

COMPUTATIONAL AND EXPERIMENTAL INVESTIGATION OF  
FLOW AND COMBUSTION PHYSICS IN POROUS MEDIA

A DISSERTATION  
SUBMITTED TO THE DEPARTMENT OF MECHANICAL  
ENGINEERING  
AND THE COMMITTEE ON GRADUATE STUDIES  
OF STANFORD UNIVERSITY  
IN PARTIAL FULFILLMENT OF THE REQUIREMENTS  
FOR THE DEGREE OF  
DOCTOR OF PHILOSOPHY

Sadaf Sobhani

October 2019

© 2019 by Sadaf Sobhani. All Rights Reserved.  
Re-distributed by Stanford University under license with the author.



This work is licensed under a Creative Commons Attribution-  
Noncommercial 3.0 United States License.  
<http://creativecommons.org/licenses/by-nc/3.0/us/>

This dissertation is online at: <http://purl.stanford.edu/qr848tv8220>

I certify that I have read this dissertation and that, in my opinion, it is fully adequate in scope and quality as a dissertation for the degree of Doctor of Philosophy.

**Matthias Ihme, Primary Adviser**

I certify that I have read this dissertation and that, in my opinion, it is fully adequate in scope and quality as a dissertation for the degree of Doctor of Philosophy.

**Craig Bowman**

I certify that I have read this dissertation and that, in my opinion, it is fully adequate in scope and quality as a dissertation for the degree of Doctor of Philosophy.

**Anthony Kovscek**

I certify that I have read this dissertation and that, in my opinion, it is fully adequate in scope and quality as a dissertation for the degree of Doctor of Philosophy.

**Nagi Mansour**

Approved for the Stanford University Committee on Graduate Studies.

**Patricia J. Gumpert, Vice Provost for Graduate Education**

*This signature page was generated electronically upon submission of this dissertation in electronic format. An original signed hard copy of the signature page is on file in University Archives.*

# Abstract

As emission regulations become increasingly more stringent and policies evolve to combat global climate change impacts, reducing pollutant and greenhouse gas emissions emerge as one of the most important goals of combustion research. Techniques such as staged combustion, lean premixed combustion, catalytic combustion, and advanced mixing and fuel atomization are some of the methods examined to reduce emissions of pollutants such as nitrogen oxides ( $\text{NO}_x$ ), carbon monoxide (CO), and unburned hydrocarbons (UHCs). Porous media combustion represents an advanced combustion concept that is capable of achieving low emissions, enhanced flame stabilization, and improved fuel efficiency. Conventionally, Porous Media Burners (PMBs) utilize a two-zone “step” burner design, which operates on the principal that the upstream high pore-density region serves as a flame arrestor and flame stability is observed at the interface between the two regions of high and low pore density.

This dissertation contributes to the analysis of combustion in porous media, characterization of its performance in conventional PMBs, and the development and testing of a novel porous matrix design for enhanced combustion performance. First, a characterization of the combustion stability, pressure drop and pollutant emissions of conventional two-zone “step” PMB is presented for a range of operating conditions and burner designs. Long-term material durability tests at steady-state and cycled on-off conditions were performed under operation with methane-fuel at atmospheric pressure. Thermocouple temperature measurements and pressure drop data are presented and compared to results obtained from 1D volume-averaged simulations. Additionally, the burner design with the maximum combustion stability regime was identified and tested in subsequent high-pressure experiments at 2, 8, and 20 bar with

fully vaporized and preheated n-heptane and methane fuels, at fuel-lean equivalence ratios.

Second, in an effort to expand the combustion stability regime beyond the capability of two-zone “step” PMBs, a novel burner design having a spatially graded porous matrix is proposed, resulting from the theoretical analysis of the governing equations and constitutive relations. This analysis reveals the significance of the pore topology on interphase heat exchange and radiative heat transfer properties, quantified by the local Stanton number and optical depth, respectively. Gradation in topology (i.e. porosity, pore diameter, cell diameter, etc.) enables the flame to stabilize dynamically within the porous matrix and for a wider range of operating conditions. Computational stability maps, temperature profiles, and emissions data are presented for comparable two-zone “step” and “graded” burner concepts, which predict significant performance enhancements in the latter.

The theoretical and computational investigation of matrix gradation in PMBs as well as experiments reveal the potential for tailoring the internal heat transfer properties to optimize performance, and thus motivates the subsequent work in leveraging recent advancements in additive manufacturing to enable smoothly graded porous structures. The next part of this dissertation achieves the use of Lithography-based Ceramic Manufacturing for the fabrication of functionally graded matrix structures, designed using periodic surface equations. The manufactured samples were operated in a PMB over a range of operating conditions to test the feasibility and performance of additive manufactured materials in PMBs. Thermal and durability testing of the manufactured parts are characterized, along with combustion stability maps from the “step” and “graded” PMB experiment, which, consistent with the previous theoretical, computational, and experimental results, show significant performance improvements of the “graded” burner.

# Acknowledgments

I would like to thank and acknowledge the many people and agencies who supported the work presented in this dissertation, including the generous financial support from the NASA Leading Edge Aeronautics Research program, as well as the National Science Foundation Graduate Research fellowship, Enhancing Diversity in Graduate Education fellowship, Graduate Public Service fellowship, and Schneider fellowship.

I would like to acknowledge my advisor, Matthias Ihme, who offered invaluable advice and guidance in both formulating the research topics and pursuing them to fruition. I would also like to thank my thesis committee members, Tom Bowman, Anthony Kovsek, Sarah Heilshorn, and Nagi Mansour who have given me incredible professional and personal mentorship over the years. Beyond the members of the committee, I am grateful to my other mentors, John Dabiri and Kenneth Goodson, and I thank them for their time and effort in helping me navigate my academic journey. I also want to acknowledge the privilege of being a part of the vibrant scientific community of the Flow Physics and Computational Engineering Group, for which I am specially grateful to: professors Parviz Moin, Ali Mani, Gianluca Iaccarino, John Eaton, and Sanjiva Lele; the administrative staff Corinne Beck, Susan Dorman, and Pamela Nelson Foster; and all the past and present students and postdocs, in particular Jared Dunnmon and Yee Chee See. During my PhD, I also had the opportunity to pursue several internships outside of Stanford and fortify my expertise in combustion and porous materials. My incredible mentors included Xiaobai Li at the Bosch Research and Development, Reid Detchon at the United Nations Foundation, and Nagi Mansour, Francesco Panerai, and Arnaud Borner at the NASA Ames Research Center.

In preparing this dissertation, I have benefited greatly from discussions with numerous collaborators, and I acknowledge their specific contributions in the footnotes at the start of each chapter. I'd like to specially thank my colleagues Danyal, Emeric, Priyanka and Joseph for their teamwork and cherished friendship. I'd also like to thank my friends Issra, Carmel, Saba, Briana, Yassi, Nura, Matisse, and Maura for their incredible support throughout the PhD process and for helping me stay grounded. A special thank you to my dear friend Erika for being there for every high and low during the PhD, advising me during difficult moments, and bringing me so much laughter and joy.

Lastly, I would like to thank my family. I am so grateful for the love and support of my husband Maxime, who has always believed in me, even when I didn't believe in myself, and pushed me to be my best self. I owe so much of this achievement to him and I couldn't imagine going through this journey without him. I am also grateful for all the support and encouragement from my in-law family, Paul-Henri, Isabelle, Anne-Sophie, Sarah, Josette, Mado, and Jean-Pierre. Likewise, I sincerely appreciate the love and support of my grandparents, uncles, aunts and cousins, each of whom have played a critical role in helping shape me to who I am today.

I truly cannot adequately express the love and support that my sister has provided me for my entire life, and I thank her for her unconditional guidance, understanding, and positivity. Next, I would like to acknowledge my caring brother-in-law Paul, who has brought me so much joy since joining our family. Finally, my sincerest gratitude to my parents, Parviz and Nahid, who have sacrificed so much for me to pursue my education. My mom has been a true example of what hard-working looks like and inspired me to reach for seemingly out-of-reach goals. And my dad, who has always nurtured my curiosity about the world and instilled in me a drive to solve difficult problems. My affinity for science and mathematics, and ultimate decision to pursue engineering are all inspired by my father, and for this, I'd like to dedicate this dissertation to him.

# Nomenclature

## Acronyms

1D	One-Dimensional
3D	Three-Dimensional
AM	Additive Manufacturing
CAD	Computer Aided Design
CO	Carbon monoxide
CVD	Chemical Vapor Deposition
EDX	Energy Dispersive X-ray
LCM	Lithography-based Ceramic Manufacturing
NO <sub>x</sub>	Nitrogen oxide
PMB	Porous Media Burner
PPI	Pores Per Inch
SEM	Scanning Electron Microscope
SiC	Silicon Carbide
TPMS	Triply Periodic Minimal Surfaces
XCT	X-ray Computed Tomography

YZA            Yttria-stabilized Zirconia Alumina

### Greek symbols

$\Delta P$	Pressure drop
$\alpha_g$	Gas thermal diffusivity ( $m^2/s$ )
$\dot{\omega}_i$	Species $i$ production rate per unit volume ( $kg/m^3 s$ )
$\epsilon$	Porosity
$\kappa$	Radiative heat extinction coefficient ( $W/m^2 K$ )
$\lambda$	Thermal conductivity ( $W/mK$ )
$\nu$	Mass of oxygen per mass of fuel ratio at stoichiometric conditions
$\omega$	Pore-density frequency in TPMS equations
$\Omega$	Scattering albedo
$\phi$	Equivalence ratio
$\rho$	Density ( $kg/m^3$ )
$\sigma$	Stefan-Boltzmann constant ( $W/m^2 K^4$ )

### Roman symbols

$\dot{m}$	Mass flux rate ( $kg/s$ )
$\dot{q}$	Heat release rate ( $W/m^3$ )
$A$	Burner cross-sectional area ( $m^2$ )
$A$	Pre-exponential factor of the Arrhenius reaction rate ( $m^3/kg s$ )
$a$	Porous media specific surface area, $1/d_{SA}$ ( $1/m$ )
$c$	Specific heat capacity ( $J/kgK$ )

$D$	Burner diameter (m)
$d$	Pore diameter (m)
$d_H$	Hydraulic diameter (m)
$d_p$	Particle diameter (m)
$d_v$	Pore diameter based on total volume of void space (m)
$D_{ij}$	Binary diffusion coefficient of species $i$ ( $\text{m}^2/\text{s}$ )
$D_{im}$	Mixture diffusivity of species $i$ ( $\text{m}^2/\text{s}$ )
$d_{SA}$	Porous media length scale based on surface area, $1/a$ (m)
$E_a$	Activation energy (J/mol)
$F$	Fuel
$H$	Burner height (m)
$h_v$	Volumetric heat transfer coefficient ( $\text{W}/\text{m}^3\text{K}$ )
$K_1$	Intrinsic or Darcian permeability ( $\text{m}^2$ )
$K_2$	Non-Darcian drag coefficient (m)
$L$	Porous media characteristic length scale (m)
$N$	Number of pores in a specific volume of porous media
$N_s$	Number of species
$O$	Oxidizer
$q$	Porosity coefficient in TPMS equations
$Q$	Fuel-mass based heat of reaction ( $\text{m}^3/\text{kgs}$ )
$R_u$	Universal gas constant

$S_L$	Laminar flame speed (m/s)
$T$	Temperature (K)
$u$	Volume-averaged fluid velocity (m/s)
$u_D$	Darcy velocity (m/s)
$V_i$	Diffusion velocity of species $i$ (m/s)
$V_p$	Total volume of void space (m <sup>3</sup> )
$W$	Mixture averaged molecular weight
$W_i$	Molecular weight of species i
$X_i$	Mole fraction of species $i$
$Y_i$	Mass fraction of species $i$
$\phi$	Mass flux rate (kg/m <sup>2</sup> s)
Nu	Nusselt number
Pe	Péclet number
Re	Reynolds number
St	Stanton number
MFR	Mass flux rate (kg/m <sup>2</sup> s)

### Other symbols

$F$	Fuel subscript
$g$	Gas phase subscript
$o$	Oxidizer subscript
$s$	Solid phase subscript
$_{eff}$	Effective property in the porous matrix subscript

# Contents

<b>Abstract</b>	<b>iv</b>
<b>Acknowledgments</b>	<b>vi</b>
<b>1 Introduction</b>	<b>1</b>
1.1 Research Objectives . . . . .	6
1.2 Accomplishments . . . . .	8
<b>2 Numerical modeling</b>	<b>10</b>
<b>3 Performance study at atmospheric conditions</b>	<b>18</b>
3.1 Motivation . . . . .	18
3.2 Experimental apparatus and procedure . . . . .	19
3.3 Numerical model . . . . .	25
3.4 Results and discussion . . . . .	27
3.4.1 Flame stability and temperature profiles . . . . .	27
3.4.2 CO and NO <sub>x</sub> emissions . . . . .	32
3.4.3 Pressure drop . . . . .	35
3.4.4 Durability testing . . . . .	35
3.5 Summary . . . . .	38
<b>4 Performance study at elevated pressures</b>	<b>40</b>
4.1 Motivation . . . . .	40
4.2 Computational analysis . . . . .	41

4.3	Experimental study . . . . .	45
4.4	Results and discussion . . . . .	52
4.4.1	Flame stability and temperature profiles . . . . .	52
4.4.2	Pressure drop . . . . .	56
4.4.3	Emissions . . . . .	58
4.5	X-ray Computed Tomography analysis . . . . .	60
4.6	Summary . . . . .	61
<b>5</b>	<b>Modulation of heat transfer</b>	<b>64</b>
5.1	Motivation . . . . .	64
5.2	Computational investigation . . . . .	65
5.2.1	Theoretical analysis . . . . .	65
5.2.2	Computational method and setup . . . . .	67
5.2.3	Parametric analysis . . . . .	69
5.3	Experimental investigation . . . . .	72
5.3.1	Experimental setup and procedure . . . . .	72
5.3.2	Micro-XCT and analysis of the porous foam . . . . .	76
5.3.3	Results and discussion . . . . .	76
5.4	Summary . . . . .	81
<b>6</b>	<b>Tailoring porous media burners</b>	<b>82</b>
6.1	Motivation . . . . .	82
6.2	Porous structures using triply periodic minimal surfaces . . . . .	85
6.3	Fabrication methodology . . . . .	87
6.4	XCT analysis of printed porous structures . . . . .	89
6.5	Thermal conductivity and durability of additive manufactured alumina	95
6.6	Tailored structures implemented in porous media burners . . . . .	101
6.6.1	Experimental setup . . . . .	102
6.6.2	Results and discussion . . . . .	102
6.7	Summary . . . . .	106

<b>7 Conclusions</b>	<b>108</b>
7.1 Main findings . . . . .	108
7.2 Directions for future work . . . . .	111
7.2.1 Addressing challenges in deploying PMBs to real-world applications . . . . .	111
7.2.2 Developing improved closure models for combustion in porous media . . . . .	111
7.2.3 Applying tailored ceramic structures to applications beyond PMBs . . . . .	112
7.2.4 Improving and expanding the ceramic porous structure fabrication methodology . . . . .	112
<b>A Experimental data</b>	<b>114</b>
A.1 Introduction . . . . .	114
A.2 Performance study at atmospheric conditions . . . . .	114
A.2.1 Stability diagram . . . . .	114
A.2.2 Thermocouple measurements . . . . .	116
A.2.3 Emissions measurements . . . . .	119
A.2.4 Pressure drop measurements . . . . .	120
A.3 Performance study at elevated pressures . . . . .	122
A.3.1 Thermocouple measurements . . . . .	123
A.3.2 Stability diagram, emissions, and pressure drop . . . . .	126
A.4 Modulation of heat transfer . . . . .	130
A.4.1 Stability diagram and pressure drop . . . . .	130
A.4.2 Thermocouple measurements . . . . .	135
A.5 Tailoring porous media burners . . . . .	136
A.5.1 Thermal conductivity of additive manufactured alumina . . . . .	136
A.5.2 Stability diagram . . . . .	137

# List of Tables

2.1	Boundary conditions for 1D simulations using volume-averaged models.	12
3.1	Specifications of configurations and pore density (PPI) of the five burners. Burners were composed of two porous samples in the upstream sections and one in the downstream sections; each sample has a height of 2.54 cm. . . . .	20
4.1	Axial locations of the thermocouples, measured from the outlet of the PMB. The thermocouples are positioned at the outer perimeter of the burner at azimuthal locations varying by 90° (see Fig. 4.4). Note that the thermocouple A-3 was damaged in early testing. . . . .	50
4.2	Summary of the test series operating fuel and pressure, as well as the range of tested operating conditions. . . . .	52
4.3	Acquisition parameters of the XCT scans. . . . .	60
5.1	Geometry of the burners, where $x$ is the axial position, $L$ is the burner length, $x_I$ is the length of the upstream section, $\epsilon$ is porosity, and $d$ is pore diameter; subscripts 1 and 2 denote values at the inlet and outlet, respectively, $\Delta d = d_2 - d_1$ , $\Delta \epsilon = \epsilon_2 - \epsilon_1$ , $\mathcal{H}(\xi)$ denotes the Heaviside function. . . . .	66
6.1	Geometric parameters for the burners tested, where $d$ , $\epsilon$ , $H$ , and $D$ refer to pore diameter, porosity, burner height, and burner diameter, respectively. . . . .	91

A.1	Data corresponding to the stable operating conditions presented in Fig. 3.6. . . . .	114
A.2	Thermocouple measurements, [K], corresponding to burner 1 and 2, including data from Fig. 3.8. The equivalence ratio, $\phi$ , and mass flux rate, $\dot{m}''$ , for each Operating Condition (OC) are described in the table.	116
A.3	Emissions measurements, including data corresponding to Fig. 3.10. .	119
A.4	Pressure drop, $\Delta P$ , measurements, including data corresponding to the cold flow cases of Fig. 3.11. Note that the units in the table are in WC, not pressure drop percentage as in the corresponding figure. B 1–B 5 refer to burners 1–5. . . . .	120
A.5	Pressure drop, $\Delta P$ , measurements, including data corresponding to the reacting flow cases of Fig. 3.11. Note that the units in the table are in WC, not pressure drop percentage as in the corresponding figure.	121
A.6	Thermocouple measurements, [K], including data from Fig. 4.7. The equivalence ratio, $\phi$ , and mass flux rate, $\dot{m}''$ , for each Operating Condition (OC) are described in the table. The thermocouples A–D correspond to the locations specified in Fig. 4.4 and Table 4.1. . . . .	123
A.7	Data corresponding to the stability regime and CO emissions presented in Fig. 4.5, $\text{NO}_x$ emissions of the stable operating conditions as presented in Fig. 4.10, and pressure drop measurements corresponding to Fig. 4.9a. . . . .	126
A.8	Data corresponding to the stable operating conditions presented in Fig. 5.7 and pressure drop, $\Delta P$ , measurements, including data corresponding to Fig. 5.9. . . . .	131
A.9	Thermocouple measurements, [K], corresponding to the step and graded burners from Fig. 5.8. The equivalence ratio, $\phi = 0.75$ , for all cases and mass flux rate, $\dot{m}''$ , for each Operating Condition (OC) are described in the table. . . . .	135
A.10	Thermal conductivity data, [W/mK], as a function of temperature, corresponding to Fig. 6.6. Materials are described in Section 6.5. The relative standard deviation of each measurement is shown in parenthesis.	136



# List of Figures

1.1	Schematic and temperature profile of a conventional two-zone “step” porous media burner. . . . .	2
3.1	SiC 10 PPI, the ceramic reticulated foam used in the combustion zone of Burners 1-3, with a few pores outlined to illustrate the polygonal pore geometry of the SiC foams. . . . .	21
3.2	YZA 10 PPI, the ceramic reticulated foam used in the combustion zone of Burners 4, with a few pores outlined to illustrate the circular pore geometry of the YZA foams. . . . .	21
3.3	Cross-sectional schematic of experimental apparatus. . . . .	23
3.4	Image of the experimental setup at Alzeta with burner, thermocouples, and test rig. . . . .	24
3.5	Location of the thermocouples, referred to as A-D, at the burner outer diameter. . . . .	25
3.6	Stability map for all five burners, with stability maximized for burner 5. The data corresponding to this figure can be found in Table A.1 in Appendix A . . . . .	28
3.7	(a) Porous media burner during stable and (b)-(d) unstable blow-off operation. (b) The flame is approaching the top surface asymmetrically. (c) A portion of the cold reactant mixture has reached the top surface. (d) The flame has reached the top surface (i.e. blow-off). These images from above the burner illustrate the non-uniformity in flame behavior. . . . .	29

3.8	Temperature variations along azimuthal direction between thermocouples, referred to as A-D, at the same axial locations (Fig. 3.5). Maximum temperature variation between thermocouples less than 1 mm apart along axial direction is labeled along with percentage different compared to maximum temperature measured. The data corresponding to this figure can be found in Table A.9 in Appendix A . . . . .	30
3.9	Averaged temperature measurements from four thermocouples compared to simulation results, described in Section 3.3 for burner 1 and 2 at various mass flux rates (MFR) and equivalence ratios $\phi$ . . . . .	31
3.10	Emissions for burners 1-3 and 5, corrected to 3% O <sub>2</sub> . Blow-off, flashback, and stable operating conditions for each burner correspond to Fig. 3.6. (a) CO emissions near flash-back conditions. CO emissions near blow-off not shown since all values are near zero. (b), (c) NO <sub>x</sub> emissions near flash-back and blow-off, respectively. (d) NO <sub>x</sub> and CO at a commonly stable operating condition of $\phi=0.5$ , MFR=0.34. The data corresponding to this figure can be found in Table A.3 in Appendix A	34
3.11	Comparison of predicted pressure drop (lines) and experimental results (symbols) for (a) cold flow conditions using three different characteristic lengths for burner 4 and the pore diameter from image analysis for all burners, and (b) reacting flow conditions, with comparison to computational results (lines) for geometry and material properties matching burner 2. Diameter of circles corresponds to equivalence ratio, $\phi = 0.47\text{--}0.66$ . The data corresponding to this figure can be found in Table A.4 and A.5 in Appendix A . . . . .	36
3.12	Temperature of PMB during cycle operation (1229 cycles total), showing 2 minute air purge, fuel addition, and ignition. Thermocouple locations are with respect to Fig. 3.5. . . . .	37
3.13	X-ray images showing cracking in the 3PPI sample of burner 5. . . . .	37

4.1	Computational profiles at $\phi = 0.57$ of (a),(b) gas temperature for free flames and PMB, and (c) heat transfer coefficient in PMB. In (d)-(f), the mass flux rate in the PMB simulation corresponds to that of the n-heptane free flame at 2, 8, and 20 bar, equal to 0.4, 0.87, and 1.34 kg/(m <sup>2</sup> s), respectively and 0.47 kg/(m <sup>2</sup> s) for methane at 8 bar. Symbols indicate the predicted solid-phase temperature. . . . .	43
4.2	Schematic of PMB test hardware located inside the high-pressure test facility SE-5 at NASA GRC. . . . .	46
4.3	Image of the high-pressure test facility SE-5 at NASA GRC. . . . .	47
4.4	Azimuthal and axial locations of thermocouples, corresponding to values in Table 4.1, in SiC (black) element and YZA (yellow) elements. In the right image, the flow direction would be from the bottom to the top. . . . .	49
4.5	Stability maps for liquid C <sub>7</sub> H <sub>16</sub> PMB: (a-b) flashback and blow-off boundaries of the stability regimes, with the size of the symbols representing CO emissions between 0–17 ppm, (c) flame stability maps, solid lines imply limit of stability, other boundaries determined by limits of the mass flow controllers and thermocouples, (d) stability maps, normalized by the local burning rate. Open symbols denote tested yet unstable conditions. The data corresponding to this figure can be found in Table A.7 in Appendix A . . . . .	53
4.6	(a) Comparison of flame stability for C <sub>7</sub> H <sub>16</sub> and CH <sub>4</sub> at 8 bar: a) stability maps, (b) stability maps normalized by the laminar burning rate. Open symbols denote tested yet unstable conditions. The data corresponding to this figure can be found in Table A.7 in Appendix A	54

4.7	Temperature profiles at various mass flux rates (MFR) and equivalence ratios, $\phi$ , of C <sub>7</sub> H <sub>16</sub> flames at a) 2 bar, b) 8 bar, and c) 20 bar marked in Fig. 4.5c, where the orange data correspond to near blow-off conditions and the other data correspond to stable operating conditions. (d) Comparison of temperature profiles of C <sub>7</sub> H <sub>16</sub> (black) and CH <sub>4</sub> (green) at 8 bar at similar mass flux rate and $\phi = 0.47$ . Symbols ▶ correspond to thermocouples A and B, and symbols ◀ to thermocouples C and D, and the lines correspond to the average temperature at each location. The data corresponding to this figure can be found in Table A.6 in Appendix A . . . . .	55
4.8	3D temperature profile rendering corresponding to the leanest conditions in Fig. 4.7, (a) $\phi = 0.48$ , 0.93 $\frac{\text{kg}}{\text{m}^2\text{s}}$ , (b) $\phi = 0.43$ , 1.34 kg/(m <sup>2</sup> s), (c) $\phi = 0.42$ , 2.68 kg/(m <sup>2</sup> s), (d) $\phi = 0.47$ , 1.55 kg/(m <sup>2</sup> s). . . . .	57
4.9	Measurements of pressure drop at stable operating conditions, where symbols correspond to operating pressure at 2 bar (●), 8 bar (▲) and 20 bar (■). The data corresponding to this figure can be found in Table A.7 in Appendix A . . . . .	58
4.10	Emissions measurements at stable operating conditions for both methane and heptane fuels, at 2 bar (●), 8 bar (▲) and 20 bar (■). The data corresponding to this figure can be found in Table A.7 in Appendix A . . . . .	59
4.11	Side and top view of the XCT isosurface of the full SiC porous foam matrix (5.08cm diameter and 2.54 cm height) in the downstream zone of the burner, post-combustion, after 22 hours of operation. Scan acquisition parameters correspond to Scan 1 in Table 4.3. . . . .	61
4.12	XCT isosurface of a strut in 1.8 mm field of view of the SiC porous foam matrix in the downstream zone of the burner, pre- and post-combustion, where the arrow indicates the location of the crack. XCT-acquisition parameters correspond to Scan 2 in Table 4.3. . . . .	62

5.1	Contour map of the local Stanton number as a function of pore diameter, $d$ , and mass flux rate, $\dot{m}''$ . Ranges of Stanton numbers accessed in the “step” burners versus the “graded” burners are illustrated. . . . .	67
5.2	Computational stability maps of (a,c) “step” and (b,d) “graded” burners 1 and 2, respectively, as well as mass flux rate associated with laminar flame speed indicated by $S_L$ (dashed line) and experimental measurements (symbols). . . . .	70
5.3	(a) Gas temperature profiles at $\phi = 0.55$ corresponding to stability maps shown in Fig. 5.2a,b and (b) profiles centered at flame peak temperature location $X_F$ for local St, for graded (blue) and step (black) profiles. . . . .	71
5.4	P&ID illustrating the experimental setup and instrumentation. . . . .	73
5.5	Images of burner in operation, at steady state conditions (left) and near blow-off (right). . . . .	74
5.6	Average pore and cell diameters for “step” (top) and “graded” (bottom) PMBs, as well as nominal pore diameters used in the model. . . . .	75
5.7	Experimental stability maps for graded (blue) and step (black) profiles, illustrating an extension of the blow-off limits for the “graded” burner. The data corresponding to this figure can be found in Table A.8 in Appendix A . . . . .	77
5.8	Thermocouple measurements (symbols, dashed lines) at $\phi = 0.75$ compared to the model (solid lines), for graded (blue) and step (black) profiles. The data corresponding to this figure can be found in Table A.9 in Appendix A . . . . .	78
5.9	Pressure drop experimental measurements (symbols) compared to the model for $\phi = 0.7$ (lines), for graded (blue) and step (black) profiles. The data corresponding to this figure can be found in Table A.8 in Appendix A . . . . .	79

6.1	Schematic outlining the three phases of actualizing tailored porous structures, starting from design using mathematically defined surfaces, fabrication, and post-print analysis. . . . .	84
6.2	SEM images, at 650 times magnification, of wafers of the HP500 material A (top) and 350D material B (bottom) alumina, illustrating the variation in surface roughness and microporosity between the materials. . . . .	90
6.3	XCT measurements of cell diameter, pore diameter, and porosity of burner 1. . . . .	92
6.4	Variations between the designed and final printed structure for burner 2, in (a) cell diameter, (b) pore diameter, and (c) porosity, illustrating four cells with red surfaces to represent the locations and morphologies of two pores, and colored rings on the struts represent the throat locations. The mean diameters of the throats pictured were estimated as $352 \mu\text{m}$ for the original geometry, versus $229 \mu\text{m}$ for the 3D printed sample. . . . .	93
6.5	XCT measurements of cell diameter, pore diameter, and porosity of burner 3. . . . .	94
6.6	Thermal conductivity measurements at various temperatures of the solid disks and porous structure, with material A and B corresponding to Alumina 350D and HP500, respectively. All data presented correspond to samples printed with XY-plane layer orientations, with thermal conductivity measured in the Z-direction. The data corresponding to this figure can be found in Table A.10 in Appendix A . . . . .	96
6.7	Bunsen burner setup used to test the material durability of the additive manufactured alumina. . . . .	99
6.8	SEM images of the porous matrix before and durability testing, at $25\times$ and $500\times$ magnification near the location of the exposed strut shown in the white box of (a). . . . .	100
6.9	$25\times$ magnified SEM (left) and EDX composition maps after 1 hour of combustion of Al (middle) and O (right). . . . .	101

6.10 (Left) Porous structure with graded pore diameter ( $d = 1.5\text{--}3.5$ mm) and constant porosity (75%) profile after binder burnout and sintering of green part. (Right) Experimental setup illustrating the burner in operation with instrumented thermocouples. Methane/air flows from bottom to top, and the flame is visible through the insulation and quartz tube. . . . .	103
6.11 Experimental flame stability measurements, illustrating maximum and minimum stable mass flux at each equivalence ratio, $\phi$ , tested in burner 1–3 (see Table 6.1). The data corresponding to this figure can be found in Table A.11 in Appendix A . . . . .	105
6.12 XCT scan of a small broken fragment of the 3D printed 350D alumina matrix, post-PMB experimentation. . . . .	106

# Chapter 1

## Introduction

Combustion within the cavities of an inert porous medium exhibits characteristics different from those of conventional burners that utilize a free flame, and has been identified in several comprehensive reviews ([Howell et al. 1996](#); [Wood and Harris 2008](#); [Mujeebu et al. 2009](#); [Ellzey et al. 2019](#)) as a promising technology for achieving higher burning rates, extending flammability limits, and reducing emissions.

Figure 1.1 illustrates a conventional two-zone “step” burner, composed of the flame arrestor and combustion zone, which will be explained in further detail below. For now, this design is shown in order to describe the basic operating principles of Porous Media Burners (PMBs). Essentially, the solid porous matrix serves as a means of internally recirculating heat from the combustion products upstream to the reactants, termed “excess enthalpy combustion” ([Hardesty and Weinberg 1973](#)). Downstream of the flame, the temperature of the combustion products is higher than that of the surrounding solid. Thus, the heat generated from the chemical reactions convects into the solid, and then recirculates upstream to the cooler parts of the solid matrix via solid conduction and long range solid-to-solid radiation. The thermal conductivity of the solid matrix can be several orders of magnitude larger than that of the gas, therefore heat generated by the flame is readily conducted upstream to preheat the incoming reactants. This recirculation of heat results in higher solid-phase temperatures in the upstream zone, as compared to incoming gas. The heat is then transferred to the unburned gas mixture by convection, effectively preheating the

incoming reactants. Figure 1.1 also illustrates the steady-state temperature profiles of the solid and gas, computed using the numerical model presented in Chapter 2. Additionally, the high heat capacity of the solid matrix stabilizes fluctuations in thermal load and fuel/air ratio, thereby mitigating the propensity for blow-off and other combustion instabilities.

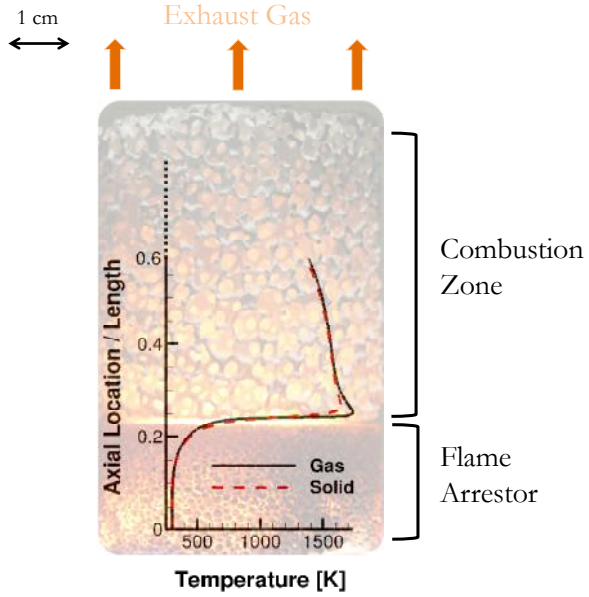


Figure 1.1: Schematic and temperature profile of a conventional two-zone “step” porous media burner.

The lean flammability limit of a fuel-air mixture decreases with increasing preheating of the mixture, and therefore heat recirculation in PMBs can lead to a reduction in this lower limit ([Zabetakis et al. 1958](#)). The practical advantages of extending the lean flammability limit include lower emissions of CO, reliable operation of low calorific fuels, reduced thermal stresses due to decreased flame temperatures, and complete fuel conversion. Additionally, the higher temperatures of the preheated reactants lead to a faster flame speed and enhanced power output ([Howell et al. 1996](#)), while the gas-to-solid convection downstream of the flame decreases the gas temperature in the reaction zone and the exhaust gas, thereby reducing the formation of thermal NO<sub>x</sub> ([Kotani and Takeno 1982](#); [Wood and Harris 2008](#)). The challenge in

PMB research lies in stabilizing these flames inside the porous matrix in the presence of complex thermophysical, transport, and heat-transfer processes. The energy released during chemical reactions is coupled with the conjugate heat transfer inside the porous structure, which results from strong heat exchange in the reaction zone.

Porous media refers to any materials with connected voids that facilitate fluid flow. The geometries considered in numerical and experimental investigations of PMBs include packed beds of spheres, arrays of staggered cylinders, fiber lamellae, and ceramic or metal foams, which have large surface-to-volume ratios, enabling maximum heat exchange between the solid and gas phases, and high porosities, thereby minimizing the pressure drop. Common materials used for the porous structure are Yttria-stabilized Zirconia Alumina (YZA), Alumina ( $\text{Al}_2\text{O}_3$ ) and Silicon Carbide (SiC), with solid thermal conductivities of approximately  $4 \text{ W/mK}$  (Choi and Bansal 2005),  $30 \text{ W/mK}$  (Hussey et al. 1998), and  $100 \text{ W/mK}$  (Lynch 1979), respectively.

Although the porous matrix extends the flame stability, the resulting coupling of the chemical energy release in the gas phase and conjugate heat transfer with the solid phase makes characterizing the flame behavior in PMBs a particularly challenging problem. Buckmaster and Takeno (1981) proposed a thermal model to predict the flame stabilization in PMBs, stating that during steady-state operation, the flame is positioned in a region where the flame speed is positively correlated with the axial location of the flame. PMB designs based on these thermal models reported approximately a 3:1 range of firing capacities, referred to as turndown ratio or power-dynamic range, for embedded flames (Kotani and Takeno 1982).

As an alternative to balancing effective flame speeds to achieve flame stabilization, Trimis and Durst (1996) proposed a quenching technique that anchors the flame at a fixed position. This design, used in most existing PMBs, is based on the concept of a critical Péclet number, which characterizes the local ratio of heat release by combustion to heat removal in a PMB (Babkin et al. 1991). The critical Péclet number determined for PMB is  $65 \pm 45$  (Wawrzinek and Trimis 2004). The flame is stabilized at the interface of the sub- and super-critical regions, and is therefore referred to as a two-zone — or “step” — PMB. A power-dynamic range up to 20:1 was reported for this design (Trimis and Durst 1996).

The quenching technique of the “step” PMB is based on the notion that the upstream region serves as a flashback arrestor. Barra et al. (2003) found that larger upstream pores and lower thermal conductivity help prevent flashback by limiting heat exchange from the solid. Sufficient flashback prevention in this design implies a performance trade-off, since limiting the reactant mixture preheating hinders the extension of both the lean flammability and blow-off limits in the burner. To address this limitation, an alternative stabilization technique was proposed by Voss et al. (2013) based on a spatially varying cross-sectional area of the burner. Contrary to the fixed-flame location of the “step” burner, in this technique the flame stabilizes at a location where the Darcy velocity balances the flame speed inside the porous matrix. Experimental studies have successfully implemented this design at high burning velocities for syngas (Voss et al. 2013) and methane (Bakry et al. 2011) with a reported power-dynamic range of approximately 6:1. However, a large angle of divergence is required to achieve adequate deceleration of the flow for some applications, which may result in relatively large cones, radial heat losses, and an inhomogeneous mean velocity profile due to the expanding flow.

Essentially, the flame stabilization is controlled by the solid matrix conductivity, optical depth and the local Stanton number, which is the ratio of the interphase heat exchange to the convective transport (Sobhani et al. 2019b). The optical depth is increased with decreasing pore diameter. Thus, if the porous media is sufficiently opaque, radiation becomes ineffective at recirculating heat. As PMBs also operate on the principle of effective interphase heat exchange, the Stanton number is an important parameter for predicting trends in burner performance:

$$\text{St} = \frac{\text{Nu}}{\text{Pe}_u}, \quad \text{Pe}_u = \frac{uL}{\alpha_g}, \quad \text{Nu} = \frac{h_v L^2}{\lambda}. \quad (1.1)$$

Since Nusselt number, Nu, is inversely proportional to the mass flux, increasing the operating flow rates of the burner reduces the preheating of the incoming reactants from the solid, eventually leading to flame blow-off.

Although a detailed understanding of the underlying processes at the pore-scale is largely incomplete at the current state, both experimental and numerical studies have

demonstrated advantages in flame stability, pollutant emissions, and lean flammability in PMBs both at atmospheric conditions and elevated pressures (El-Hossaini et al. 2008; Malico and Pereira 2001; Noordally et al. 2004; Williams and Agrawal 2012; Vijaykant and Agrawal 2007; Bedoya et al. 2015; Bakry et al. 2011).

Previous experimental and computational studies of lean premixed combustion of gaseous fuel at atmospheric pressure in PMBs have illustrated several performance advantages compared to conventional burners (Kotani and Takeno 1982; Howell et al. 1996; Barra and Ellzey 2004; El-Hossaini et al. 2008; Malico and Pereira 2001; Sobhani et al. 2017; 2019b). Investigations of lean premixed porous media combustion at elevated pressure are less common and primarily utilize gaseous fuels. Bedoya et al. (2015) utilized a conical PMB with natural gas as the fuel source, and reported enhanced burning velocities for pressures up to 14 bar. Noordally et al. (2004) studied combustion of methane-air mixtures at lean conditions up to 11 bar, although the propensity of flash-back was found to increase with increasing pressure. Bakry et al. (2011) also utilized a conical PMB operated with methane fuel at lean conditions up to 9 bar.

A limited number of studies on lean premixed combustion of liquid fuels in PMBs have also been reported, although limited to atmospheric pressure conditions. These studies demonstrate similar performance advantages as those of gaseous fuel burners, such as higher burning rates, lower lean flammability limits, and reduced emissions. Liquid-fuel combustion in a PMB was first experimentally investigated by Kaplan and Hall (1995). Liquid heptane was delivered to a nozzle and sprayed onto a porous foam upstream of the main PMB. Radiant preheating from the PMB as well as flow through the upstream porous foam facilitated enhanced fuel-droplet evaporation and mixing. The fuel/air mixture was then supplied through a gap to the PMB, and stable combustion was observed for equivalence ratios between 0.57 and 0.67. Emissions of CO are reported ranging from 3–7 ppm and NO<sub>x</sub> from 15–20 ppm, corrected for 3% oxygen. No accumulation of soot or pore plugging was observed. Tseng and Howell (1996) experimentally and computationally investigated the operation of liquid heptane in a PMB, and found stable operation for equivalence ratios as lean as  $\phi = 0.3$ . Emissions were reported to be very low, with CO < 10 ppm and NO<sub>x</sub> below 20

ppm. Combustion of kerosene in a PMB was investigated by [Vijaykant and Agrawal \(2007\)](#), using both an air-assist injector and a swirl-air injector.

In all the aforementioned studies of liquid fuel PMBs, the distance between the injector and the porous media was reported as a critical factor to maintain stable combustion. To eliminate the need of using a fuel atomizer, both [Takami et al. \(1998\)](#) and [Jugjai et al. \(2002\)](#) directly supplied kerosene to the top surface of the PMB, via a steel wire net to achieve a uniform droplet distribution. Stable combustion was achieved in the equivalence ratio ranging from 0.1 to 0.9.

Due to the high volumetric heat release of PMBs, incineration of liquid hazardous waste was proposed as a potential application of liquid fuel combustion in porous media ([Kaplan and Hall 1995](#)). PMBs at elevated pressures also have potential applications in clean gas-turbine operation ([Noordally et al. 2004](#)). In a recent numerical study, the effect of porous media combustion on the thermodynamic cycle performance of gas-turbine engines was evaluated and shown to enable appreciable increase in thermodynamic efficiency and reduction of emissions by extending the nominal lean flammability limit, thereby allowing for engine operation at higher pressure ratios and lower dilution ratios ([Mohaddes et al. 2019](#)). As outlined above, most of the existing literature on examining the operation of porous media combustion with liquid fuel has been limited to atmospheric pressures while those at elevated pressures operate with gaseous fuel.

## 1.1 Research Objectives

Motivated by the potential efficiency and emissions advantages of PMB technology, this dissertation aims to further the understanding of combustion in porous media, from which a novel and enhanced PMB design is introduced and tested. This work includes theoretical, computational, and experimental studies, leveraging both conventional and emerging additive manufacturing technologies.

The numerical framework used in the computational investigations presented in this dissertation is described in Chapter 2. In Chapter 3, a characterization of combustion stability, pressure drop and pollutant emissions for a range of equivalence

ratios, mass flow rates, and burner setups at atmospheric conditions are presented. Experimental measurements from conventional “step” burners are presented and compared to results obtained from 1D volume-averaged simulations. Experimental and model results show good agreement for temperature profiles and pressure drop evaluated using the Darcy-Forchheimer equation with Ergun’s relations. Additionally, long-term material durability tests at constant and cycled on-off conditions are presented. Measurements of product gas concentrations illustrate highest emissions of CO at conditions close to flash-back and, as expected, higher NO<sub>x</sub> emissions with increasing equivalence ratios. Enhanced flame stability is observed for burners with YZA upstream and SiC in the downstream combustion zone. Subsequently, this burner design is then tested at pressures up to 20 bar with fully vaporized and pre-heated n-heptane (C<sub>7</sub>H<sub>16</sub>) and methane fuels, at fuel-lean equivalence ratios to assess the viability of this technology for application to aviation gas-turbine engines. The high-pressure results and discussion are presented in Chapter 4.

Chapter 5 presents a novel PMB design that extends the flame stability regime beyond that of conventional designs. Inspired by a theoretical analysis of the governing equations and constitutive relations of combustion in porous media, this concept proposes a gradation in the porous matrix topology (i.e. porosity, pore diameter, cell diameter, etc.), which enables a continuous variation of radiative extinction properties as well as interphase heat exchange, allowing the flame to stabilize dynamically within the porous matrix and for a wider range of operating conditions. Through computations and experiments, it is shown that the proposed physical design of the porous matrix results in a significant enhancement of the power-dynamic range and in excess of 50% higher blow-off limits compared to conventional designs. The experimentation of this concept was performed using a step-wise approximation of a graded topology profile, motivating the subsequent efforts to enable a smoothly graded ceramic porous structure. In this chapter, theoretical analysis, computational studies and preliminary experimental results indicate the potential of pore-space gradation of ceramic structures to enable significant performance enhancements in PMBs. However, conventional ceramic fabrications techniques are easily amenable to the tailoring of the local porous microstructure.

In Chapter 6, a framework is proposed for designing and manufacturing tailored ceramic porous structures for application to high-temperature environments. Lithography-based Ceramic Manufacturing (LCM) is utilized, enabling the production of complex and customized structures on a layer-by-layer basis from Computer Aided Design (CAD) model data. The matrix topology used as the input to the LCM is designed using periodic surface equations. Next, the feasibility of additive manufactured PMBs with spatially graded porous matrices is experimentally investigated. The benefits of microstructure tailoring are illustrated, which, consistent with the previous theoretical, computational, and preliminary experimental results, show significant performance improvements in performance of “graded” PMBs as compared to conventional “step” designs. Conclusions and directions for future work are discussed in Chapter 7.

## 1.2 Accomplishments

This dissertation includes the following original contributions that further both the fundamental understanding of combustion in porous media and the development of PMB technology with potential applications to propulsion, stationary gas turbines, waste-heat recovery, incineration of liquid hazardous waste, reformers, and domestic heating units:

- Characterized, via experimentation and computation, the operational stability and trends in pollutant formation for combustion in conventional PMBs at atmospheric and elevated pressures up to 20 bar,
- Applied X-ray Computed Tomography (XCT) with life-cycle testing for the analysis of the microstructure durability of ceramic porous materials utilized in PMBs,
- Established a novel design of PMBs based on topology gradation of the underlying porous structure that significantly extends the flame stability regime as compared to conventional PMBs,

- Enabled tailoring and customization of the porous structure topology with specified porosity and pore diameter profiles via Triply Periodic Minimal Surface equations, enabling future design optimizations,
- Demonstrated the enhanced combustion performance in “graded” PMBs, using additive manufacturing to fabricate smoothly graded porous structures,
- Applied and characterized lithography-based additive manufactured ceramics for tailored porous structures suitable in high-temperature environments, potentially applicable to numerous energy and thermal management systems.

## Chapter 2

# Computational modeling and simulation of combustion in porous media

In the conventional Computational Fluid Dynamics approach, direct simulation of the Navier-Stokes equations are obtained under full representation of the domain by a body fitted mesh. Owing to the complex geometrical structure of the porous material, the mesh generation and subsequent simulation of combustion in PMBs remains only feasible for restrictively small domains. Thus, the governing equations at the pore level are volume averaged to solve for spatially averaged quantities over many pores and for larger domains. The method of volume-averaging is described in detail by [Whitaker \(1967\)](#) and [Slattery \(1967\)](#).

The main difficulty with volume-averaging methods is that they result in terms involving unresolved pore-level information. A phenomenological description of the conduction, convection, and radiation heat transfer at the macro-scale are required for closure of the volume-averaged equations. In earlier works in PMB modeling, local thermal equilibrium (i.e. single-medium approximation) was assumed between the solid and gas phase. However, this assumption was later shown to be inaccurate ([Mujeebu et al. 2010](#)). Therefore, in simulating PMB performance, the gas and solid phases must be treated separately, since the chemical reactions and heat release

occur in the gas phase while the chemical energy is recirculated and transferred via the solid phase. This modeling approach is referred to as the two-medium approximation ([Kaviany 1991](#)).

The equations governing the combustion in porous media are derived by volume-averaging of the transport equations for a chemically reacting gaseous system ([Mu-jeebu et al. 2010; Kaviany 1991](#)). Effects of conduction and radiation in the solid phase, and heat exchange between solid and gas are incorporated in the equations. The following assumptions are used in the current model formulation:

- the Dufour, Soret, and viscous heat dissipation effects are negligible,
- the burner is radiating to a black body at 300 K from the inlet and outlet,
- the solid matrix emits, absorbs and scatters radiation as a gray body,
- radiation in the gas phase is negligible,
- the solid matrix is inert and potential catalytic effect is neglected,
- neither flame stretch nor turbulence are induced by the flow, resulting in a one-dimensional flame,
- two separate energy equations are solved for the gas and solid phases, which are coupled through a volumetric heat transfer coefficient.

With these assumptions, the governing equations for mass, species, and energy conservation take the following form:

$$\partial_t(\rho_g \epsilon) + \partial_x(\epsilon \rho_g u) = 0, \quad (2.1a)$$

$$\epsilon \rho_g (\partial_t Y_i + u \partial_x Y_i) = -\partial_x(\epsilon \rho_g V_i Y_i) + \epsilon \dot{\omega}_i, \quad (2.1b)$$

$$\begin{aligned} \epsilon \rho_g c_g (\partial_t T_g + u \partial_x T_g) &= \partial_x (\lambda_g \partial_x(\epsilon T_g)) - \rho_g \left( \sum_{i=1}^{N_s} c_{g,i} V_i Y_i \right) \partial_x(\epsilon T_g) \\ &\quad - h_v(T_g - T_s) + \epsilon \dot{q}_H, \end{aligned} \quad (2.1c)$$

$$(1 - \epsilon) \rho_s c_s \partial_t(T_s) = \partial_x (\lambda_{s,\text{eff}} \partial_x T_s) - \partial_x \dot{q}_R + h_v(T_g - T_s) \quad (2.1d)$$

The radiative source term, appearing in Eq. (2.1d) takes the form:

$$\partial_x \dot{q}_R = 2\kappa(1 - \Omega) (2\sigma T_s^4 - [\dot{q}_R^+ + \dot{q}_R^-]) , \quad (2.2)$$

where  $\kappa$  is the radiative heat extinction coefficient,  $\Omega$  is the scattering albedo and  $\sigma$  is the Stefan-Boltzmann constant. The radiant heat fluxes in the forward (+) and backward (-) directions are expressed using the Schuster-Schwarzschild approximation (Howell et al. 2010):

$$d_x \dot{q}_R^+ = -\kappa(2 - \Omega) q_R^+ + \kappa\Omega q_R^- + 2\kappa(1 - \Omega)\sigma T_s^4 \quad (2.3a)$$

$$-d_x \dot{q}_R^- = -\kappa(2 - \Omega) q_R^- + \kappa\Omega q_R^+ + 2\kappa(1 - \Omega)\sigma T_s^4 \quad (2.3b)$$

The gas and solid energy equations are coupled by the convective heat transfer,  $h_v(T_g - T_s)$ , where  $h_v$  for ceramic foams is used (Fu et al. 1998). The effective thermal conductivity in the porous solid is estimated from manufacturer data. The Discrete-Ordinates two-flux method was used to model the radiant source term in the solid phase energy equation (Eq. (2.1d)) (Howell et al. 2010). The radiative heat extinction coefficient,  $\kappa$ , is based on a geometric optics model that was validated by Hsu and Howell (1992), evaluated as  $\kappa = 3(1 - \epsilon)/d_p$ .

Inlet conditions	Outlet conditions
$T_g = 300$ K	$d_x T_g = 0$
$d_x T_s = 0$	$d_x T_s = 0$
$Y_i = Y_{i0}$	$d_x Y_i = 0$
$q^+ = \sigma T_s^4$	$q^- = \sigma T_s^4$

Table 2.1: Boundary conditions for 1D simulations using volume-averaged models.

Combustion simulations were performed using the CANTERA (Goodwin 1998) 1D reacting flow solver, which was adapted to account for the coupling between the gas and solid phases in the PMB calculations. The solution proceeds in two different

stages. In the first stage, the initial gas and solid temperatures are held at their initial values. With the update in velocity and species mass fractions, the next step solves all four conservation equations, Eq. (2.1a)–(2.1d), taking in more realistic initial conditions for the chemical kinetics equations rather than those initially prescribed. In both stages, the solver first attempts to solve the equations at steady-state by minimizing the residual norm through Newton-minimization method. This process is repeated to reduce the residuals of the governing equations until a solution that meets the tolerances is found or the solution begins to diverge, in which case the solver switches to trying to solve the transient problem instead of the steady state. This switch allows for the profiles to evolve and approach the true steady-state solution. In attempting the transient solution, an increasing number of time steps forward are attempted before reverting to the steady-state solver, depending on whether each attempt is successful. The boundary conditions for solving Eq. (2.1) are given in Table 2.1.

The pressure drop was evaluated using the Darcy-Forchheimer equation ([Philipse and Schram 1991](#)):

$$d_x P = -\frac{\mu}{K_1} u_D - \frac{\rho}{K_2} u_D^2 , \quad (2.4)$$

using the Ergun's equations ([Ergun and Orning 1949](#)) to evaluate the permeability and drag coefficients:

$$K_1 = \frac{d_p^2 \epsilon^3}{150(1-\epsilon)^2} , \quad K_2 = \frac{d_p \epsilon^3}{1.75(1-\epsilon)} . \quad (2.5)$$

Ergun's empirical relations were developed for unconsolidated porous media made of solid spherical particles, therefore  $d_p$  in Eq. (2.5) refers to the particle diameter. The application of this model to consolidated porous media (i.e. foams) is described in Section 3.4.3.

In this work, the model and computational framework described above are applied to study the behavior of PMB systems. Before continuing, the governing equations (Eq. (2.1a)–(2.1d)) are further analyzed in order develop a better understanding of the coupled system of equations, time-scales and physical stiffness of the system. First,

Eq. (2.1a)–(2.1d) are simplified by neglecting radiation and heat transfer through mass diffusion due to different species specific heats (second term on the right-hand-side of Eq. (2.1c)). The following simplified equations are derived:

$$\partial_t(\rho_g \epsilon) + \partial_x(\epsilon \rho_g u) = 0, \quad (2.6a)$$

$$\epsilon \rho_g (\partial_t Y_i + u \partial_x Y_i) = \underbrace{-\partial_x(\epsilon \rho_g D_i \partial_x Y_i)}_{\text{diffusion}} + \underbrace{\epsilon \dot{\omega}_i}_{\text{reaction rate}}, \quad (2.6b)$$

$$\epsilon \rho_g c_{p,g} (\partial_t T_g + u \partial_x T_g) = \underbrace{\partial_x(\epsilon \lambda_g \partial_x T_g)}_{\text{conduction}} - \underbrace{h_v(T_g - T_s)}_{\text{heat exchange}} + \underbrace{\epsilon \dot{q}}_{\text{heat release}}, \quad (2.6c)$$

$$\rho_s c_{p,s} \partial_t((1-\epsilon)T_s) = \underbrace{\partial_x((1-\epsilon)\lambda_s \partial_x T_s)}_{\text{conduction}} + \underbrace{h_v(T_g - T_s)}_{\text{heat exchange}}, \quad (2.6d)$$

If the fuel combustion is assumed to follow a global one-step mechanism:



represented in mass units, then the species conservation equations simplify to the following two equations for fuel and oxidizer mass fraction:

$$\epsilon \rho_g (\partial_t Y_F + u \partial_x Y_F) = \partial_x(\epsilon \rho_g D_F \partial_x Y_F) - \epsilon \dot{\omega}_F \quad (2.8)$$

$$\epsilon \rho_g (\partial_t Y_O + u \partial_x Y_O) = \partial_x(\epsilon \rho_g D_O \partial_x Y_O) - \epsilon \dot{\omega}_O \quad (2.9)$$

For ultra-lean mixtures, where the oxidizer mass fraction is assumed to be constant across the flame, the combustion reactants for a methane-air reaction are:



From the equivalence ratio  $\phi$  of the mixture, the initial mass fractions of fuel  $Y_{F,0}$  and oxidizer  $Y_{O,0}$  are found assuming the fuel is methane and the oxidizer is air:

$$\begin{aligned} W_F &= 16.04 \text{kg/mol} & Y_{F,0} &= \frac{1 + W_F}{(1 + \frac{2*4.76}{\phi})W} \\ W_O &= 28.96 \text{kg/mol} & Y_{O,0} &= \frac{\frac{2*4.76}{\phi}W_O}{(1 + \frac{2*4.76}{\phi})W} \\ W &= \frac{1 + W_F + \frac{2*4.76}{\phi}W_O}{1 + \frac{2*4.76}{\phi}} \end{aligned}$$

The species reaction rate term is modeled using the Arrhenius law and the heat release term is the fuel reaction rate scaled by the heat of reaction:

$$\dot{\omega}_F = A\rho_g^2 Y_O Y_F \exp \frac{-E_a}{R_u T_g} \quad (2.11)$$

$$\dot{q} = Q\dot{\omega}_F \quad (2.12)$$

Assuming constant porosity,  $\epsilon$ , the simplified governing equations (Eq. (2.6)) can be reformulated using the following non-dimensional variables and ratios:

$$\begin{aligned} Y_F^* &= Y_F(Y_{F,0})^{-1} & \theta &= (T - T_{g,0})c_{p,g}(Y_{F,0}Q)^{-1} \\ Y_O^* &= Y_O(Y_{O,0})^{-1} & \Delta\theta &= \theta_g - \theta_s & \text{Pe} &= u_0 a \alpha^{-1} \\ x^* &= xd^{-1} & T_r &= Y_{F,0}Qc_{p,g}^{-1} + T_{g,0} & \text{Nu} &= h_v d(a\lambda)^{-1} \\ t^* &= tu_0d^{-1} & \gamma &= E_a(R_u(T_{g,0} + Y_{F,0}Qc_{p,g}^{-1}))^{-1} & \text{Da} &= du_0^{-1}(A\rho_{g,0}Y_{O,0} \exp -\gamma) \\ \rho^* &= \rho\rho_0^{-1} & \beta &= (1 + \gamma(T_r)^{-1}(\theta_g Y_{F,0}Qc_{p,g}^{-1})) \end{aligned}$$

The Arrhenius reaction term,  $\dot{\omega}_F$ , is linearized using a first-order Taylor series expansion about the reduced temperature,  $T_r$ .

$$\dot{\omega}_F \approx A\rho_g^2 Y_O Y_F \exp(-\gamma)(1 + \gamma(T_g - T_r)T_r^{-1})$$

The Damköhler, Da, number is the ratio of the residence time of the flow to the chemical time scale. Péclet, Pe, number is ratio of the rates thermal energy convected to that conducted within each phase. In this analysis, the diffusivities of the two phases are matched to equate Pe numbers. Lastly, the Nusselt, Nu, number

is the ratio of convective to conductive heat transfer normal to a boundary. Typically, this number is defined with respect to the fluid phase properties. In this problem, Nusselt number is defined with respect to both phases.

$$\rho_g^* (\partial_t^* Y_F^* + u^* \partial_x^* Y_F^*) = Pe_g^{-1} \partial_x^* (\rho_g^* \partial_x^* Y_F^*) - Da\beta \quad (2.13)$$

$$\rho_g^* (\partial_t^* \theta_g^* + u^* \partial_x^* \theta_g^*) = Pe_g^{-1} (\partial_x^{2*} \theta_g^* - Nu_g \epsilon^{-1} \Delta\theta) + Da\beta \quad (2.14)$$

$$\rho_s^* \partial_t^* \theta_s^* = Pe_s^{-1} (\partial_x^{2*} \theta_s^* - Nu_s (1 - \epsilon)^{-1} \Delta\theta) \quad (2.15)$$

$$\partial_t(\rho_g^*) + \partial_x(\rho_g^* u^*) = 0 \quad (2.16)$$

Substituting the following values, corresponding to representative gas and solid phase parameters:

$$\begin{aligned} A &= 2.2 * 10^{13} [m^3 kg^{-1} s^{-1}] & Pe &= 100 \\ Q &= 4.255 * 10^7 [m^3 kg^{-1} s^{-1}] & Nu_g &= 100 & T_r &= 1000 \\ h_v &= 2 * 10^7 [W m^{-3} K^{-1}] & Nu_s &= 0.04 & \gamma &= 10 \\ E_a &= 1.77 * 10^5 [J mol^{-1}] & Da &= 10^7 & \beta &= 1 + 15\theta_g \\ \Delta\theta &= 1000 \end{aligned}$$

results in the following scaling of the simplified governing equations:

$$\partial_t(\rho_g^*) + \partial_x(\rho_g^* u^*) = 0 \quad (2.17)$$

$$\rho_g^* (\partial_t^* Y_F^* + u^* \partial_x^* Y_F^*) = \underbrace{Pe_g^{-1}}_{10^{-2}} \partial_x^* (\rho_g^* \partial_x^* Y_F^*) - \underbrace{Da}_{10^8} \beta(\theta_g) \quad (2.18)$$

$$\rho_g^* (\partial_t^* \theta_g^* + u^* \partial_x^* \theta_g^*) = \underbrace{Pe_g^{-1}}_{10^{-2}} \partial_x^{2*} \theta_g^* - \underbrace{Pe_g^{-1} Nu_g \epsilon^{-1}}_{10^3} \Delta\theta + \underbrace{Da}_{10^8} \beta(\theta_g) \quad (2.19)$$

$$\rho_s^* \partial_t^* \theta_s^* = \underbrace{Pe_s^{-1}}_{10^{-2}} \partial_x^{2*} \theta_s^* - \underbrace{Pe_s^{-1} Nu_s (1 - \epsilon)^{-1}}_{10^{-1}} \Delta\theta \quad (2.20)$$

This analysis illustrated the ten orders of magnitude difference in the relevant time scales in the problem, and exhibits four orders of magnitude difference in the

heat transfer rate between the two phases, due to the much higher heat conductivity of the solid phase, as quantified by the Nusselt numbers. Furthermore, it reveals the relevant non-dimensional parameters controlling the coupled heat transfer in a PMB (i.e.Da, Nu, Pe, St=Nu/Pe) . The influence of the porous media morphology on these parameters, specifically the Stanton number, St, is explored in further in Chapter 5.

In subsequent chapters, the model and computational framework described above are implemented and used in conjunction with experimentation to investigate the behavior of PMBs.

# Chapter 3

## Investigation of lean combustion stability, pressure drop, and material durability in porous media burners \*

### 3.1 Motivation

Increasingly stringent emission requirements for gas-turbine engines and other energy systems motivate novel combustion system designs that enable reliable operation near the fuel-lean flammability limit. Lean premixed combustion mitigates emissions and efficiency concerns related to incomplete mixing of fuel and air, but can also lead to thermo-acoustic instabilities and other undesirable phenomena such as flashback and blow-off. Proper flame stabilization is a critical safety and reliability concern, which highlights the need for innovative combustor concepts.

In this chapter, the operational stability and thermal durability of combustion in

---

\*This chapter contains previously published work ([Sobhani et al. 2017](#)), adapted here with only minor modifications. Bret Haley, Dave Bartz, and John Sullivan at the Alzeta Corporation contributed to the experimental work presented.

conventional two-zone “step” PMBs is examined experimentally and computationally. In the first step towards testing the viability of this burner for application to aviation gas-turbine engines, the effects of the solid matrix material and geometric properties on flame stability are studied at atmospheric conditions with gaseous methane fuel. Two materials of different thermal conductivities, namely YZA and SiC, are tested in five different configurations and across a range of equivalence ratios and mass flow rates to identify trends in flame stability behavior. Additionally, the accuracy of volume-averaged models for predicting the temperature distribution and pressure drop in PMBs is examined. The temperature predictions of a 1D volume-averaged model with detailed chemistry are assessed against thermocouple measurements from the burner. Pressure drop is computed with the Darcy-Forchheimer equation ([Philipse and Schram 1991](#)), using Ergun’s relations for the drag and permeability coefficients ([Ergun and Orning 1949](#)), and compared to experimental measurements. Furthermore, to determine durability, the burner design with optimal pressure drop and stability properties was tested at steady-state and cycled on-off conditions.

In the following, the experimental setup is described in Section [3.2](#); the numerical model is described in Section [3.3](#), and results for combustion stability, temperature profiles, emissions, pressure drop and material durability are presented in Section [3.4](#). A summary is presented in Section [3.5](#).

## 3.2 Experimental apparatus and procedure

The present study utilizes ceramic reticulated foams due to their high porosities and consequently low pressure drops. The ceramic reticulated foams used in the upstream and downstream sections of the PMB are varied in the experimental investigation. Samples of SiC and YZA were used in five different arrangements, as summarized in Table [3.1](#). The reticulated SiC foams (Ultramet, Pacoima, CA) are made using chemical vapor deposition (CVD) of SiC, which coats the ligaments of the underlying non-crystalline vitreous carbon foam structure. The YZA foams (Selee Corporation, Hendersonville, NC), similar to the underlying carbon foam of the SiC, are made via the sponge replication process and are composed of 62% zirconia, 33% alumina, 2%

yttria and 3% calcia. Figures 3.1 and 3.2 show the relative similarity between the two structure topologies and also illustrates the difference between the circular pores of the YZA and the polygonal pores of the SiC. Furthermore, from inspection, the presence of closed pores in the YZA sample is evident, which can affect the pressure drop and flow behavior. For the five different pore densities used, ranging from 3 to 65 PPI, the porosity of the samples varies linearly between 91% to 83%, respectively. The solid thermal conductivity of YZA foams is 0.30 W/(mK) and that of the SiC ( $\epsilon = 0.9$ ) is near 1.5 W/(mK)(Selee and Ultramet manufacturer data).

The porous media specimens were stacked in a castable alumina tube (Western Industrial Ceramics, Santa Fe Springs, CA) and wrapped in ceramic paper (Unifrax, Tonawanda, NY) for sealing and insulation.

Burner	Upstream Flame-Arrestor	Downstream Combustion Section
1	SiC, 65	SiC, 10
2	YZA, 60	SiC, 10
3	YZA, 40	SiC, 10
4	YZA, 40	YZA, 10
5	YZA, 40	SiC, 3

Table 3.1: Specifications of configurations and pore density (PPI) of the five burners. Burners were composed of two porous samples in the upstream sections and one in the downstream sections; each sample has a height of 2.54 cm.

The experiments were performed using natural gas, composed of about 95% methane, 4% ethane, 1% carbon dioxide and <1% of other hydrocarbons, based on molar concentration. Upstream, the fuel and air streams are properly mixed by first converging within a tee-fitting, then flowing through a length equal to 63 pipe diameters, including four 90° elbows, before entering the apparatus (Fig. 3.3 for schematic and Fig. 3.4 for image of test facility). Premixed air and natural gas are supplied to the burner and ignited at the 0.32 cm steel plate downstream of the porous media. The flow conditions for stable operation of the reaction are subsequently investigated. The occurrence of flame instability in PMBs is challenging to identify experimentally since it is a gradual process, unlike a free flame that extinguishes immediately after the system reaches an imbalance with the flame speed. In this study, stable operation

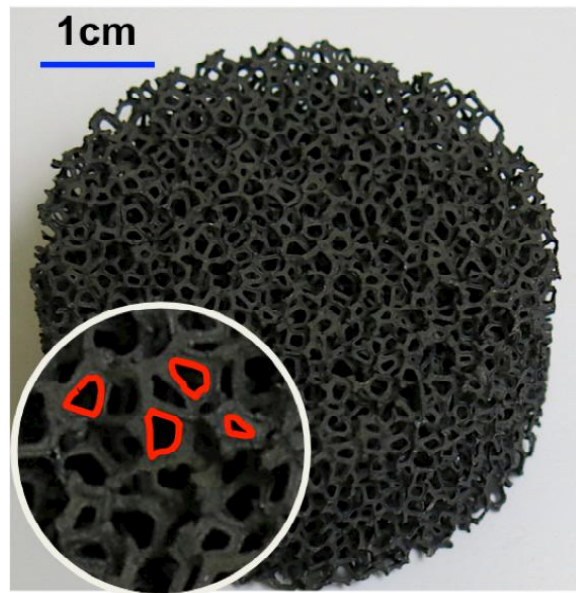


Figure 3.1: SiC 10 PPI, the ceramic reticulated foam used in the combustion zone of Burners 1-3, with a few pores outlined to illustrate the polygonal pore geometry of the SiC foams.

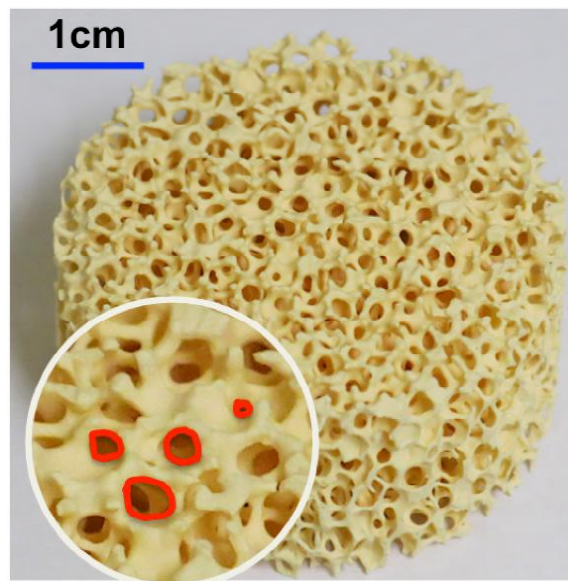


Figure 3.2: YZA 10 PPI, the ceramic reticulated foam used in the combustion zone of Burners 4, with a few pores outlined to illustrate the circular pore geometry of the YZA foams.

is identified as a stationary flame within the downstream combustion section, determined by measuring the temperature along the flow axis. Flashback was recorded if the temperature detected by the thermocouple upstream of the interface surpassed 755 K. Blow-off occurred in two stages. During the first stage of blow-off, the flame departs from the interface between the upstream and downstream sections, which is detected by a sharp decrease in temperature near the interface. This behavior is followed by partial or total departure of the flame-front from the downstream section, which is detected visually. For stability tests, adjustments in the mass flux and equivalence ratio were made until the flame indicated either flash-back or blow-off. To check repeatability, the high mass-flux limit (i.e. blow-off) was repeated at least 3 times, and the low mass-flux limit (i.e. flash-back) was repeated at least 2 times for each equivalence ratio value. Within each series, blow-off or flash-back generally occurred at the same circumferential position, and variations in mass-flux at the point of instability were generally within 5-10%.

To measure the flow rate, five rotameters (Dwyer Magnehelic, Michigan City, IN) were utilized; two for natural gas, and three for air. Rotameters with the smallest maximum flow rate that fit the test series were used for each experiment. Two differential pressure gauges were used; the first measured the combustion air pressure at the rotameter exits, the second measured the pressure drop across the PMB.

The burner was instrumented with thermocouples, with a 90° separation azimuthally and 0.635 cm separation axially (Fig. 3.5). Two thermocouples were placed at each axial location with a 180° separation, but they slightly shifted axially during the experiment and their updated locations are reflected in the results (labeled A–D in Fig. 3.8). All thermocouples were mineral-insulated type-K units with standard limits (Watlow Gordon, Richmond, IL). Since only lean mixtures were tested in this experiment, thermocouples with higher temperature tolerances were not required. Grounded junction thermocouples measured axial temperatures and exposed junction thermocouples measured exhaust temperatures. All temperature data was captured with three Pico Technology TC-08 thermocouple data loggers.

Emissions were sampled with an ECOM EN2-F Portable Emissions Analyzer. The measured species, range, accuracy and resolution are as follows: O<sub>2</sub>, 0-21% by volume,

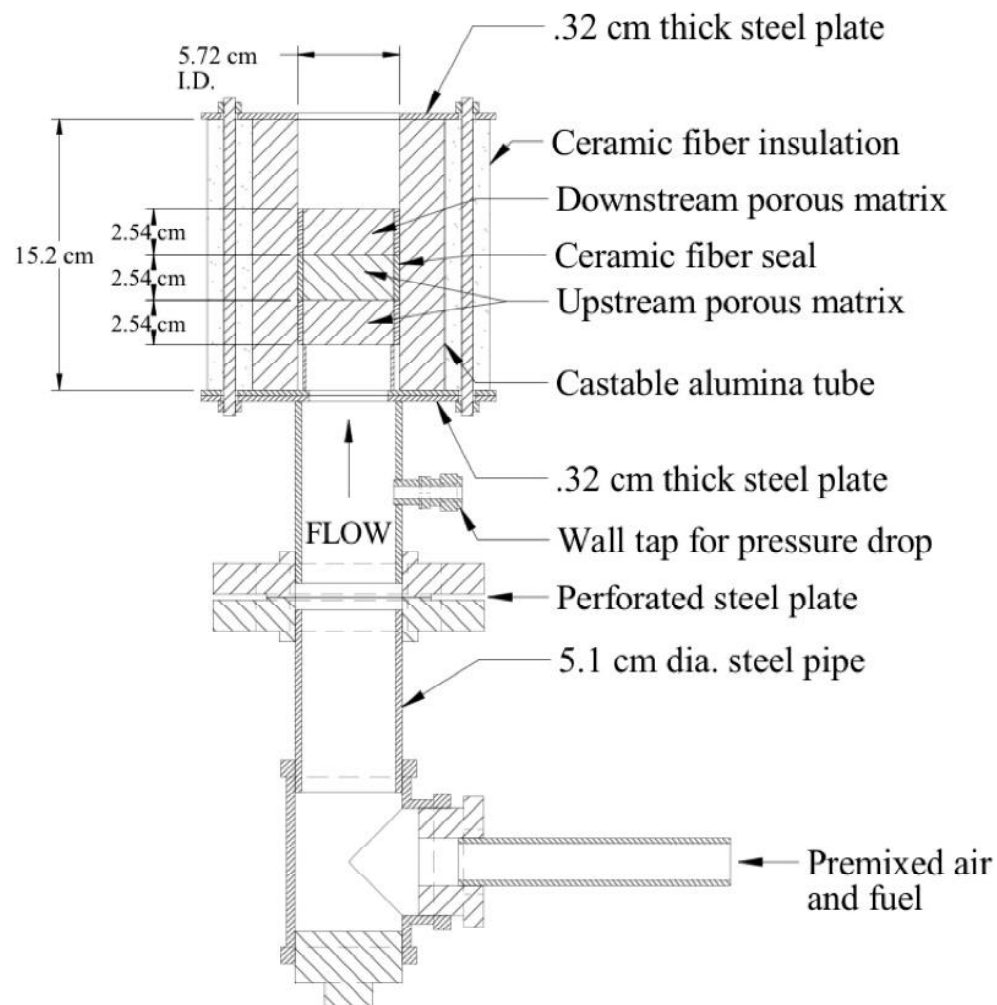


Figure 3.3: Cross-sectional schematic of experimental apparatus.

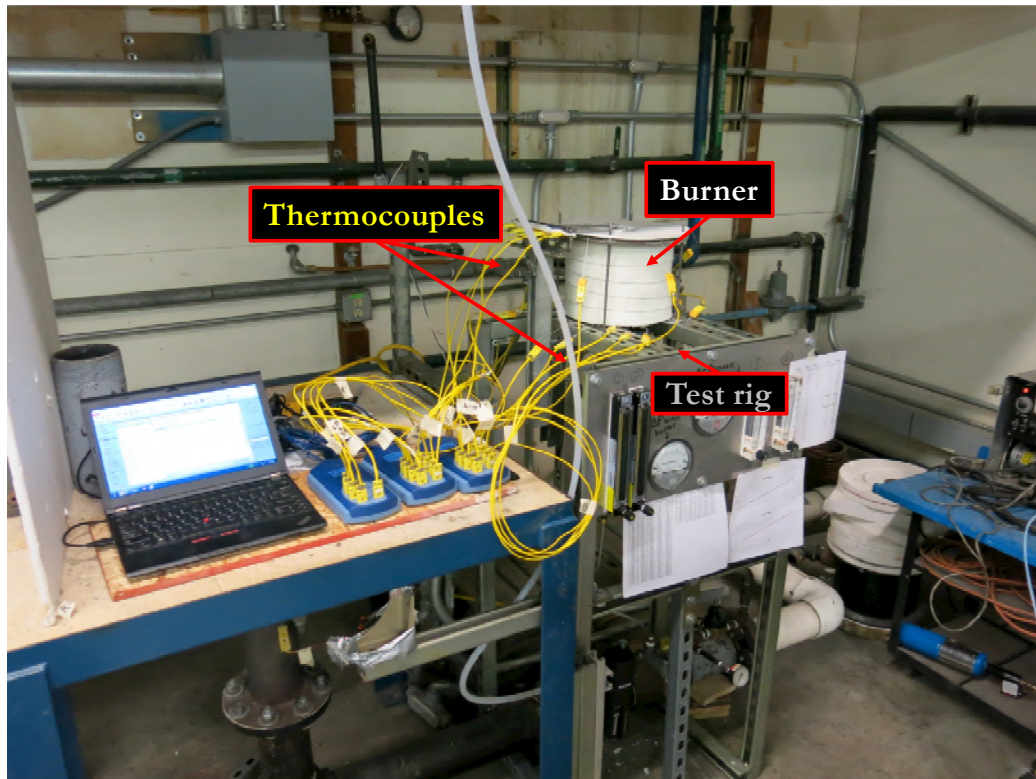


Figure 3.4: Image of the experimental setup at Alzeta with burner, thermocouples, and test rig.

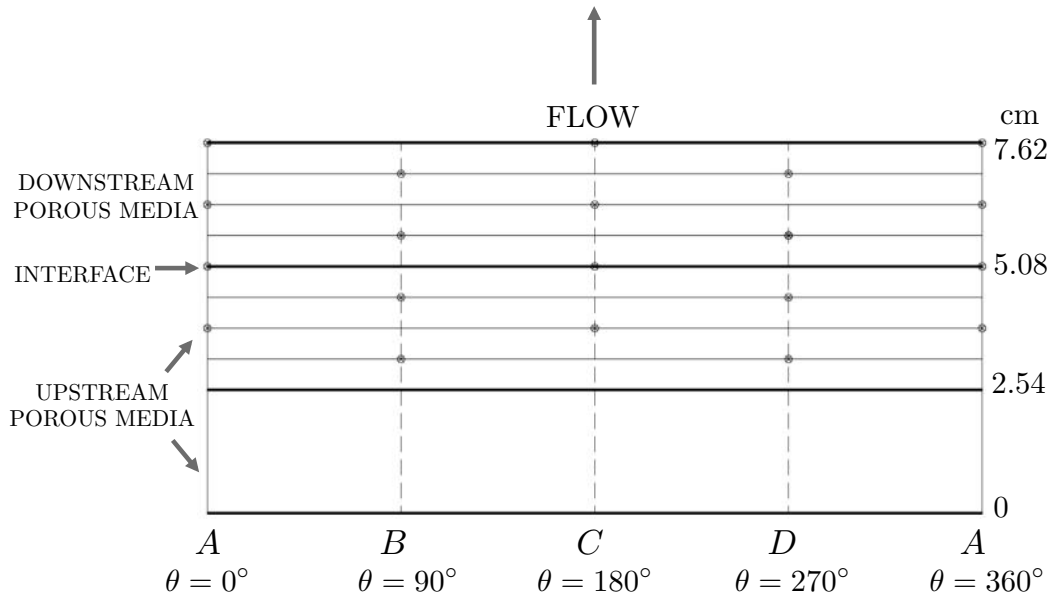


Figure 3.5: Location of the thermocouples, referred to as A-D, at the burner outer diameter.

$\pm 0.2\%$ ,  $0.1\%$ ; CO, 0-10,000 parts per million (ppm),  $\pm 2\%$ , 1 ppm; NO, 0-5000 ppm,  $\pm 5\%$ , 0.1 ppm;  $\text{NO}_2$ , 0-100 ppm,  $\pm 5\%$ , 0.1 ppm. An Ametek Thermoxy CMFA-P Portable Premix Analyzer (accuracy is the greater of  $\pm 2\%$  of measured and  $\pm 0.1\%$   $\text{O}_2$ ) was used to measure the  $\text{O}_2$ -content.

### 3.3 Numerical model

A computational study was conducted to compare model predictions for pressure drop and temperature against the experimental measurements. The equations governing the combustion in porous media (Eq. (2.1)) and the adapted CANtera ([Goodwin 1998](#)) 1D reacting flow solver used are described in Chapter 2.

The pressure drop was evaluated using the Darcy-Forchheimer equation with Ergun's relations, as described in Eq. (2.4) and (2.5) in Chapter 2. Ergun's empirical relations were developed for unconsolidated media made of solid spherical particles, therefore  $d_p$  in Eq. (2.5) refers to the particle diameter. These relations, along with most models used for the prediction of permeability parameters of ceramic foams,

are based on the particle diameter as the characteristic length scale. The major difficulty in applying these models to porous foams is in defining representative structural properties of a foam to replace the particle diameter in Ergun's model. [Philipse and Schram \(1991\)](#) first illustrated that Ergun-type permeability models based on granular media also apply to foams, simply by replacing the particle diameter with the pore diameter, extracted from image analysis, as the characteristic length. Several other attempts have been presented in the literature to replace the particle size in Ergun's relations. [Innocentini et al. \(1999\)](#) used the cylindrical form of the hydraulic diameter ( $d_h = 1.5\frac{1-\epsilon}{\epsilon}d_p$ ) to derive an effective particle diameter from the average pore size of the porous foam,  $d$ . The hydraulic diameter represents the ratio between the volume available for the flow to the total wetted surface. Here, it is assumed that the solid filaments of the porous foam structure are analogous to the particles of a granular media. [Dukhan and Patel \(2008\)](#) later proposed the reciprocal of the specific surface area ( $d_{SA}$ ) as the equivalent particle diameter, and showed good agreement with experimental measurements for metal foams. This method requires information from the manufacturer about the specific surface area of the foam.

Despite the importance and wide-spread use of ceramic foams in several fluid-flow applications, a relationship between their permeability and simple foam structure properties remains uncertain. To address this, the experimental data for pressure drop of this study are compared to the Ergun-type models proposed by [Philipse and Schram \(1991\)](#); [Innocentini et al. \(1999\)](#); [Dukhan and Patel \(2008\)](#).

The total pressure drop across the porous matrix can be obtained by integrating Eq. (2.4) along the axial direction:

$$\Delta P = - \int_0^x \left( \frac{\mu}{K_1 \rho \epsilon A} \dot{m} + \frac{1}{K_2 \rho} \left( \frac{\dot{m}}{\epsilon A} \right)^2 \right) dx , \quad (3.1)$$

recognizing that the thermoviscous and material properties depend on the spatial location, and using the superficial velocity expressed in terms of the mass flow rate,  $u_D = \dot{m}/(\epsilon A \rho)$ .

In the following, in addition to presenting results from experimentation of PMBs, the results from 1D simulations described above are compared against experimental

measurements to assess the accuracy of volume-averaged models applied to porous media combustion.

## 3.4 Results and discussion

### 3.4.1 Flame stability and temperature profiles

The five burners tested exhibited varying temperature profiles and stability regimes, associated with the unique thermal and geometric properties of the porous samples comprising the burners. The stability map for all five burners tested are shown in Fig. 3.6. With close to five times the thermal conductivity, SiC exhibits favorable flame stability properties when employed in the downstream reaction zone but conversely affects flame stability when employed in the upstream flame-arrestor zone. The small-pore, low-conductivity YZA foam was shown to be a superior upstream flame arrestor compared to SiC and permitted operation at higher levels of equivalence ratios and mass fluxes. The higher thermal conductivity of the SiC in the upstream section for burner 1 resulted in flash-back at lower values of equivalence ratio compared to all other burners. Burners 2, 3, and 5 have similar stability performances, with burner 5 achieving the highest mass flux and lowest pressure drop. Burners 1 and 4 had much smaller stability envelopes by comparison. Burner 1, with SiC for both zones of the PMB, was only stable at low mass flux and equivalence ratio test conditions. Burner 4 utilized YZA for both zones of the PMB and blow-off occurred at lower mass flux rates compared to burners 1-3 and 5.

Figure 3.7 illustrates the burner blow-off sequence with the flame first embedded in the porous matrix and then approaching the surface. The blow-off initially occurs only on one side of the burner, as evidenced by the cold reactant mixture reaching the top surface. The non-uniformity in the porous media is illustrated by the asymmetric behavior of the flame at blow-off and further confirmed by the temperature variations at each axial location. Azimuthal asymmetries in temperature, as high as 30%, are observed in all five burners and illustrated for burner 1 and 2 in Fig. 3.8. The source of non-uniformity in temperature and flow behavior is believed to be caused

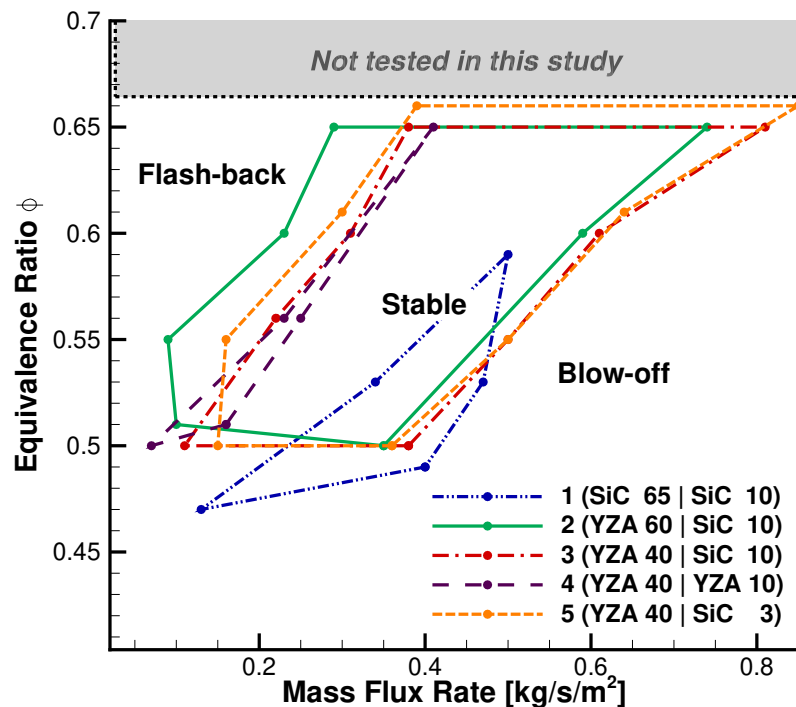


Figure 3.6: Stability map for all five burners, with stability maximized for burner 5. The data corresponding to this figure can be found in Table A.1 in Appendix A

by heterogeneities in porosity and pore distribution or pore-blockage in regions of the foam. Potentially, foams with homogeneous structures would enable the ideal uniform temperature distribution and better control of combustion stability.

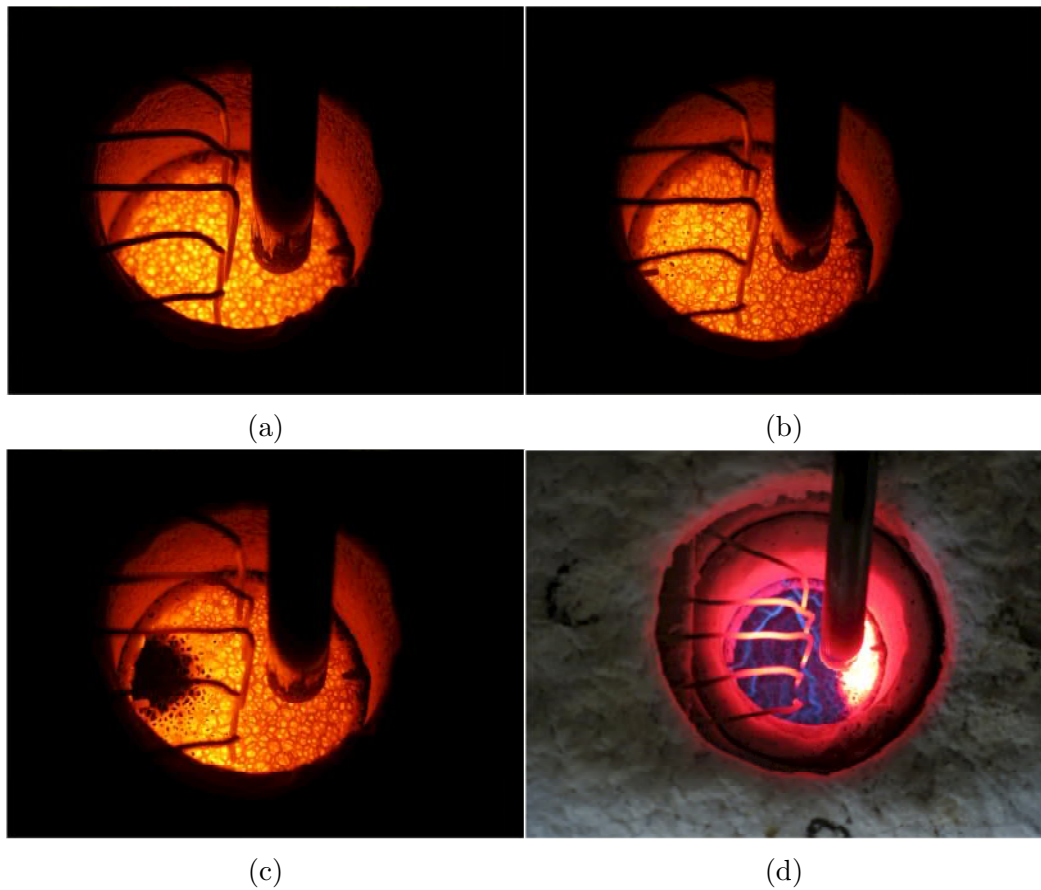


Figure 3.7: (a) Porous media burner during stable and (b)-(d) unstable blow-off operation. (b) The flame is approaching the top surface asymmetrically. (c) A portion of the cold reactant mixture has reached the top surface. (d) The flame has reached the top surface (i.e. blow-off). These images from above the burner illustrate the non-uniformity in flame behavior.

Figure 3.9 shows azimuthally averaged temperature measurements from thermocouples at each axial location in comparison to the volume-averaged numerical model. In general, trends in the predicted temperature profiles from the 1D model are in reasonable agreement with averaged experimental temperature measurements. It is

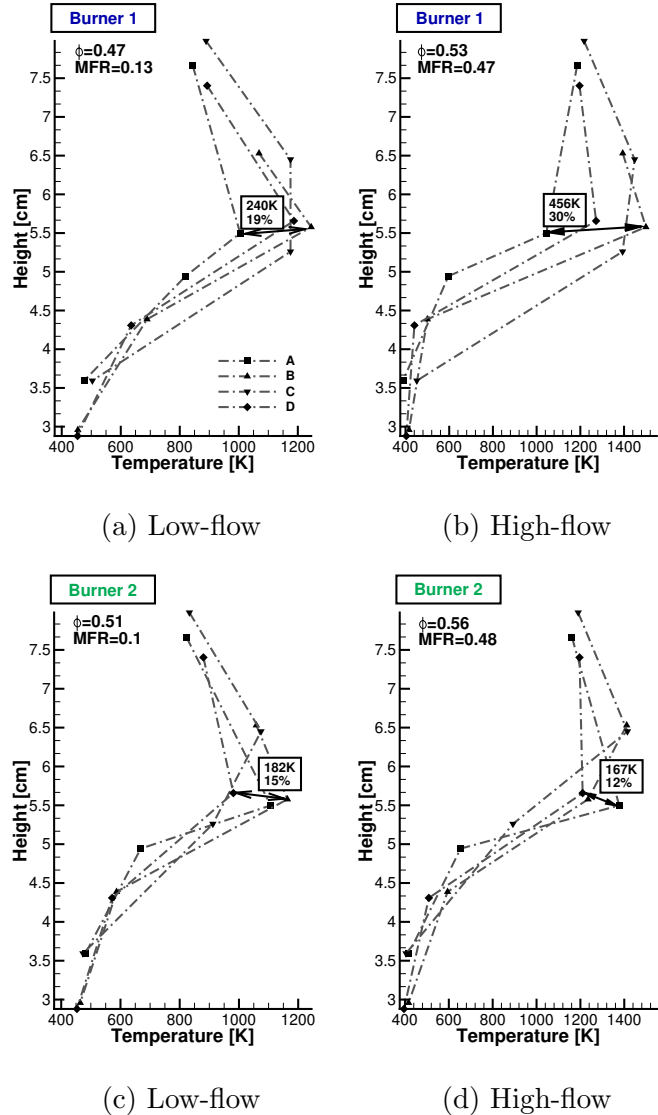


Figure 3.8: Temperature variations along azimuthal direction between thermocouples, referred to as A-D, at the same axial locations (Fig. 3.5). Maximum temperature variation between thermocouples less than 1 mm apart along axial direction is labeled along with percentage different compared to maximum temperature measured. The data corresponding to this figure can be found in Table A.9 in Appendix A

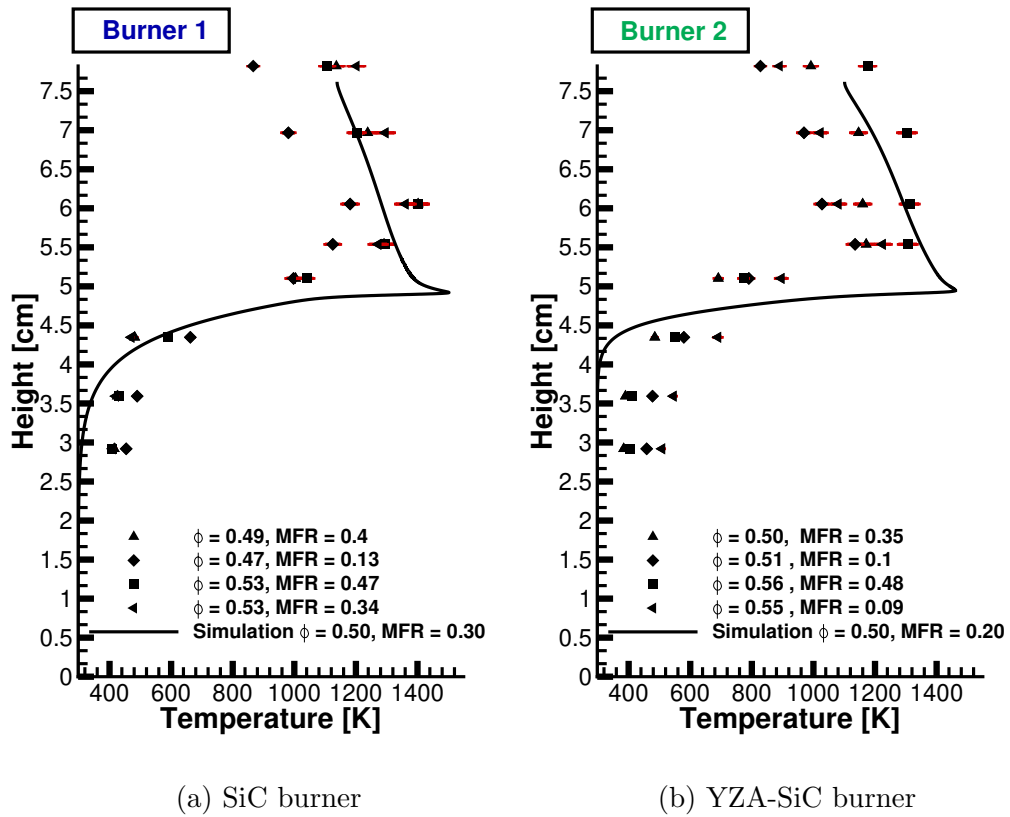


Figure 3.9: Averaged temperature measurements from four thermocouples compared to simulation results, described in Section 3.3 for burner 1 and 2 at various mass flux rates (MFR) and equivalence ratios  $\phi$ .

important to note that the thermocouple measurements only reveal the local temperature of the pore in which the thermocouple is placed. With only two thermocouples at each axial location, the measurements may not be representative of the temperature distribution. This is especially relevant in the flame-zone where alveolar flames significantly increase local temperatures. Although averaged temperatures from two point measurements are expected to deviate above or below that of the volume-averaged model predictions, the model consistently under-predicts temperatures in the upstream flame-arrestor section, both for the SiC and YZA samples. [Dunnmon et al. \(2016\)](#) reported similar trends for a SiC burner operated with methane. In this study, 3D XCT measurements were used to interpret the pore-scale temperature field, which was then cross-sectionally averaged and compared to a volume-averaged model. These comparisons also revealed a temperature under-prediction in the upstream section. Non-intrusive, 3D temperature measurements and detailed simulations can help shed light on the pore-scale physics in order to develop enhanced volume-averaged models and effective material parameters. Nonetheless, the model accurately identifies flame location, maximum temperatures, and exit temperatures, which are critical for designing integrated systems where downstream components are temperature sensitive.

### 3.4.2 CO and NO<sub>x</sub> emissions

Figure 3.10 shows NO<sub>x</sub> and CO emission measurements corrected to 3% O<sub>2</sub> for burners 1-3 and 5, at operating conditions near flash-back, blow-off, and stable flame regimes (Fig. 3.6). Emissions data for burner 4 are not presented due to poor stability performance, and therefore lack of sufficient data. All emissions are measured 3.2 cm above the top surface of the PMB at the centerline of the burner. At stable operating conditions, emissions of CO and NO<sub>x</sub> were generally low (<15 ppm). Figure 3.10(d) shows emissions during stable operation. For all conditions, NO<sub>x</sub> emissions increase with increasing equivalence ratios for all burners (Fig. 3.10(b,c)). This behavior is expected since more heat is released as equivalence ratio increases, enhancing both prompt and thermal NO<sub>x</sub> production pathways. CO emissions were approximately

or equal to zero near blow-off conditions, and therefore not shown in Fig 3.10. Conversely, CO emissions were highest near flash-back conditions, where oxidation rates decrease due to low temperatures ( $\sim 1000$  K). Therefore, incomplete combustion results in higher CO emissions. This phenomenon is most pronounced in burner 1, with peak CO emission of 950 ppm. The high thermal conductivity of the SiC in this burner facilitates rapid heat conduction away from the flame zone, potentially hindering CO oxidation. Measurements near the walls of the burner consistently showed higher CO emissions than centerline measurements, which further suggests the role of flame quenching both at the pores and at the walls of the burner. Figure 3.10(d) illustrates the trend in both CO and  $\text{NO}_x$  for burners 1-3 and 5 at a commonly stable operating condition of  $\phi = 0.5$ , MFR = 0.34. At this condition, all four burners operate in the regime between flash-back and blow-off, and therefore trends in emissions are attributed to the composition of the burner. The decreasing trend in CO emissions between burner 1 and 2, which are composed of different thermally conductive materials upstream, further illustrates the effect of the upstream section in facilitating reaction zone cooling and impedance of CO oxidation. In addition to the solid matrix heat transport properties, the upstream material pore density also has an effect on emissions. Between burner 2 and burner 3, upstream pore density decreases by 20 PPI, and the result is a decrease in CO emissions. Although the high pore density material in the upstream section of burner 2 extends the limit for flash-back as compared to burner 3 (Fig. 3.6), the enhanced flame quenching behavior results in higher CO emissions. Consistent with the trends found, stable emissions of burners composed of the same upstream material and pore density, are nearly identical (i.e. burners 3 and 5). Overall, burners with the highest range of stability (i.e. burners 2, 3, 5) exhibit ultra-low emissions characteristics, which is directly relevant to their impact in industrial applications.

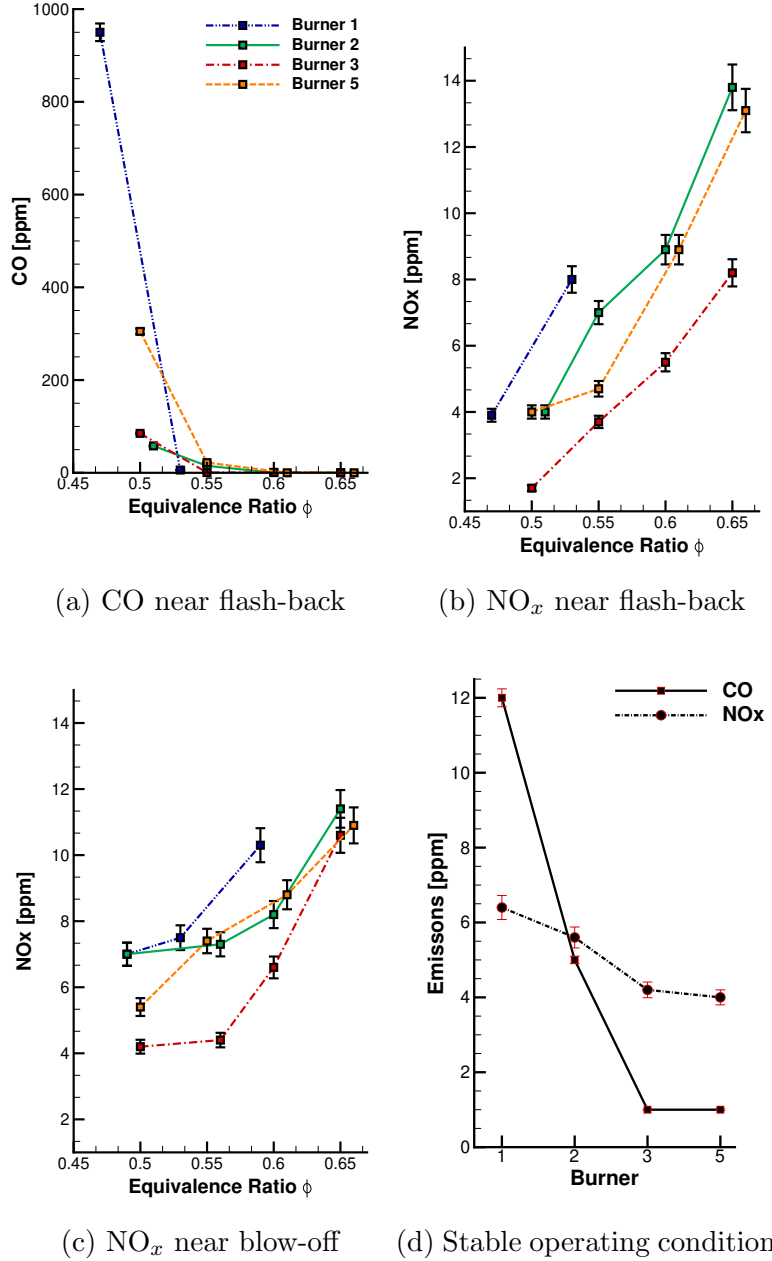


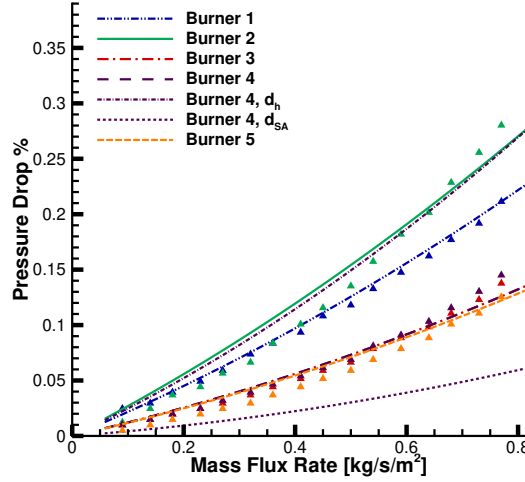
Figure 3.10: Emissions for burners 1-3 and 5, corrected to 3% O<sub>2</sub>. Blow-off, flash-back, and stable operating conditions for each burner correspond to Fig. 3.6. (a) CO emissions near flash-back conditions. CO emissions near blow-off not shown since all values are near zero. (b), (c) NO<sub>x</sub> emissions near flash-back and blow-off, respectively. (d) NO<sub>x</sub> and CO at a commonly stable operating condition of  $\phi=0.5$ , MFR=0.34. The data corresponding to this figure can be found in Table A.3 in Appendix A

### 3.4.3 Pressure drop

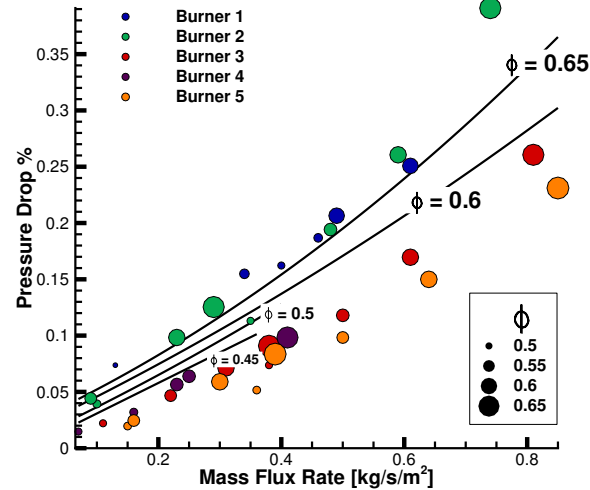
Pressure drop is analyzed from experimental measurements and simulation predictions. Pressure drop is minimized in burner 5 due to its composition of low pore-density and thus large pore diameter ceramic foams. For comparison with the Darcy-Forchheimer model, three different commonly used characteristic length scales are evaluated against the experimental data. Results show that computing Ergun's relations using pore diameter  $d$  from image analysis yields better agreement with experimental data, compared to other lengths scales found in the literature (i.e. the hydraulic diameter  $d_h$  and the reciprocal of specific surface area  $d_{SA}$ ). The cold flow pressure drop computed using all three length scales is illustrated in Fig. 3.11(a) for burner 4, since only the YZA manufacturer provided information about the specific surface area of the foam. Pressure drop calculations using  $d$  from image analysis for all other burners is also shown in this figure. Using the most suitable length scale identified, the predicted pressure drop shows reasonable agreement with the experimental data for both cold and reacting flows (Fig. 3.11). Results illustrate that all burner designs yield very low pressure drops well below 0.4%.

### 3.4.4 Durability testing

Two durability tests, continuous and cycle testing, were done for burner 5, which exhibited optimal pressure drop, emissions, and flame stability behavior. For the continuous test, the burner was operated over 419 hours at an equivalence ratio of 0.6 and a mass flux rate of  $0.5 \text{ kg}/(\text{m}^2\text{s})$ . The on-off cycle test was operated for 1229 cycles at the same mass flux rate as the continuous testing (Fig. 3.12). Thermocouples were used to measure the ambient temperature of the incoming reactants, upstream flame-arrestor section, and the interface between the flame-arrestor and downstream combustion sections. The operation cycle includes a 2-minute air purge, fuel addition to an equivalence ratio of 0.9, followed by an ignition. A standing pilot located at the top of the exhaust duct ignited the fuel-air mixture at the start of each cycle. After ignition, the temperature of the downstream element was monitored until the temperature in this section reached  $500^\circ\text{C}$ , after which the fuel flow was adjusted to an



(a) Cold flow all burners



(b) Reacting flow all burners

Figure 3.11: Comparison of predicted pressure drop (lines) and experimental results (symbols) for (a) cold flow conditions using three different characteristic lengths for burner 4 and the pore diameter from image analysis for all burners, and (b) reacting flow conditions, with comparison to computational results (lines) for geometry and material properties matching burner 2. Diameter of circles corresponds to equivalence ratio,  $\phi = 0.47\text{--}0.66$ . The data corresponding to this figure can be found in Table A.4 and A.5 in Appendix A

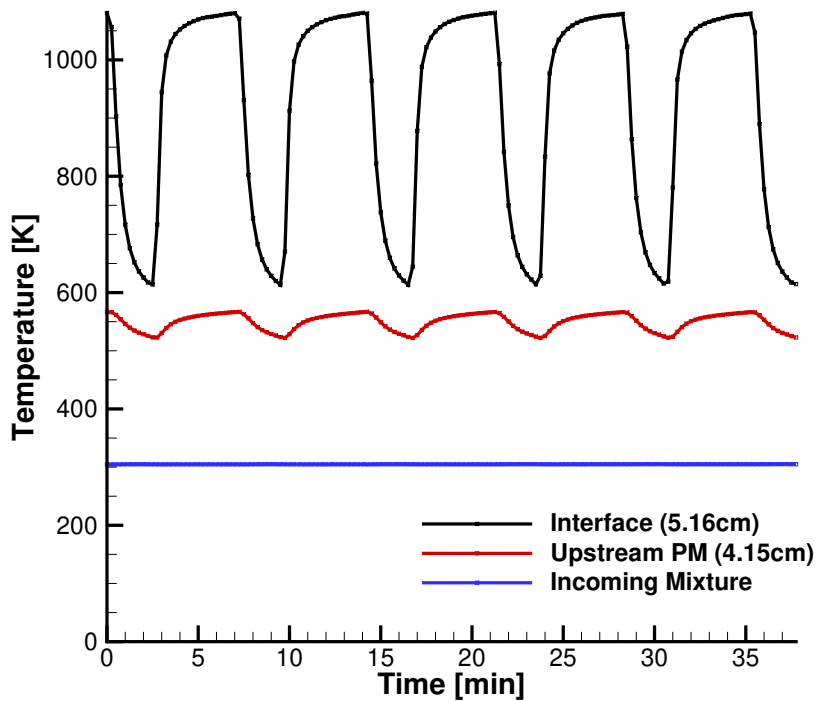


Figure 3.12: Temperature of PMB during cycle operation (1229 cycles total), showing 2 minute air purge, fuel addition, and ignition. Thermocouple locations are with respect to Fig. 3.5.

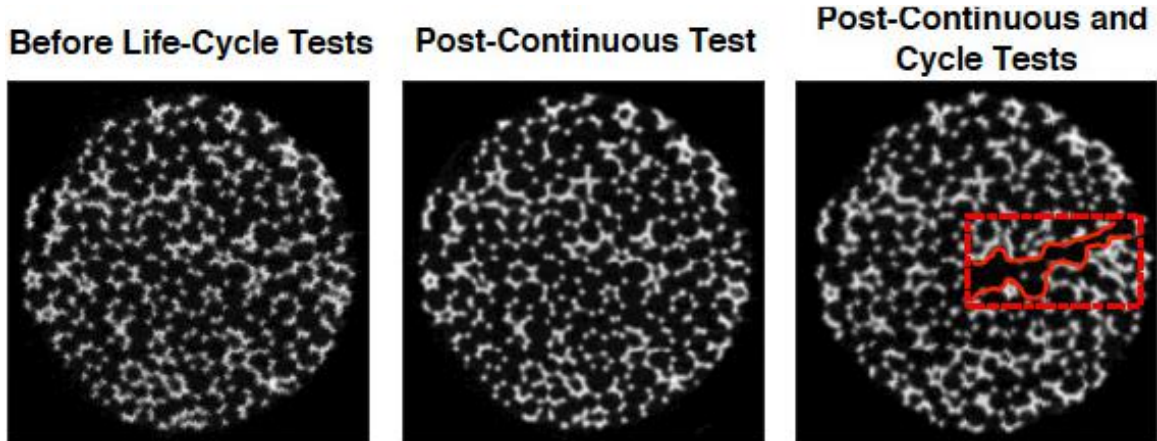


Figure 3.13: X-ray images showing cracking in the 3PPI sample of burner 5.

equivalence ratio of 0.6. The PMB then operates at this condition for 5 minutes, and the cycle repeats. During the continuous test over 419 hours in the combustion zone, the SiC matrix lost 1.4 grams, or 8% of total weight, from the oxidation of some of the carbon within the porous structure. Following the continuous life test, the YZA and SiC elements were undamaged, with no evidence of cracking or spalling. XCT scans of the 3 PPI SiC sample before and after the durability test were used to examine the internal structural integrity of the porous matrix. A representative view of the scans is shown in Fig. 3.13, where it is evident that the integrity of the porous media is preserved after the extensive continuous testing. Following the cycle tests, the SiC element had lost only 0.1 grams of mass, but the XCT scans revealed a crack in the porous matrix near the interface with the upstream section. The interface region is the location of the flame during stable operation. Therefore, thermal cycling of the material resulted in fractures where fluctuations in temperature are most extreme. Coating of carbon foams with reinforcing material can potentially eliminate cracking and achieve high structural strength in PMBs. Studies using coated carbon foams have successfully achieved combustion without incurring material degradation ([Marbach and Agrawal 2003; Vijaykant and Agrawal 2007](#)).

### 3.5 Summary

In this chapter, the flame stability, pressure drop, CO and  $\text{NO}_x$  emissions, and material durability of 5 PMBs were tested and compared to 1D volume-averaged simulation results. Material durability testing was also conducted for a burner made of 3 PPI SiC downstream section and a 40 PPI YZA upstream section. Long-term material durability tests at constant and cycled on-off conditions were done to investigate the feasibility of these materials in industrial applications. Although the 3 PPI SiC in the downstream combustion zone exhibited superior pressure drop and stability behavior, local cracks developed in the flame region during the cycle testing.

The results from the combustion experiments illustrate that the optimal configuration for minimizing pressure drop and maximizing flame stability is achieved using low

heat conductive YZA upstream and high-conductive SiC downstream.  $\text{NO}_x$  measurements were observed to increase at higher equivalence ratios and CO emissions were highest at lower flow rates, where low temperatures hinder complete CO oxidation.  $\text{NO}_x$  emissions were all below 14 ppm. The results reinforce concepts in PMB design and optimization, and demonstrate the potential of PMBs to overcome technological barriers associated with conventional free-flame combustion technologies.

# Chapter 4

## Experimental investigation of lean premixed pre-vaporized liquid-fuel combustion in porous media burners at elevated pressures up to 20 bar \*

### 4.1 Motivation

In continuation of the study presented in the previous chapter, the potential of PMBs applied to aviation gas turbine engines is tested at engine-relevant conditions. As outlined in Chapter 1, most of the existing literature on examining the operation of porous media combustion at elevated pressures has been limited to gaseous fuels, while investigations of liquid fuels only consider atmospheric pressure conditions. By addressing this gap, the objective of this study is to experimentally examine the performance of an “interface-stabilized” PMB that is operated with liquid fuel at

---

\*This chapter contains previously published work ([Sobhani et al. 2019a](#)), adapted here with only minor modifications. Jun Kojima, Clarence Chang, and Jeffrey Moder at the NASA Glenn Research Center contributed to the experimental work. Justin Legg, Dave Bartz, and John Sullivan at the Alzeta Corporation contributed to the burner design and testing.

high-pressure conditions. The design of the test rig and operating conditions were motivated by the expected pressure and temperature at the combustor inlet of a high-bypass ratio turbo-fan engine at cruise and take-off conditions to examine the viability of porous media combustion for application to aviation gas-turbine engines. The PMB was operated at fuel-lean equivalence ratios between 0.4–0.55 at pressures up to 20 bar with fully pre-vaporized and preheated n-heptane as well as gaseous methane at 8 bar for performance comparison. To focus on the combustion process and eliminate complexities associated with the liquid-fuel atomization, the fuel is pre-vaporized upstream of the burner. The experiment is instrumented with thermocouples, pressure sensors, and an exhaust-emissions probe to measure temperature profiles, pressure loss, and combustion products of CO and NO<sub>x</sub>. These measurements are complemented by numerical simulations using the volume-averaged, one-dimensional reacting flow-equations to provide insight about the effect of the pressure and fuel mixture on the flame structure. Results from these computational investigations are presented in the next section. The experimental setup and results from the high-pressure measurements are discussed in Section 4.3 and 4.4. To provide insights into the structural integrity of commonly used ceramic foams in PMBs, pre- and post-combustion analysis of the porous structure using high-resolution XCT is presented and discussed in Section 4.5. Finally, conclusions are presented in Section 4.6.

## 4.2 Computational analysis

To provide a general understanding of the high-pressure effects on the flame structure, numerical simulations of the PMB were performed at experimentally-studied conditions. The equations governing the combustion in porous media are derived by volume-averaging of the transport equations for a chemically reacting gaseous system (Kaviany 1991). Numerical simulations were performed using the Cantera 1D reacting flow solver, which was adapted to account for the coupling between the gas and solid phases in the PMB calculations. The reaction chemistry was modeled using a 68-species skeletal mechanism for n-heptane (Lu et al. 2009) and the DRM-19 mechanism, derived from the GRI-Mech 1.2, for methane (Kazakov and Frenklach 1994).

More details on the governing equations, model assumptions, and the computational method can be found in Chapter 2.

In the simulations, the inlet temperature was 470 K and the operating pressure varied from 2 to 20 bar to match the experimental conditions. Both of the chemical mechanisms implemented have been previously validated at elevated pressures for the fuel-lean conditions tested (i.e.  $\phi = 0.57$ ). The upstream flame-arrestor section was modeled as a 5.08 cm porous material with 82% porosity, 0.25 mm pore size, and 0.30 W/mK thermal conductivity. The downstream section combustion was 2.54 cm in length, 89% porosity, 1.1 mm pore size, and 1.5 W/mK thermal conductivity. The material, length, pore size, and porosity distribution of the burner in the simulation were chosen to match those of the experiment, as described in Section 4.3.

Figure 4.1 shows comparisons of the flame profiles between free flames and PMBs for a range of pressure conditions and mass flux rates. In the governing equations, the gas and solid temperatures are coupled by the convective heat transfer,  $h_v(T_g - T_s)$ . Therefore, in addition to the gas and solid temperature profiles, the heat transfer coefficient,  $h_v$ , is presented in Fig. 4.1c to give insights into the effects of pressure on the flame. First, Fig. 4.1a illustrates the temperature profiles of n-heptane free flames at 2, 8, and 20 bar, as well as methane at 8 bar, all at  $\phi = 0.57$ . The results indicate a  $\sim$ 50 K difference in flame temperature in the methane 8 bar flame, as compared to n-heptane, and small differences with increasing pressure near the reaction zone. However, the results show appreciable differences in the flame structure for PMB-flames. First, as shown in Fig. 4.1b, at a fixed mass flux rate of 0.3 kg/(m<sup>2</sup>s) and increasing pressure, the exit temperature for the n-heptane flames has a non-monotonic behavior, first increasing then slightly decreasing. At 2 bar, the flame has a smaller preheat zone and an appreciable temperature peak in the reaction zone. At 8 bar, this peak flattens out and the temperature profile broadens. This trend extends to 20 bar, where the preheat temperatures are further increased and the profile is flatter and more distributed. This behavior can be predicted using the modified Péclet number, which characterizes the ratio of heat release from the flame to heat removal in a PMB:

$$\text{Pe}_{S_l} = \frac{S_l L}{\alpha_g}, \quad (4.1)$$

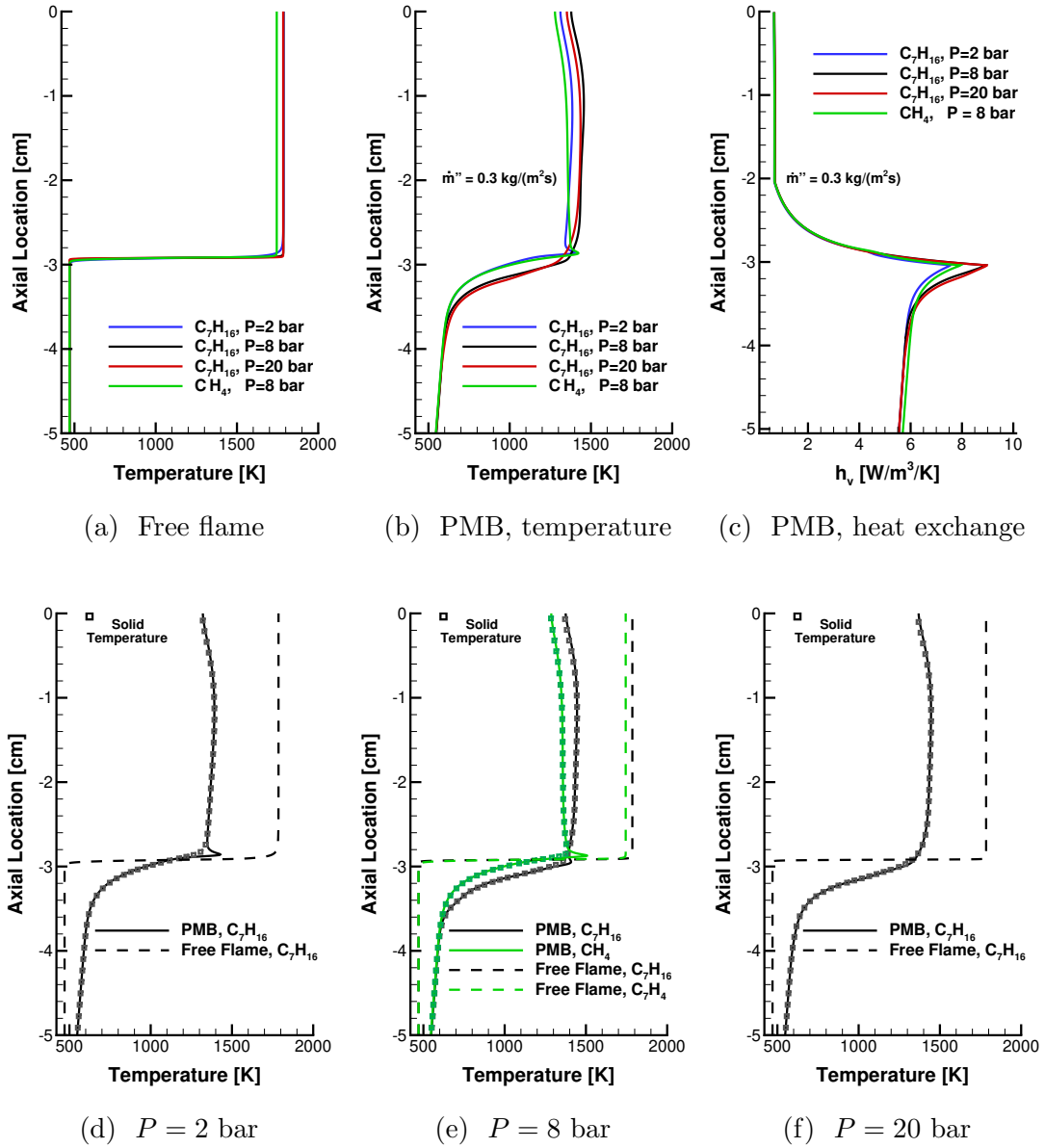


Figure 4.1: Computational profiles at  $\phi = 0.57$  of (a),(b) gas temperature for free flames and PMB, and (c) heat transfer coefficient in PMB. In (d)-(f), the mass flux rate in the PMB simulation corresponds to that of the n-heptane free flame at 2, 8, and 20 bar, equal to 0.4, 0.87, and 1.34  $\text{kg}/(\text{m}^2\text{s})$ , respectively and 0.47  $\text{kg}/(\text{m}^2\text{s})$  for methane at 8 bar. Symbols indicate the predicted solid-phase temperature.

where  $L$  is the characteristic length scale, and  $\alpha_g$  is the gas thermal diffusivity. The dependence of the laminar flame speed and diffusivity on pressure can be approximated as  $P^{-0.5}$  and  $P^{-1}$ , respectively. Thus, the ratio of heat release to heat removal increases with increasing pressure ( $\text{Pe} \propto \sqrt{P}$ ), which increases the preheat zone temperatures. Furthermore, the heat exchange between the solid and gas phase increases with increasing pressure, as shown in Fig. 4.1c, thus leading to enhanced heat recirculation and more distributed temperature profiles. Although the critical modified Pécelt number for quenching in porous media can vary, depending on the gas composition and solid matrix temperature (Wawrzinek and Trimis 2004), a general scaling to elevated pressures can be identified. With the pore diameter as the characteristic length, the following relationship for the pore diameter is derived for matching the Pe number at pressure  $P$ :

$$\frac{d}{d_o} = \sqrt{\frac{P_o}{P}} , \quad (4.2)$$

For instance, to match the flame stability properties at an elevated pressure of 10 bar, an upstream porous material with  $\sim \sqrt{10}$  times smaller pores is needed to prevent flash-back.

It is evident that at the same equivalence ratio and mass flux rate, the methane and n-heptane flames differ significantly in structure, preheat length, and exit temperature. In Figs. 4.1d–4.1f, the free flame temperature profiles are compared to the corresponding PMB case, operated at the laminar flame mass flux, equal to 0.4, 0.87, and  $1.34 \text{ kg}/(\text{m}^2\text{s})$ , at 2, 8, and 20 bar respectively, for n-heptane and  $0.47 \text{ kg}/(\text{m}^2\text{s})$  at 8 bar for methane. Firstly, the effect of the porous media on the flame temperature profile is illustrated, primarily in increasing the preheat zone and changing the flame structure. Secondly, the predicted steady-state solid temperature profile is shown to closely resemble the gas temperature, except near the flame zone for conditions with low mass-flux rates. In the experimental study, thermocouple measurements, which measure the solid temperature, were used to approximate the flame location. These computational results, as well as previous experiments (Zheng et al. 2011), indicate that using thermocouple measurements of the solid-phase temperature yield sufficient approximations of the flame location.

With an understanding of the high-pressure effects on the flame structure through computational simulations, the high-pressure experimental investigations follow next. The experimental setup and the results from these measurements are discussed in the next section.

### 4.3 Experimental study

High-pressure combustion experiments were performed in the SE-5 flame tube facility at the NASA Glenn Research Center (GRC) (see Fig. 4.3 for illustration and Fig. 4.2 for burner schematic). This facility has been used in previous high-pressure combustion studies (Kojima and Fischer 2013; Kojima et al. 2016). The internal pressure was maintained by the cooling air flow provided by the central facility compressor (31 bar). The ambient-temperature cooling air was introduced in two locations: at the bottom of the rig for cooling the burner hardware and downstream of the burner to quench-cool the combustion by-products (< 5.0 kg/min). The rig pressure was controlled by a back-pressure valve mounted in the exhaust pipe, which was remotely operated by an auto-feedback process controller to stabilize the desired pressure within 3% deviations. The rig pressure was varied from 2 to 20 bar in the present work, although the burner rig could operate at above 30 bar.

The PMB tested in this study employs a two-zone “step” burner concept comprised of porous foams, which are characterized by pore density measured in pores per inch (PPI). In previous work (Sobhani et al. 2017), the PMB design for maximizing flame stability with minimal pressure drop for gaseous methane at atmospheric pressure was experimentally determined. This design consists of a 3 PPI SiC downstream section and two 40 PPI YZA elements upstream. The three foam components are each 5.08 cm in diameter and 2.54 cm in length and stacked vertically in a castable alumina tube and wrapped in ceramic paper for sealing and insulation. Details about the manufacturing and composition of the ceramic foams can be found in Section 3.2.

The PMB assembly with liquid-fuel vaporizer was fit into the vertical-standing, upward-flowing pressure vessel that has an internal diameter of 15 cm with four optical access ports. Note that the optical ports were not used for any observation purpose.

Coriolis mass-flow controllers were used to regulate the air and fuel flow rates and thus, controlled the mass flux and global equivalence ratios of the premixed mixture entering the PMB. The mass flow meters for air, CH<sub>4</sub>, and C<sub>7</sub>H<sub>16</sub> (liquid) have 2 to 100% range with maximum readings of 24 kg/h, 1 kg/h, and 1 kg/h, respectively. The flow metering accuracy was 0.5% per reading.

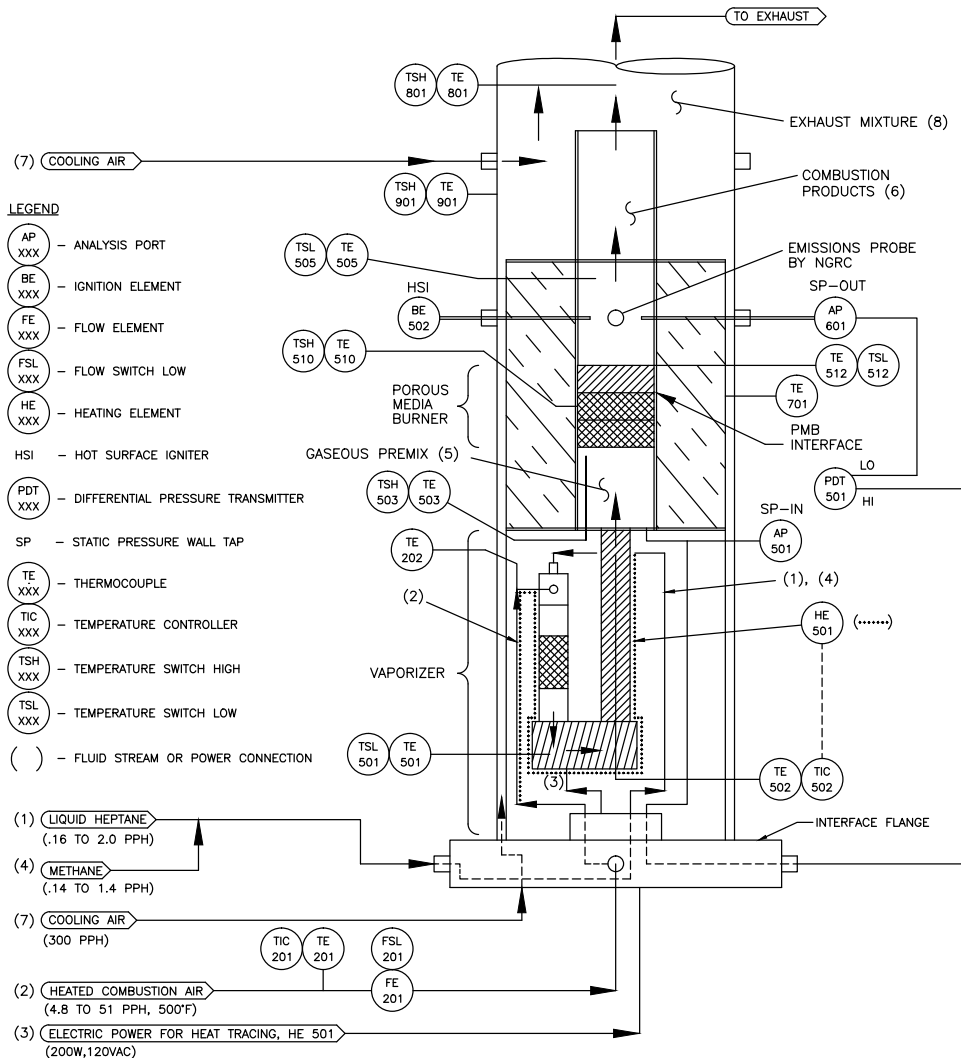


Figure 4.2: Schematic of PMB test hardware located inside the high-pressure test facility SE-5 at NASA GRC.

A schematic of the burner and flow system is shown in Fig. 4.2. A nitrogen-pressurized piston-cylinder fuel system delivered liquid n-heptane to the vaporizer,

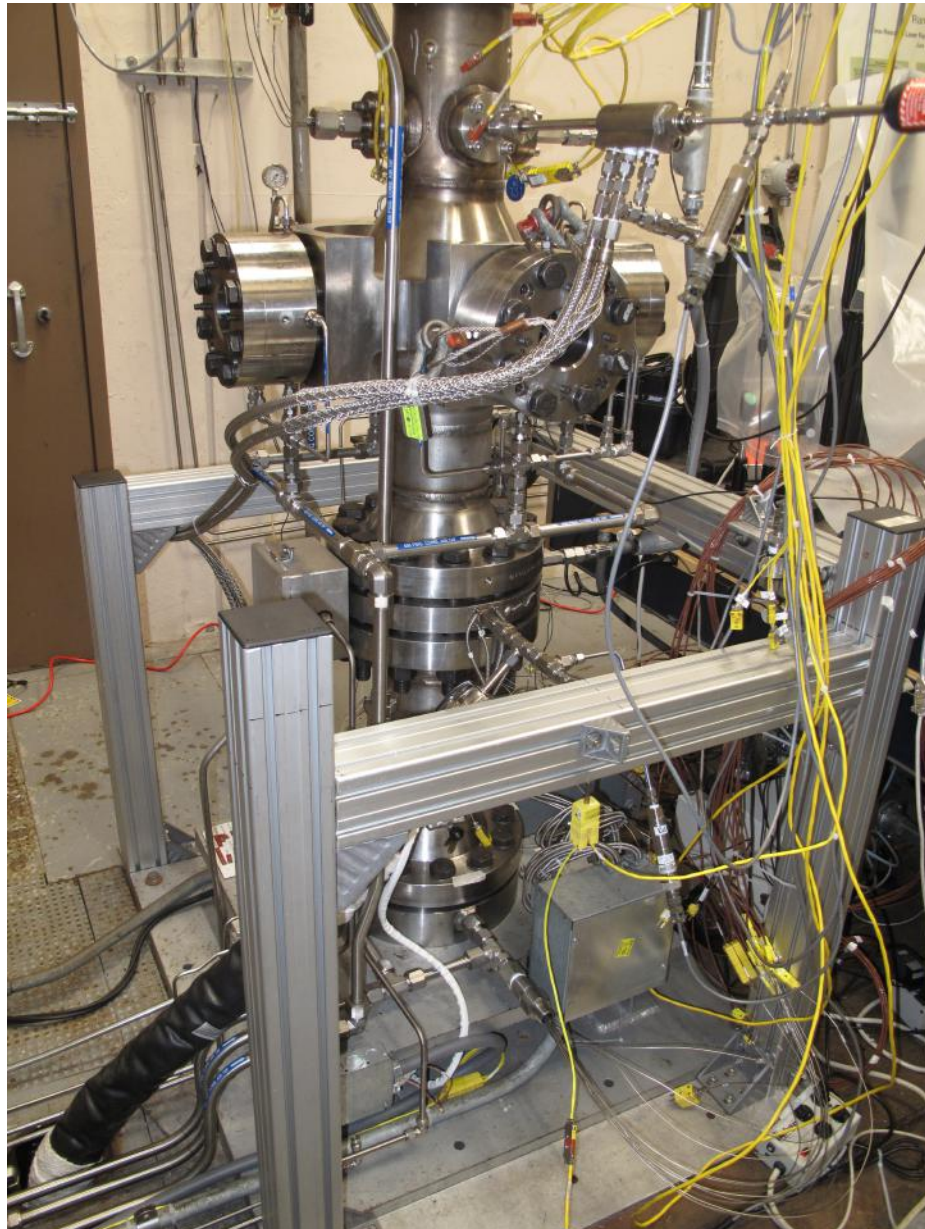


Figure 4.3: Image of the high-pressure test facility SE-5 at NASA GRC.

located upstream of the PMB. In the vaporizer, the liquid fuel was drip-fed to a packed column of length 16.5 cm and inner diameter of 1.57 cm filled with stainless-steel spheres (diameter 0.63 cm), which was heated by heat tracing to the desired temperature ( $\sim 500$  K) for complete vaporization. Methane fuel was separately (but never simultaneously with the other fuel) fed into the same packed column via a gaseous fuel delivery system with a compressed gas cylinder. Preheated ( $\sim 500$  K) and pressurized oxidizer air was also routed to the packed column in order to be premixed with the fuel vapor or gaseous fuel (see Fig. 4.2). Several tests were run to find the adequate length of the packed column to ensure complete vaporization of the fuel. The temperature at the exit of the packed column was monitored to ensure that the fuel/air mixture was formed without condensation or auto-ignition. After the packed column, the mixture flowed through a bend at the base of the system, then upward through a pipe of length of 29.2 cm to the PMB section. The exterior of this pipe was wrapped with electric resistance heat-tape that was controlled (see TE502 in Fig. 4.2) to provide a constant premixed gas temperature at the inlet to the PMB.

The PMB section was encased in alumina insulation (3.2 cm thick) and placed inside a stainless steel cylinder (12.7 cm outer diameter). Figure 4.4 illustrates the setup, with the top-most porous sample referred to as the downstream section and the bottom two samples acting as the upstream flame-arrestor. The temperature was measured using Watlow K-type mineral-insulated thermocouples, with a range of 368–1533K and standard limits ( $\pm 2.2$  K). The thermocouples were positioned at the outer perimeter of the burner, placed between the porous media and the ceramic insulation, to monitor the location of the flame at four circumferential quadrants and eight axial locations. One of the thermocouples (A-3) was damaged in early testing. The locations of the thermocouples are specified in Table 4.1, where each thermocouple is identified with a letter corresponding to its azimuthal location and a number corresponding to its axial location (see Fig. 4.4 for reference), measured from the SiC outlet surface. As found by Zheng et al. (2011), a thermocouple inserted inside a porous medium estimates the local solid temperature and the difference between such thermocouple measurements and gas phase temperatures are  $< 25$  K, except

near the reaction zone (also illustrated in the computational results in Section 4.2). As such, measured temperatures were used primarily for observing trends in flame location. Oxidizer air, fuels, thermocouples and electrical leads for heat tracing were fed through the base flange of the test rig. Instrumentation access ports were located above the PMB section and permitted insertion of a hot surface igniter, static pressure tap, and gas-emissions sampling probe.

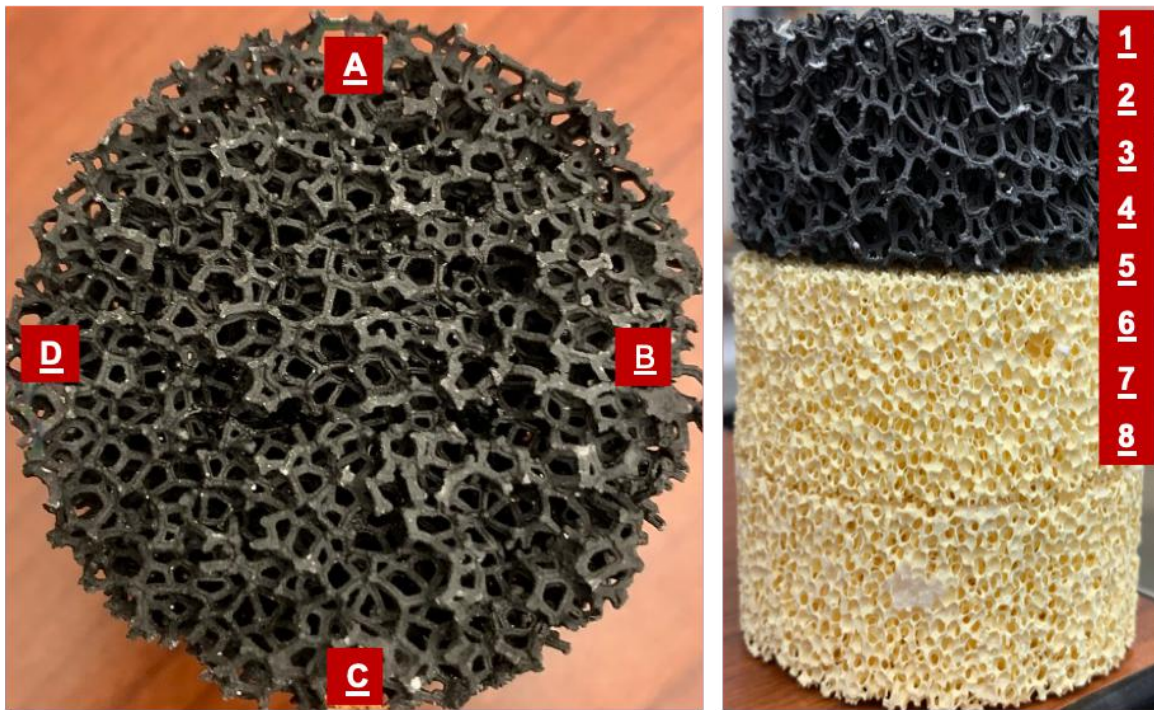


Figure 4.4: Azimuthal and axial locations of thermocouples, corresponding to values in Table 4.1, in SiC (black) element and YZA (yellow) elements. In the right image, the flow direction would be from the bottom to the top.

The exhaust of the PMB was sampled for emission measurements, then combined with cooling air before flowing into the pressure control valve downstream. As shown in Figs. 4.3 and 4.2, a nickel-plated stainless-steel sampling probe (12.7 mm outer diameter) was placed in the downstream section of the PMB to extract emissions from the exhaust gas via a single 0.8 mm diameter hole. The probe was designed to work with elevated pressures up to 41 bar and employed pressurized cooling water at flow rates ranging from 0.5 to 3.0 gal/min. The use of water cooling prohibits further

Thermocouple	Axial location	Element
A-1, C-1	0 cm	SiC
B-2, D-2	-0.64 cm	SiC
(A-3), C-3	-1.27 cm	SiC
B-4, D-4	-1.93 cm	SiC
A-5, C-5	-2.54 cm	YZA
B-6, D-6	-3.18 cm	YZA
A-7, C-7	-3.81 cm	YZA
B-8, D-8	-4.45 cm	YZA

Table 4.1: Axial locations of the thermocouples, measured from the outlet of the PMB. The thermocouples are positioned at the outer perimeter of the burner at azimuthal locations varying by  $90^\circ$  (see Fig. 4.4). Note that the thermocouple A-3 was damaged in early testing.

reactions of the exhaust products inside the probe. In a preliminary test, five exhaust samples near the walls and centerline over the surface of the PMB were measured, showing only small variations. Thus, the probe design and position in the test rig was assumed to have minimal contribution to the measurement uncertainty of the emission values. The gas pressure of the sample was reduced to slightly above the ambient pressure before it reached a portable gas analyzer (ECOM-EN2F), which measured concentrations of O<sub>2</sub> (0-21%), CO (0-4000 ppm), NO (0-5000 ppm), and NO<sub>2</sub> (0-1000 ppm), each with  $< \pm 5\%$  of measurement uncertainty. NO<sub>x</sub> was calculated as the sum of NO and NO<sub>2</sub>, each having a 5% accuracy of the measurement. NO<sub>x</sub> and CO were recorded as part per million by volume (ppm), corrected to 3% O<sub>2</sub> to standardize the effect of air dilution on concentration.

The mixture was ignited 5.4 cm downstream of the porous media. The flame was first stabilized at the outlet of the burner, until the matrix sufficiently heated up to enable the flame to propagate into the porous media. During operation of the embedded flame, emissions and pressure drop properties for a range of mass flux and equivalence ratios were tested. At a given operating condition, the PMB was identified as either stable or unstable, with the latter corresponding to either a blow-off or a flashback condition. The thermocouple measurements and CO emissions were used to track the flame location and stability. At a given equivalence ratio,

the boundaries of stability were determined by changing the mass flux by increments of 10%. To establish a new equivalence ratio, the flow conditions were changed by increments of 5% to find the stability boundaries. A stable operating condition was identified when the flame remains inside the SiC element (see Table 4.1 for axial locations) and all temperature measurements remain constant in time. Blow-off was identified by the formation of CO, and a large decrease in temperature at all four quadrants near the surface (thermocouples A-D at location 1). At certain conditions, a decrease in temperature was observed in only one or two of the four quadrants, without associated CO formation to indicate quenching of the flame. Thus, these conditions were identified as stable. Flashback was identified by a rapid increase in temperature in any thermocouples below the YZA/SiC interface (thermocouples A-D at locations 6-8).

The pressure drop was determined from the measured value of static pressure upstream and downstream of the PMB, using a differential pressure transducer. The upstream tap is shown in Fig. 4.2 as AP501 in the upstream reactant mixture of the PMB, and the downstream tap is indicated as AP601. The pressure drop of the PMB was measured directly with a differential pressure transducer, PDT501 model 3100D-2-FM-1-1, with range of (0.15 to 7.5 kPa) and accuracy  $\pm 0.75\%$  of full scale. Differences in hydrostatic head and velocity head between the two wall taps were negligible and omitted in the pressure drop result.

Liquid n-heptane was chosen as a neat fuel to alleviate concerns associated with the coking and separation of multi-component fuel into constituents with different vapor pressure, density and heating value. Since gaseous methane fuel was used in the earlier study at atmospheric conditions (see Chapter 3), methane at 8 bar was also tested in this study for performance comparison.

The test series in this study are summarized in Table 4.2, and the burner performance results for each are discussed in the following section.

Test Series	Fuel	Operating Pressure (bar)	Mass Flux (kg/(m <sup>2</sup> s))	Equivalence Ratio	Preheat Temperature
1	n-Heptane	2	0.71–1.68	0.44–0.61	517–526K
2	n-Heptane	8	0.86–3.26	0.39–0.55	498–527K
3	n-Heptane	20	1.37–3.24	0.39–0.49	519–541K
4	Methane	8	0.68–3.38	0.39–0.55	483–524K

Table 4.2: Summary of the test series operating fuel and pressure, as well as the range of tested operating conditions.

## 4.4 Results and discussion

### 4.4.1 Flame stability and temperature profiles

For the operating conditions specified in Table 4.2, the corresponding flame stability and temperature profiles were measured. The regions of burner stability are shown in Fig. 4.5 for n-heptane and Fig. 4.6 comparing n-heptane and methane at 8 bar. Solid lines in the stability maps indicate either flashback or blow-off boundaries. All other edges of the stability map are imposed limitations of the mass flow meter and thermocouples. More specifically, vertical boundaries without a solid line were imposed by the limits of the mass flow meters for the air and fuel, and horizontal boundaries (i.e. the upper limit of tested equivalence ratios), were imposed by the measured temperatures in the PMB. To protect the PMB material and the thermocouples, the upper temperature limit for stable operation was set at 1580 K, and thus operating conditions that exceeded this temperature were not tested. In all tests, flashback events occurred more rapidly than liftoff events. Once the flame flashed back in one quadrant, it soon propagated to the other quadrants in the YZA element and eventually to the base of the PMB. In Figs. 4.5a and 4.5b, the size of the symbols represent the CO emissions corresponding to that operating condition, ranging between 0–17 ppm. At the lowest stable equivalence ratios and mass flux rates, the flame was stationary but began to quench, as observed by the elevated formation of CO. This limit differs from flashback, where the flame migrated upstream with increased temperature inside the YZA porous media

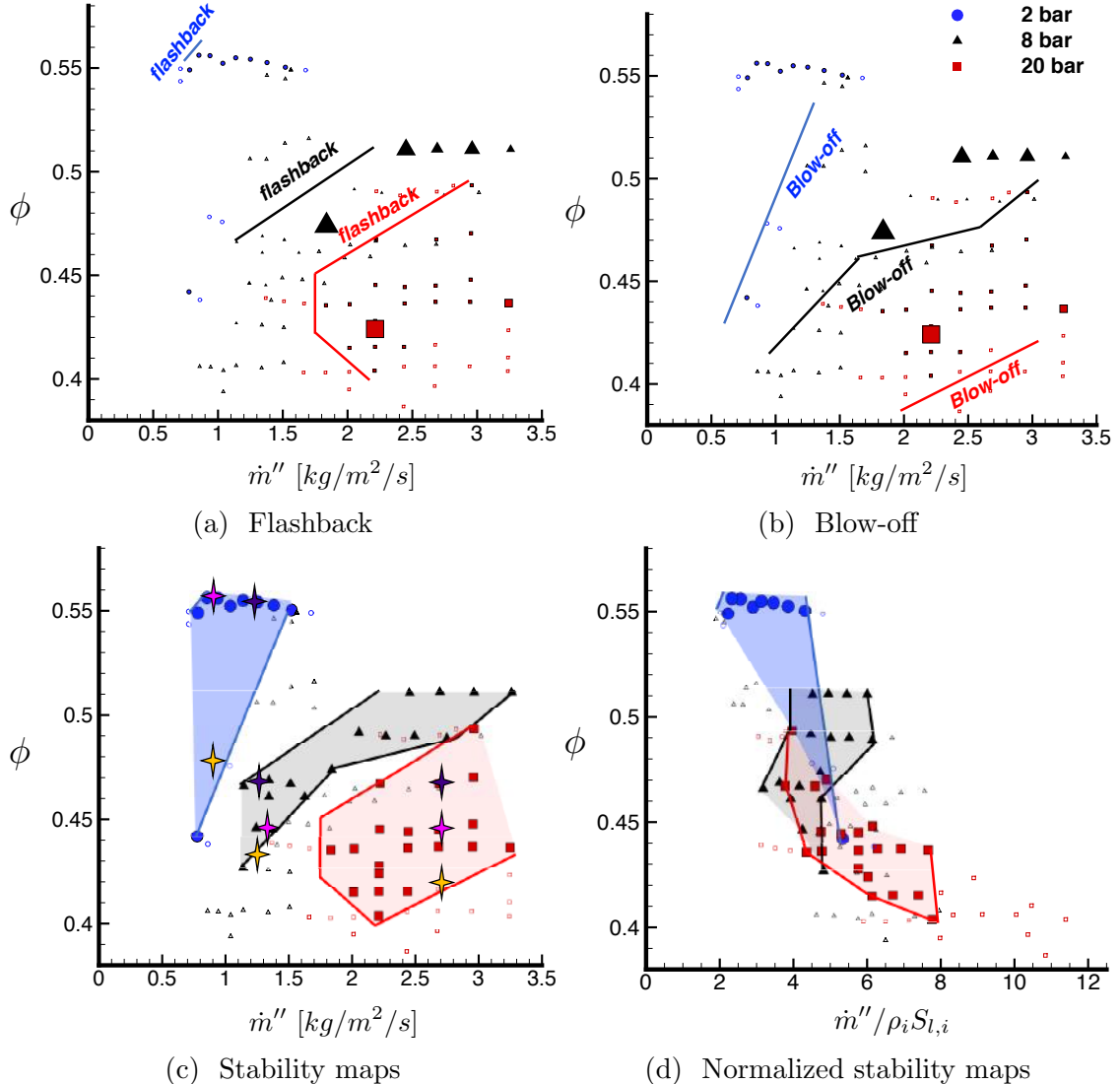


Figure 4.5: Stability maps for liquid C<sub>7</sub>H<sub>16</sub> PMB: (a-b) flashback and blow-off boundaries of the stability regimes, with the size of the symbols representing CO emissions between 0–17 ppm, (c) flame stability maps, solid lines imply limit of stability, other boundaries determined by limits of the mass flow controllers and thermocouples, (d) stability maps, normalized by the local burning rate. Open symbols denote tested yet unstable conditions. The data corresponding to this figure can be found in Table A.7 in Appendix A

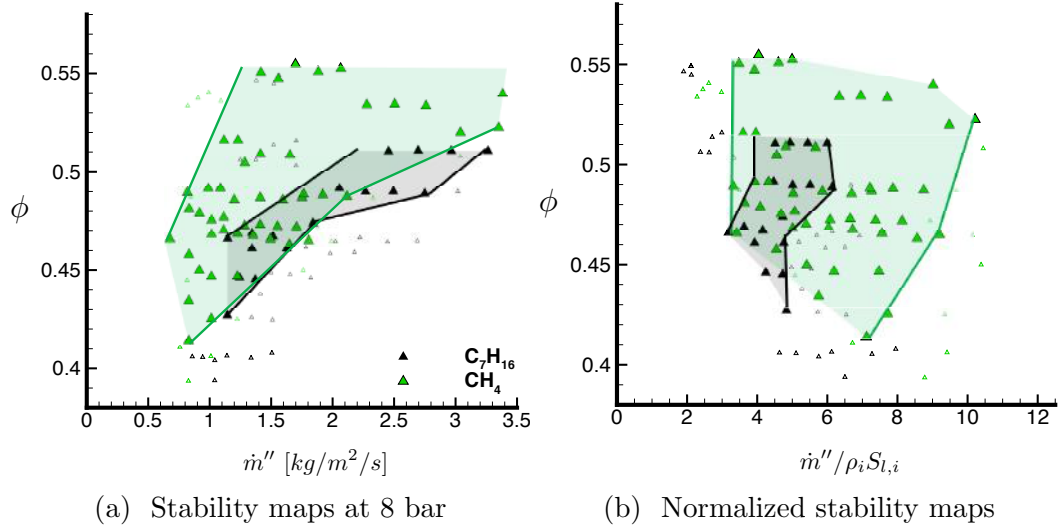


Figure 4.6: (a) Comparison of flame stability for  $C_7H_{16}$  and  $CH_4$  at 8 bar: a) stability maps, (b) stability maps normalized by the laminar burning rate. Open symbols denote tested yet unstable conditions. The data corresponding to this figure can be found in Table A.7 in Appendix A

With increasing pressure, the flashback boundary and higher mass flux rates moves to leaner conditions, which is predicted by the aforementioned modified Péclet number analysis (Eq. (4.1)).  $Pe_{S_l}$ , or the ratio of heat release to heat removal, increases with increasing pressure, which increases the preheat temperature thereby increasing the propensity of flashback. The computational results in Section 4.2 verify this trend, showing that the preheat temperatures increase with pressure (see Fig. 4.1b). A similar increase in flashback propensity was found for methane-fuel PMB operation at pressures up to 11 bar by Noordally et al. [Noordally et al. \(2004\)](#).

The flame stability maps in Fig. 4.5d and Fig. 4.6b are normalized by the laminar burning flux,  $f = \rho_i S_{l,i}$ , using local reference quantities as a function of burner inlet temperature, pressure, and equivalence ratio. The effect of the porous media on the combustion performance and flame stabilization is highlighted by this normalization. Fig. 4.5d and Fig. 4.6b show an increase in the normalized mass flux by up to six to ten times for n-heptane and methane, respectively. After normalization, the results show a significantly higher blow-off boundary in the stability regime for methane than

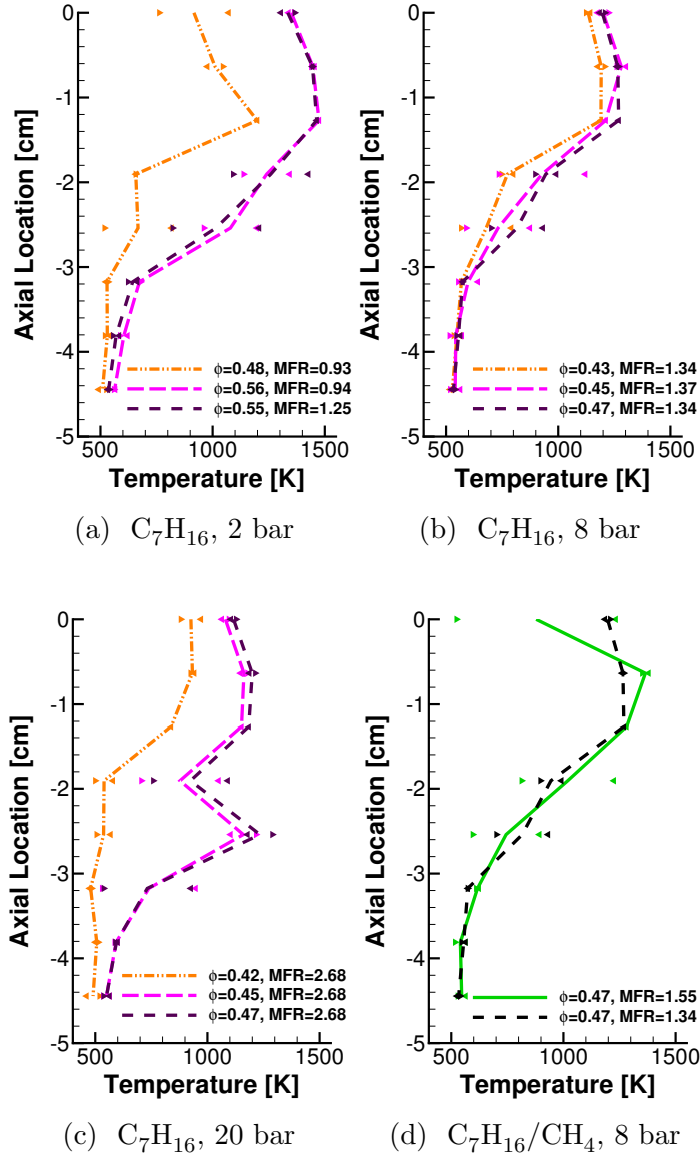


Figure 4.7: Temperature profiles at various mass flux rates (MFR) and equivalence ratios,  $\phi$ , of  $\text{C}_7\text{H}_{16}$  flames at a) 2 bar, b) 8 bar, and c) 20 bar marked in Fig. 4.5c, where the orange data correspond to near blow-off conditions and the other data correspond to stable operating conditions. (d) Comparison of temperature profiles of  $\text{C}_7\text{H}_{16}$  (black) and  $\text{CH}_4$  (green) at 8 bar at similar mass flux rate and  $\phi = 0.47$ . Symbols  $\blacktriangleright$  correspond to thermocouples A and B, and symbols  $\blacktriangleleft$  to thermocouples C and D, and the lines correspond to the average temperature at each location. The data corresponding to this figure can be found in Table A.6 in Appendix A

n-heptane, as indicated by the solid lines in Fig. 4.6b.

Temperature profiles of n-heptane flames at 2 bar, 8 bar, and 20 bar marked in Fig. 4.5c are shown in Fig. 4.7. Thermocouple temperature measurements at each axial location illustrate significant tilting of the flame for certain conditions. Increasing equivalence ratio results in increasing peak temperatures. Furthermore, similar to the computational temperature profiles shown in Section 4.2, the experimental temperature profiles become more flattened as the pressure increases, exhibiting higher preheat temperatures.

Figure 4.7d compares the flame profiles of comparable stable operating conditions for n-heptane and methane at 8 bar. Although a similar average temperature profile was measured, the methane flame is significantly more inhomogeneous in the azimuthal direction and lift-off at thermocouple A-1 is observed. The flame heterogeneities and tilting are further illustrated in Fig. 4.8 for the leanest conditions shown in Fig. 4.7. Flame tilting was also observed in a previous study of gaseous methane at atmospheric pressure, with the same PMB matrix composition ([Sobhani et al. 2017](#)). The study by [Hsu et al. \(1993\)](#) attributed the flame tilting to the formation of fissures that disturb the otherwise uniform flow distribution as well as the local thermophysical properties of the solid matrix. Such fissures were indeed observed in the porous matrix post-combustion in XCT scans (see Section 4.5). Furthermore, computational studies of filtration gas combustion identify flame inclination as one of two key flame-front instabilities in flame propagation in packed-bed porous media ([Minaev et al. 1994](#); [Dobrego et al. 2001](#); [Zhang et al. 2013](#)).

#### 4.4.2 Pressure drop

The pressure drop for both heptane and methane flames increase with increasing mass flux rate, according to the Darcy-Forchheimer model, described in Eq. (2.4). To isolate the effect of the operating pressure, the total pressure drop across the porous matrix can be expressed by integrating Eq. (2.4) along the axial direction and

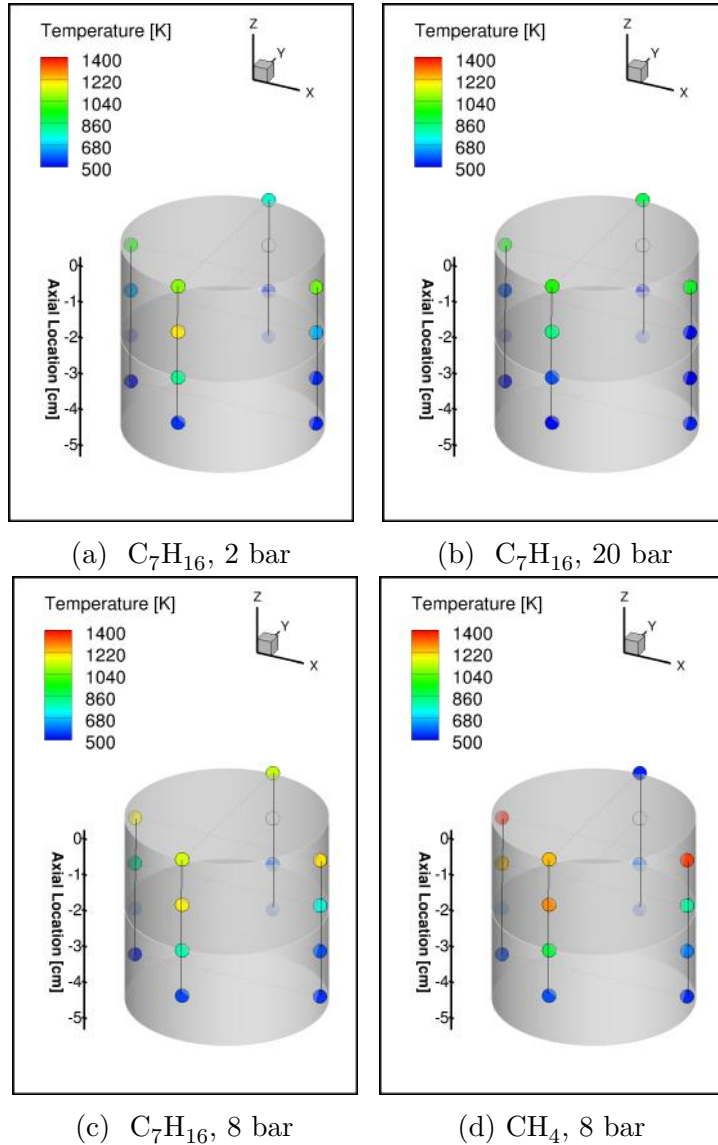


Figure 4.8: 3D temperature profile rendering corresponding to the leanest conditions in Fig. 4.7, (a)  $\phi = 0.48, 0.93 \frac{\text{kg}}{\text{m}^2\text{s}}$ , (b)  $\phi = 0.43, 1.34 \text{ kg}/(\text{m}^2\text{s})$ , (c)  $\phi = 0.42, 2.68 \text{ kg}/(\text{m}^2\text{s})$ , (d)  $\phi = 0.47, 1.55 \text{ kg}/(\text{m}^2\text{s})$ .

substituting the ideal gas law to relate pressure and density:

$$\Delta P = - \int_0^x \frac{RT}{P_o} \left[ \frac{\mu}{K_1} \frac{\dot{m}''}{\epsilon} + \frac{1}{K_2} \left( \frac{\dot{m}''}{\epsilon} \right)^2 \right] dx . \quad (4.3)$$

Thus, for an equivalent temperature profile, the pressure drop is estimated to be lower at higher operating pressures. The measured pressure drop is shown in Fig. 4.9a. By multiplying the measured pressure drop by the operating pressure, the results begin to collapse as shown in Fig. 4.9b. The results for higher pressures still remain slightly lower, due to the lower flame temperatures at these conditions.

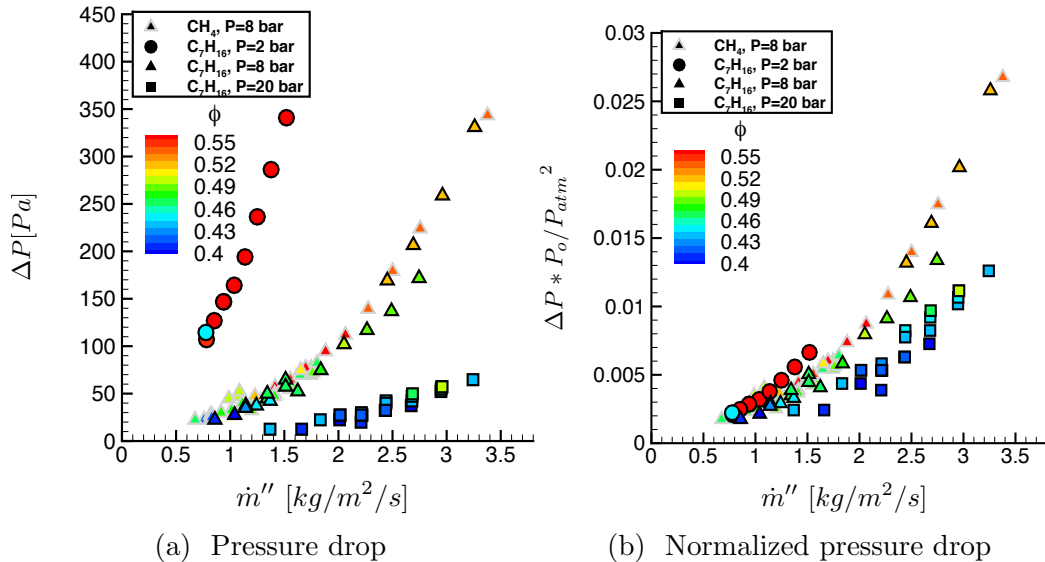


Figure 4.9: Measurements of pressure drop at stable operating conditions, where symbols correspond to operating pressure at 2 bar (●), 8 bar (▲) and 20 bar (■). The data corresponding to this figure can be found in Table A.7 in Appendix A

#### 4.4.3 Emissions

Emissions of  $\text{NO}_x$  and CO, corrected to 3% O<sub>2</sub>, are shown in Fig. 4.10 for both fuels at elevated pressures and stable operating conditions. Since all temperatures are below 1800 K, thermal NO production is insignificant, and the prompt NO pathway

is dominant (Miller and Bowman 1989). The  $\text{NO}_x$  emissions decrease at higher pressures, since the stability regime shifted to leaner conditions with increasing pressure. For stable operating conditions,  $\text{NO}_x$  emissions increase with increasing mass flux rate and equivalence ratio due to higher local temperatures in the burner, as indicated by thermocouple measurements. Near the minimum stability limit (i.e. lower equivalence ratio and mass flux), the CO emissions increase for both fuels since the flame is starting to quench. Similarly, near the blow-off and flashback boundaries, the local temperature begins to decrease and incomplete combustion results in higher CO emissions. (Kaplan and Hall 1995) performed experimental tests at atmospheric pressure where the liquid n-heptane fuel was sprayed directly onto a porous foam upstream of the main PMB, and reported similar CO and  $\text{NO}_x$  emissions as those of the current study at 2 bar (i.e., 3–7 ppm CO and 15–20 ppm  $\text{NO}_x$ ). For all stable operating conditions,  $\text{NO}_x$  measurements were below 25 ppm and mostly complete CO combustion was observed, with a maximum of 17 ppm.

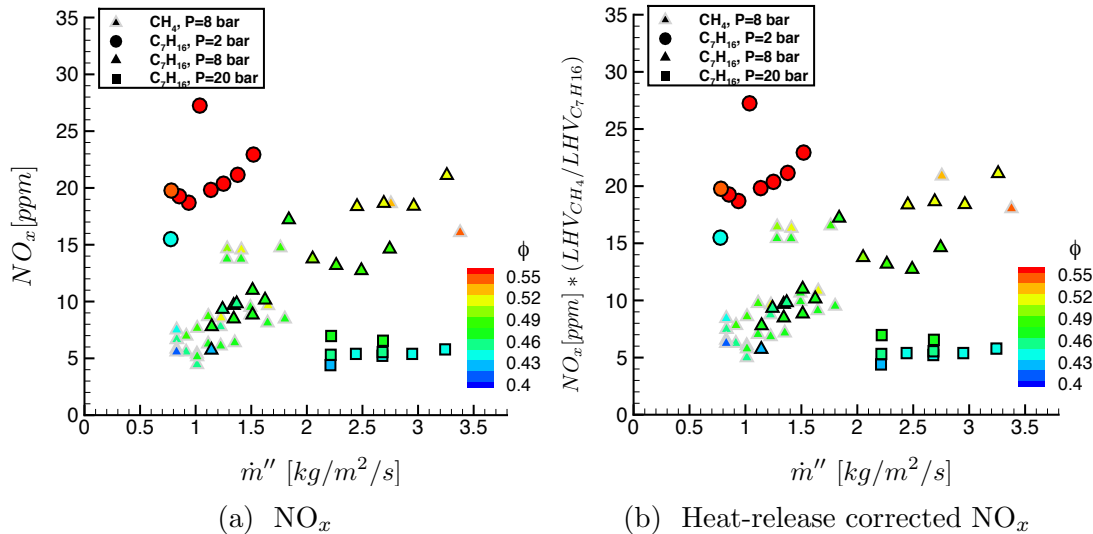


Figure 4.10: Emissions measurements at stable operating conditions for both methane and heptane fuels, at 2 bar (●), 8 bar (▲) and 20 bar (■). The data corresponding to this figure can be found in Table A.7 in Appendix A

## 4.5 X-ray Computed Tomography analysis

The PMB experiments were performed over four days, during which the burner underwent dozens of on-and-off cycles and a total of over 22 hours of operation. To examine the structural integrity of the porous matrix over the course of the combustion tests, the 3 PPI SiC sample was analyzed using a ZEISS XRADIA 520 VERSA X-ray Microscope for XCT. As the resolution capability of the diagnostic decreases with increasing field-of-view, the whole domain was first scanned at a resolution of  $89.8 \mu\text{m}$  to identify large-scale structural defects. Subsequently, a high-resolution scan of a strut was performed to identify small-scale cracks and surface properties. The acquisition parameters of the two scans, performed with projections over  $360^\circ$ , are summarized in Table 4.3.

Scan	Field of View	Resolution	Voltage	Current
1	Full domain	$89.6 \mu\text{m}$	110 kVp	91 mA
2	1.8mm	$1.88 \mu\text{m}$	60 kVp	83 mA

Table 4.3: Acquisition parameters of the XCT scans.

Automatic 3D segmentation and isosurface rendering were performed using the Avizo software to visualize the structure, as shown in Figs. 4.11 and 4.12. The pre- and post-combustion scans of the full domain were nearly identical, and showed no apparent signs of large-scale degradation. The isosurface of the matrix post-combustion is shown in Fig. 4.11. However, the higher resolution scan revealed fissures ( $\sim 20 \mu\text{m}$  wide) in the struts of the matrix structure. Thus, high-resolution methods are required to fully examine the material degradation of the ceramic matrix foams. However, the matrix proved to be durable in withstanding the over 22 hours of operation, thermal stresses due to on-and-off cycling, and high pressure conditions. In addition to the fissures, the high-resolution scans reveal an increase in the solid surface roughness after combustion. SiC oxidizes at high temperatures, leading to oxide bubble formation and solid  $\text{SiO}_2$  deposition on the matrix structure Jacobson (1993); Gianella et al. (2012); Aronovici et al. (2015). Aronovici et al. Aronovici et al. (2015) found that the formation of an oxide layer on SiC lattice drastically reduces the effective thermal conductivity, while changes in pressure drop are insignificant. Although the

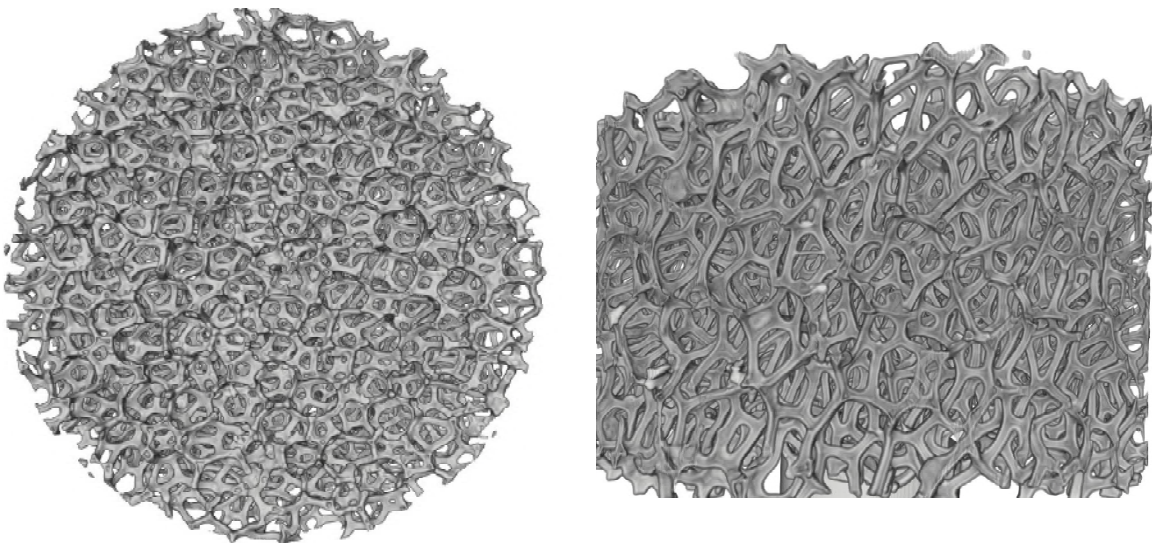


Figure 4.11: Side and top view of the XCT isosurface of the full SiC porous foam matrix (5.08cm diameter and 2.54 cm height) in the downstream zone of the burner, post-combustion, after 22 hours of operation. Scan acquisition parameters correspond to Scan 1 in Table 4.3.

XCT scans indicate the potential of oxide layer deposition after high pressure PMB operation, further analysis of the material composition is needed to identify the cause of the apparent surface transformation and its effects on the burner performance.

## 4.6 Summary

In this chapter, the performance of a PMB that was operated with liquid fuel at high-pressure conditions was examined. Combustion stability regimes, temperature, pressure drop, CO and  $\text{NO}_x$  emissions were measured and XCT analysis was performed to examine the structural integrity of the porous matrix during high-pressure combustion. Experiments were conducted in NASA's high-pressure facility SE-5 at 2, 8, and 20 bar absolute pressure using n-heptane fuel with preheat temperatures of around 500 K. For performance comparisons, the burner was also tested with methane at 8 bar. After normalization with the laminar burning rate, the results showed a significantly larger stability regime for methane than n-heptane. For all tests, the

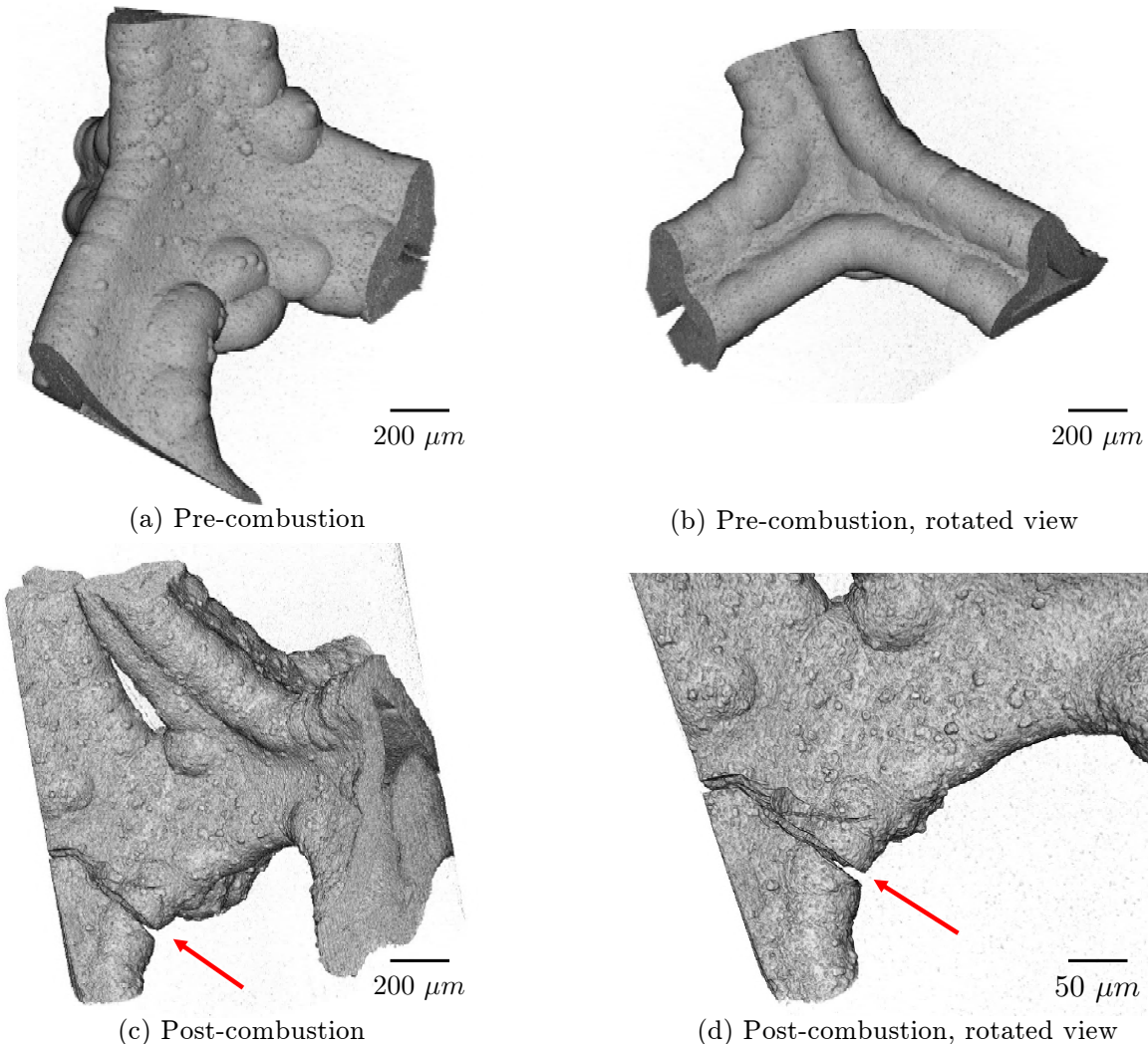


Figure 4.12: XCT isosurface of a strut in 1.8 mm field of view of the SiC porous foam matrix in the downstream zone of the burner, pre- and post-combustion, where the arrow indicates the location of the crack. XCT-acquisition parameters correspond to Scan 2 in Table 4.3.

burning velocity in the PMB was measured up to ten times higher than the laminar flame speed. Trends in flame flashback were found to be well predicted by the modified Péclet number, illustrating a higher mass flux flashback boundary with increasing pressure. These experimental investigations were complemented by numerical simulations to examine effects of the pressure and liquid fuel on the flame structure. These simulations confirmed the increase in preheat-zone temperatures and propensity for flashback with increasing pressure. The pressure drop was shown to decrease with increasing pressure, although independent of fuel. NO<sub>x</sub> measurements were below 25 ppm for all stable operating conditions, for which complete oxidation of CO was observed. At 20 bar conditions, stable operation at very low values of equivalence ratio were found, with corresponding values of NO<sub>x</sub> below 5 ppm. Additionally, this work demonstrated the utility of applying lab-scale XCT diagnostics for investigating the material and structural processes in porous foams. The XCT analysis revealed small-scale fissures, but no large-scale defects were observed in the SiC porous matrix after extensive high-pressure testing.

Although PMBs have been previously identified as an advanced combustion technology capable of reducing emissions and increasing system efficiency, most of the existing literature on PMBs are limited to gaseous fuels operated at atmospheric pressure conditions. The current study extends to pre-vaporized liquid fuels and elevated pressures to demonstrate the viability of porous media combustion for application to gas-turbine engines and presents quantitative trends at engine-relevant conditions.

# Chapter 5

## Modulation of Heat Transfer for Extended Flame Stabilization in Porous Media Burners Via Topology Gradation \*

### 5.1 Motivation

The design proposed in this chapter is based on a topology gradation of the porous matrix, which addresses the aforementioned challenges in PMB design: reliable operation of premixed flames, enhanced heat recirculation without flashback, and extended blow-off limit. Pore topology is commonly defined by pore diameter, cell diameter, porosity, and other parameters outlined in [Mullens et al. \(2006\)](#). The structure of porous foams consists of rounded polyhedra (cell diameter) connected by openings or windows (pore diameter). The topology of the porous material directly impacts the local heat transfer, and thereby the flame behavior. The impact of porosity and pore diameter on the properties of the flame is examined theoretically in Section 5.2 by non-dimensionalizing the volume-averaged governing equations and isolating the

---

\*This chapter contains previously published work ([Sobhani et al. 2019b](#)), adapted here with only minor modifications. Danyal Mohaddes contributed to the experimentation presented.

constitutive relations that are strongly dependent on the pore topology. The newly proposed design, referred to as a “graded” PMB, is studied numerically using a 1D volume-averaged model and experimentally using a series of SiC porous foams instrumented to measure the temperature profiles and pressure drop. The experimental investigation is presented in Section 5.3, comparing results to those of a “step” PMB to illustrate the performance advantages of the graded design, with power-dynamic ratios near 50:1 and less than 5.4% pressure drop. This chapter closes by offering conclusions in Section 5.4.

## 5.2 Computational investigation

### 5.2.1 Theoretical analysis

The equations governing the combustion in porous media are derived by volume-averaging of the transport equations for a chemically reacting gaseous system (Eq. (2.1)). The equations, assumptions, and computational framework are described in Chapter 2. In the current model formulation, the approximation of the radiative heat extinction coefficient is based on a geometric optics model, previously validated by Hsu and Howell (1992), where  $\kappa = 3(1 - \epsilon)/d$ . Patel and Talukdar (2016) determined the radiative properties of a ceramic foam by solving the radiative transfer equations in a 3D cubic unit cell, reporting a positive correlation between pore density and extinction coefficient. Assuming that the pore diameter decreases with increasing pore density, this is consistent with the geometric optics model that predicts an increase in extinction coefficient with decreasing pore diameter. Scattering albedo, however, was found to be unaffected by pore density (Patel and Talukdar 2016). Therefore the extinction coefficient and optical depth are increased with decreasing pore diameter. As such, if the porous media is sufficiently opaque, radiation becomes ineffective at recirculating heat.

After non-dimensionalization of Eq. (2.1c) with respect to reference quantities, the ratio of the convective transport to the interphase heat exchange terms in the gas-phase temperature equation results in the Stanton number, defined in Eq. (1.1).

Depending on its sign, the term  $(T_g - T_s)$  in Eq. (2.1c) can quantify a source or sink. Specifically, upstream of the flame, the solid, which is heated by solid-solid radiation and conduction, transfers heat to the incoming cold reactants (i.e. source term), whereas the hot combustion products transfer heat to the solid downstream of the flame (i.e. sink term). To model this heat exchange, an empirical correlation for the Nusselt number in ceramic foams is used:  $\text{Nu} = C\text{Re}^m\text{Pr}^n$ , where the coefficients  $C$ ,  $m$ ,  $n$  equal 3.7, 0.38, and 0.25, respectively (Bedoya et al. 2015). The Reynolds and Prandtl numbers are defined as:  $\text{Re} = \rho_g u_D d / \mu_g$ ,  $\text{Pr} = C_{p,g}\mu_g / \lambda_g$ , respectively.

Effects of pore diameter,  $d$ , and mass flux rate,  $\dot{m}''$ , on the Stanton number are illustrated in Fig. 5.1, where the values for the thermal properties correspond to burnt gases. Figure 5.1 illustrates the decrease of interphase heat exchange with increasing mass flux ( $\text{St} \propto (\dot{m}''d)^{m-1}$ ), which reduces preheating and eventually results in flame blow-off. As highlighted by the empirical correlations discussed, closure models for the 1D volume-averaged equations are parametrized by two main topological features, namely pore diameter and porosity, with the assumption that other features such as pore density and cell diameter can be deduced through a deterministic mapping.

Burner	Two-zone (Step)	Continuous (Graded)
1	$\epsilon = (\epsilon_1 + \epsilon_2)/2$	$\epsilon = (\epsilon_1 + \epsilon_2)/2$
	$d(x) = d_1 + \Delta d \mathcal{H}(x - x_I)$	$d(x) = d_1 + \Delta d(x/L)$
2	$\epsilon(x) = \epsilon_1 + \Delta \epsilon \mathcal{H}(x - x_I)$	$\epsilon(x) = \epsilon_1 + \Delta \epsilon(x/L)$
	$d(x) = d_1 + \Delta d \mathcal{H}(x - x_I)$	$d(x) = d_1 + \Delta d(x/L)$

Table 5.1: Geometry of the burners, where  $x$  is the axial position,  $L$  is the burner length,  $x_I$  is the length of the upstream section,  $\epsilon$  is porosity, and  $d$  is pore diameter; subscripts 1 and 2 denote values at the inlet and outlet, respectively,  $\Delta d = d_2 - d_1$ ,  $\Delta \epsilon = \epsilon_2 - \epsilon_1$ ,  $\mathcal{H}(\xi)$  denotes the Heaviside function.

Recognizing that the heat transfer between the solid and gas, quantified using the Stanton number, as well as the radiative heat transfer in the solid are primarily dependent on the local pore topology, a comparative study of flame stability and pressure drop between conventional “step” PMBs and those with graded matrix topologies was conducted. The porous matrix in “graded” PMBs can be designed to accommodate different heat outputs over a wider range of operating conditions without resorting to a flame quenching approach. In this study, gradation of the porous matrix was

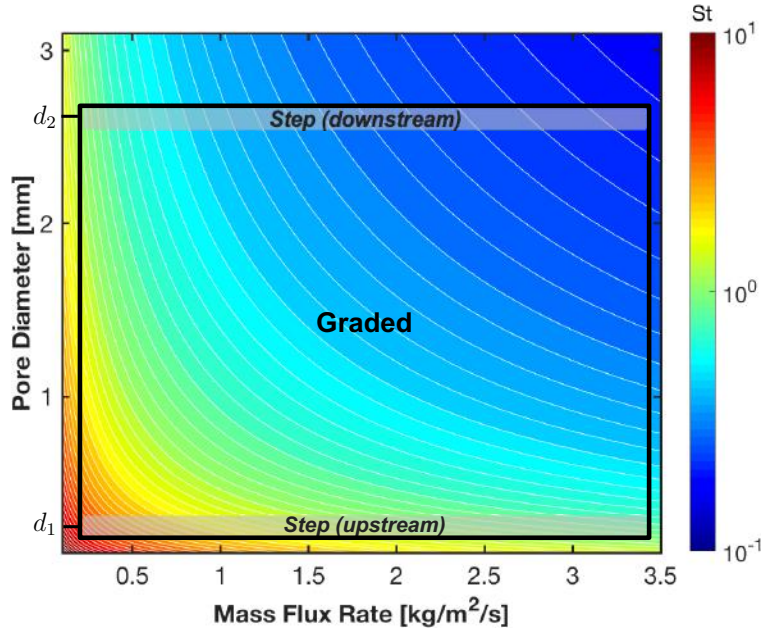


Figure 5.1: Contour map of the local Stanton number as a function of pore diameter,  $d$ , and mass flux rate,  $\dot{m}''$ . Ranges of Stanton numbers accessed in the “step” burners versus the “graded” burners are illustrated.

achieved by changing either the local pore diameter, porosity, or both simultaneously. Two of the configurations examined for “step” and “graded” PMBs are shown in Table 5.1. Prompted by the analysis of the governing equations and constitutive relations for heat exchange and thermal radiation, the following numerical and experimental studies demonstrate and experimentally validate the impact of a graded porous matrix on the salient features of a PMB.

### 5.2.2 Computational method and setup

Numerical simulations were performed using the Cantera (Goodwin 1998) 1D reacting flow solver, which was adapted to account for the coupling between the gas and solid phases. More details on the model assumptions and the computational method can be found in Chapter 2. Detailed reaction chemistry for methane/air was modeled using the GRI 2.11-mechanism (C. T. Bowman et al. 1995), which includes nitrogen chemistry.

To facilitate comparisons, the length, material, and pore densities modeled correspond to those of the experimental study, described in Section 5.3. The total length of all burners considered is  $L = 7.62$  cm, and the length of the upstream section, serving as a flashback arrestor for the interface-stabilized burner is  $x_I = L/2$ . A “graded” burner of the same total length was constructed with the same porosity and pore-diameter limits, but with either a linearly varying or a constant profile (see Table 5.1).

The effective thermal conductivity,  $\lambda_{s,\text{eff}}$ , in the porous solid is determined by the material microstructure and the conductivity of its constituents using PuMA ([Ferguson et al. 2018](#)). For this, a  $25\ \mu\text{m}$  resolution tomographic reconstruction of the 10 PPI SiC foam used in the experimental investigation is imported to PuMA. The steady state heat conduction equation is then solved using a finite difference method with a prescribed temperature differential in the simulation direction and periodic boundary conditions in the side directions. This process is repeated for the all three directions. An effective thermal conductivity is found to be isotropic and equal to  $8.7\ \text{W}/(\text{mK})$ , which is approximated as a constant, thereby neglecting the weak dependence on the local topology for the conditions considered in the present work ([Hsu and Howell 1992](#)). All simulations and experiments in the current work were done using the same material (i.e. SiC).

Using this simulation technique, a parametric study exploring inlet mass flux rate and equivalence ratio was carried out to compare the stability range, pressure drop and emissions of the newly proposed “graded” burner against the conventional “step” burner. Starting with a stable operating point, simulations were performed by incrementally increasing or reducing the mass flux rate until flame blow-off or flashback, respectively. Predicted mass flux rates above the validity of the closure models used for interphase heat transfer were discarded. Results from this analysis are discussed next.

### 5.2.3 Parametric analysis

Flame stability, pressure drop, and  $\text{NO}_x$  emissions of “step” and “graded” PMBs were investigated computationally. For burner 1, both designs had a constant porosity  $\epsilon = 0.8$  and increasing nominal pore diameters (i.e.  $d = 1/\text{PPI}$ ),  $d_1 = 0.39$  mm and  $d_2 = 2.54$  mm, corresponding to 65 PPI and 10 PPI foams, respectively. For burner 2, the pore diameter profile was the same as burner 1, but the porosity was graded from  $\epsilon_1 = 0.75$  to  $\epsilon_2 = 0.85$ . The stability envelopes for both burners are shown in Fig. 5.2 for equivalence ratios 0.55 to 0.65 since at higher equivalence ratios, the predicted mass flux rates were outside of the valid range of the closure models used for interphase heat transfer. Trends in flame stability at these lean conditions confirm the predictions of the theoretical analysis and motivated further experimental investigations.

Figures 5.2a,b illustrate the stability envelopes of burner 1, corresponding to “step” and “graded” PMBs, shown with isocontours of pressure drop, mass flux rate associated with laminar flame speed indicated by  $S_L$ , together with measurements at the experimentally determined maximum mass flux rates (further described in Section 5.3). As predicted by the analysis of the optical depth and interphase heat exchange in the governing equations, a “graded” PMB expands the range of stable operating conditions compared to that of a “step” PMB. Burner 1 reached approximately 75% higher blow-off mass flux rates than the “step” PMB, while maintaining similar  $\text{NO}_x$  emissions (not shown). Figures 5.2c,d illustrate the stability envelopes of burner 2. The pressure drop is generally lower for this burner, although the increase in flame stability is less pronounced. In the burners with a step profile in pore topology, the flame primarily stabilizes slightly downstream of the interface, where the pore diameter is larger. However, in the “graded” burner, the flame is not anchored to any specific location but rather is dynamically stabilized, resulting in the following practical consequences. First, this feature is relevant to the pressure drop, which is inversely proportional to the pore diameter and directly proportional to the viscosity (Philipse and Schram 1991). Viscosity at the flame is significantly increased, but its effect on pressure drop is mitigated if the flame is stabilized within larger pores, as in the “step” burner. Therefore, the “step” PMB is predicted to have lower pressure

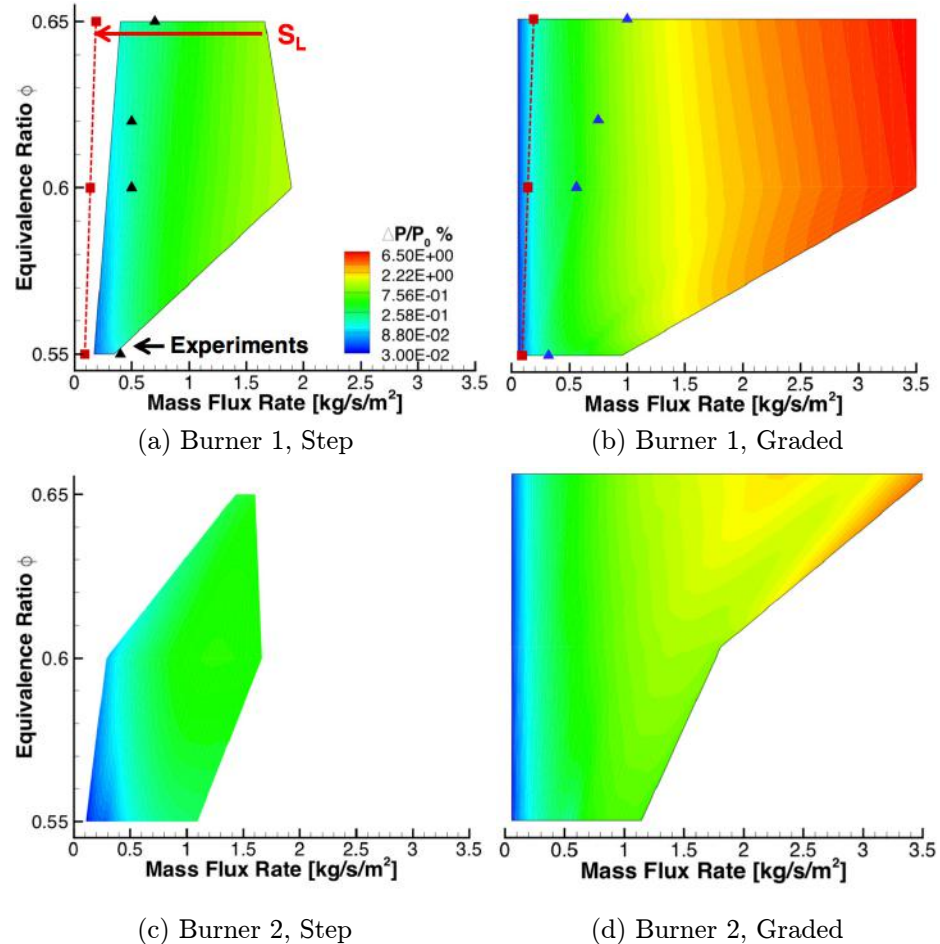


Figure 5.2: Computational stability maps of (a,c) “step” and (b,d) “graded” burners 1 and 2, respectively, as well as mass flux rate associated with laminar flame speed indicated by  $S_L$  (dashed line) and experimental measurements (symbols).

drop. Second, the interface- versus continuous-flame stabilization affects the axial Stanton number profile and consequently the heat transfer properties, as illustrated in Fig. 5.3(b).

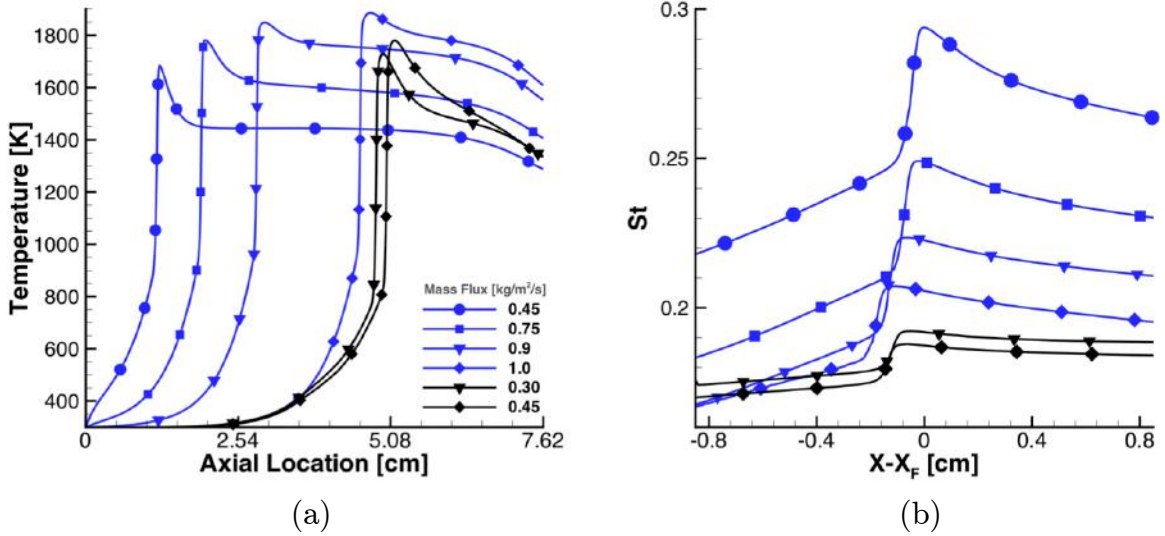


Figure 5.3: (a) Gas temperature profiles at  $\phi = 0.55$  corresponding to stability maps shown in Fig. 5.2a,b and (b) profiles centered at flame peak temperature location  $X_F$  for local St, for graded (blue) and step (black) profiles.

Temperature profiles, which confirm the excess enthalpy behavior in PMBs, are shown in Fig. 5.3a. The continuous-flame stabilization of the “graded” PMB is compared to the anchored flames of the “step” PMB, corresponding to the stability map of burner 1 at  $\phi = 0.55$  (see Fig. 5.2). In Fig. 5.3b, the coordinate system has been centered at the flame location to examine trends in the local Stanton number. At higher mass flux rates, the flame in the “graded” burner stabilizes further upstream, where the local Stanton number near the flame is higher, as compared to the “step” burner. The St values in Fig. 5.3b decrease with increasing mass flux, as illustrated in Fig. 5.1, although values for local St in the “graded” burner match those of the “step” burner at two to three times higher mass flux rates. The “graded” burner increases the heat exchange into the solid downstream of the flame, which, together with the smaller optical depth upstream, enhance interphase heat transfer and radiation feedback. This results in further preheating of the incoming reactants, thus

delaying blow-off. The “graded” burner 1 (Fig. 5.2b) results in the maximum blow-off mass flux rate and reduced propensity for flashback, therefore this burner design was chosen for the experimental investigation.

## 5.3 Experimental investigation

### 5.3.1 Experimental setup and procedure

An experiment was designed to test the computational predictions and to examine the stability and pressure drop characteristics of the “graded” burner in comparison to the step design. All experiments were performed using methane/air mixture at atmospheric pressure. Flow rates of reactants were measured and controlled using Alicat Scientific mass flow controllers. Compressed air and methane were mixed at a tee-junction approximately 200 tube diameters upstream of the burner to achieve a homogeneous mixture prior to entry into the burner. The gauge pressure was measured immediately upstream of the burner using an Omega PX309 pressure transducer. A schematic of the experimental setup is illustrated in Fig. 5.4 and the burner in operation is shown in Fig. 5.5.

The burner consisted of stacked ceramic foams that were wrapped in a layer of compressible ceramic insulation (Unifrax Fiberfrax 550-Grade Ceramic Fiber Paper) and housed in a quartz tube. Temperature was measured using K-type mineral-insulated thermocouples with standard limits (Watlow) placed between the porous media and the ceramic insulation. As discussed in Section 4.3, the thermocouple measurement approximates the local solid temperature and was used in the experiments primarily to identify the flame location.

Hardware interfacing and data acquisition were performed using a National Instruments Data Acquisition system (NI-cDAQ 9188). All measured variables were logged automatically at 10Hz by a laboratory computer, and all controlled variables were specified using a LabVIEW interface. Maximum error in mass flux rate was  $< 1\%$  and the error in equivalence ratio was typically  $< 3\%$ , not exceeding 12% at the extinction limit. Thermocouple and pressure transducer errors were reported by

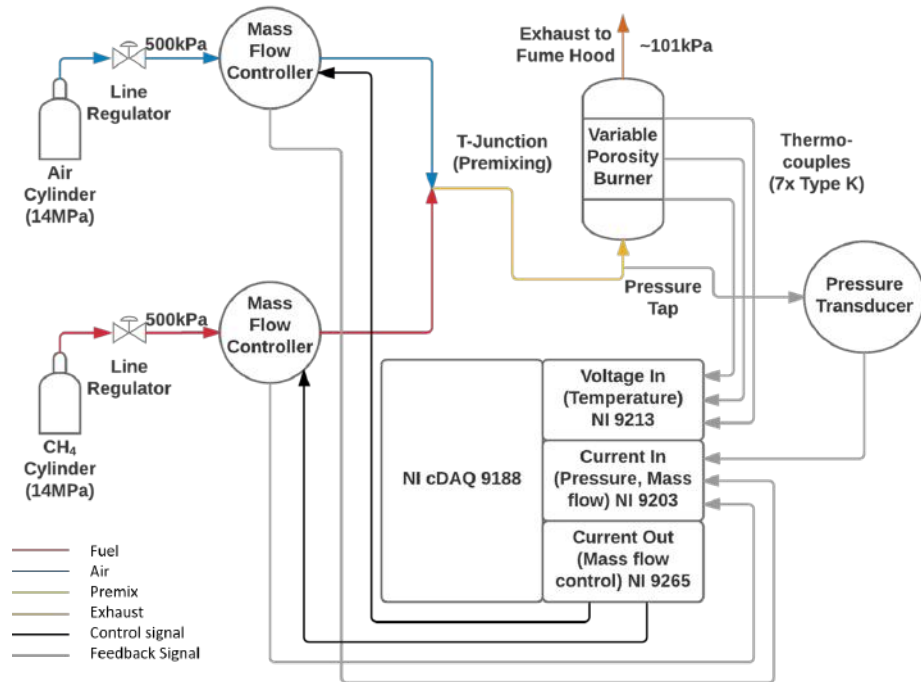


Figure 5.4: P&ID illustrating the experimental setup and instrumentation.

the manufacturer as  $\pm 0.75\%$  and  $\pm 0.25\%$  of the measured value, respectively. The system was ignited directly downstream of the porous media while supplied with lean premixed methane/air at a condition corresponding to the laminar flame speed. The first thermocouple was placed 1.3 cm upstream of the porous media to monitor for flashback, but this phenomenon was not observed in the current study. Instead the flame eventually extinguished with decreasing mass flux rate. Six subsequent thermocouples were placed downstream at azimuthal locations varying by  $90^\circ$ . The locations of the thermocouples are shown by the symbols in Fig. 5.8.

Stable operation was defined as continuous operation with no changes in thermocouple measurements greater than 5 K over 5 minutes. After reaching steady state, the stability limits were determined by changing the equivalence ratio (at a constant mass flux) to the condition under consideration, and subsequently increasing (or decreasing) the mass flux (at a constant equivalence ratio) in increments of  $0.05 \text{ kg}/(\text{m}^2\text{s})$ . The blow-off limit was determined first by the occurrence of the maximum temperature measurement at the thermocouple furthest downstream, and subsequently by

the continual decrease in temperature measured by this thermocouple. In the “step” PMB, blow-off was also confirmed visually by observing the gradual lift-off of the flame from the interface followed by lift-off from the downstream end of the porous media.



Figure 5.5: Images of burner in operation, at steady state conditions (left) and near blow-off (right).

The SiC porous matrix was manufactured by LANIK. Ceramic porous materials are commonly manufactured based on pore density. To create an axially variable profile, the manufacturer used disks of polyurethane foams with increasing pore densities, each with a height of 1.27 cm and a diameter of 5.08 cm. Six disks, ranging from 65 to 10 PPI, were first dipped in a ceramic slurry, and while wet, glued in ascending order of pore density. Once dry, the disks were sintered together to create a continuous porous material with a height of 7.62 cm (see Fig. 5.6). The “step”

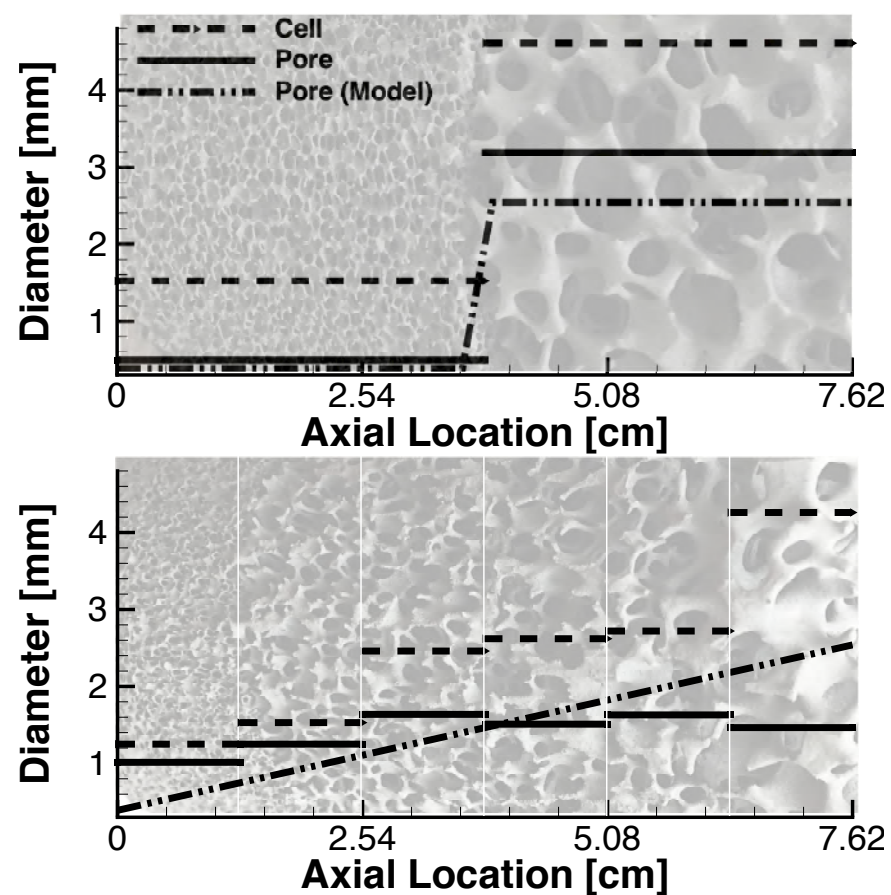


Figure 5.6: Average pore and cell diameters for “step” (top) and “graded” (bottom) PMBs, as well as nominal pore diameters used in the model.

burner was designed by stacking a 10 PPI and a 65 PPI SiC sample, each 3.81 cm in height, in the quartz tube. For both the “step” and “graded” burners, pore diameter increased in the direction of the flow but maintained a relatively constant porosity of approximately 75% and 78% in the “graded” and “step” PMB, respectively. The methodology for extracting pore topology profiles is discussed next.

### 5.3.2 Micro-XCT and analysis of the porous foam

All samples that were experimentally investigated in the present work were analyzed using Micro-XCT. Each sample was scanned using a GE eXplore CT 120 scanner with the following acquisition parameters: 25  $\mu\text{m}$  resolution, 80 kVp tube energy, 32 mA current and 1200 projections over 360°. The reconstructed gray-scale images were first smoothed using a 2D bilateral filter, and then binarized using a 3D constant threshold. The porosity was extracted along the axial location of the sample as the ratio of gas voxels over the total number of voxels, averaged over each cross-sectional slice. The pore and cell diameters were identified by using a 3D distance transform watershed algorithm followed by a 3D particle analyzer ([Legland et al. 2016](#); [Maire et al. 2007](#)). Measurements of mean pore and cell diameters along each cross-flow slice for the step and graded porous matrices are shown in Fig. 5.6.

### 5.3.3 Results and discussion

The experimental results for flame stability, temperature, and pressure drop are shown in Figs. 5.7-5.9. The flame stability maps, in Fig. 5.7, for both designs tested, qualitatively confirm a minimum 50% enhancement in flame stability, as found in the computational investigation. Thermocouple temperature measurements for both burners are shown in Fig. 5.8, and compared to solid temperatures predicted by the model discussed in Section 5.2.2. Since the thermocouples are placed between the porous matrix and the surrounding ceramic insulation, measured temperatures are expected to be lower than those corresponding to the 1D volume-averaged simulation due to radial heat losses.

The pressure drop for mutually stable operating conditions is shown in Fig. 5.9,

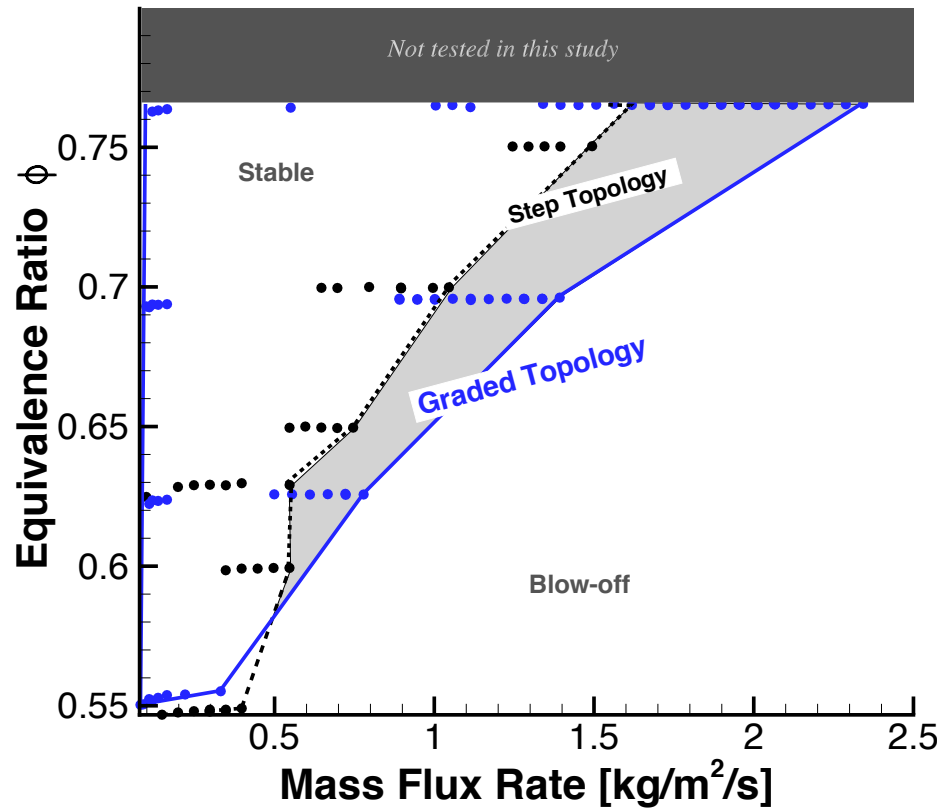


Figure 5.7: Experimental stability maps for graded (blue) and step (black) profiles, illustrating an extension of the blow-off limits for the “graded” burner. The data corresponding to this figure can be found in Table A.8 in Appendix A

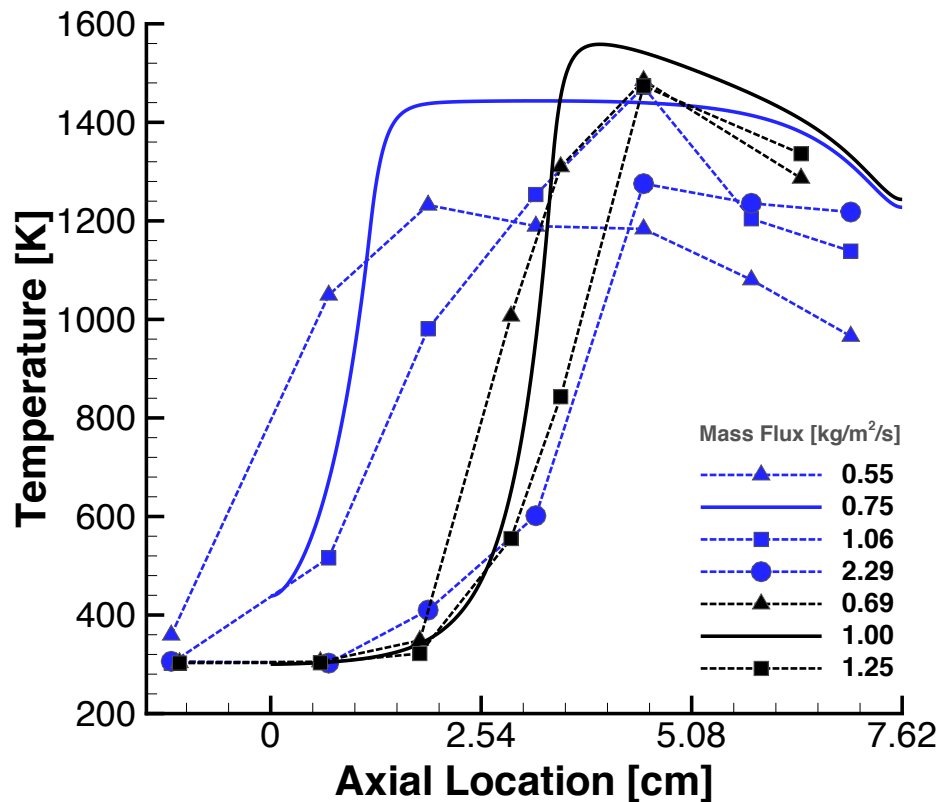


Figure 5.8: Thermocouple measurements (symbols, dashed lines) at  $\phi = 0.75$  compared to the model (solid lines), for graded (blue) and step (black) profiles. The data corresponding to this figure can be found in Table A.9 in Appendix A

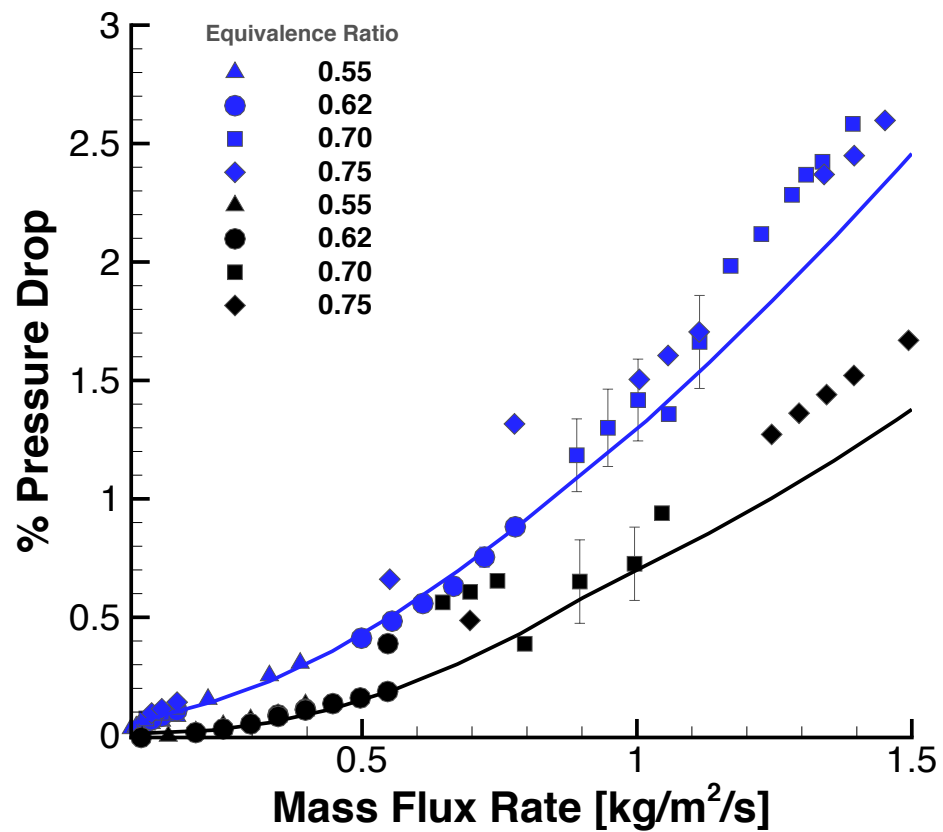


Figure 5.9: Pressure drop experimental measurements (symbols) compared to the model for  $\phi = 0.7$  (lines), for graded (blue) and step (black) profiles. The data corresponding to this figure can be found in Table A.8 in Appendix A

where error bars represent variations in pressure drop depending on the location of flame stabilization for a given operating condition. As predicted, pressure drop is higher in the “graded” burner, but does not exceed 5.4% at the highest mass flux rate ( $2.34 \text{ kg}/(\text{m}^2\text{s})$ ). Although both burners are made from the same material, and therefore have similar heat conduction properties, the solid temperatures are higher upstream of the flame in the “graded” PMB. This can be attributed to the increased radiative heat transfer. Therefore, not only is the heat exchange between the gas and solid enhanced, as predicted by the Stanton number profile in Fig. 5.3b, but also the lower radiative extinction properties in the “graded” burner enables more effective heat recirculation. The consequence of the enhanced radiative heat feedback in the “graded” burner is increasingly relevant at higher equivalence ratios, where higher mass flux rates are supported. As illustrated in Fig. 5.1, the heat exchange between the solid and gas phase decreases as mass flux rates increase, which lowers preheat temperatures and eventually results in blow-off. In the experiment, dynamic stabilization of the flame was observed in the “graded” PMB, whereas the “step” PMB anchored the flame at the interface, as expected from the burner design and computational predictions.

Although the 1D model qualitatively captures trends in flame stability and pressure drop, deficiencies are apparent. This can be explained by the Micro-CT analysis of the porous foams, which revealed a deviation from the nominal pore diameter and an inconsistent trend in cell and pore diameter in some sections (see Fig. 5.6). Specifically, the presumed gradation in the pore diameter profile, based on the foam pore density, is less pronounced. However, there is a clear gradation in the cell diameter. As discussed in Section 5.2.2, existing closure models for 1D volume-averaged governing equations in porous media combustion are mainly parameterized by porosity and pore diameter, assuming these features are the only free parameters in the geometry. However, this does not account for independent variations in other topological features, such as cell diameter, as prescribed by the fabrication method. Additionally, to avoid specifying discontinuities in the numerical solution, the interface between differing topologies is either smoothed or represented as a continuous profile. Approximation of the related physical parameters and topology discontinuities may attribute to the

discrepancy between the model predictions and experimental observations.

## 5.4 Summary

In this chapter, a novel porous matrix design is proposed, motivated by theoretically examining the governing equations and constitutive relations. The burner implements a porous matrix with a constant cross-sectional area and spatially varying pore-diameter profile. First, the impact of the porous matrix topology on the flame is illustrated by non-dimensionalizing the volume-averaged governing equations and analyzing the properties of the constitutive relations. This analysis demonstrates the significance of pore topology on the local Stanton number and optical depth properties, and consequently on the flame stability. The newly proposed “graded” PMB is studied numerically and experimentally. Results from 1D simulations showed an extensive improvement in flame stability between “step” and “graded” burners, in particular for a graded pore diameter and constant porosity profile. In subsequent experimentation of this design, it was found that the “graded” burner had  $\sim 50\%$  higher blow-off limits as compared to the “step” design.

# Chapter 6

## Enabling Tailored Porous Media Burners via Additive Manufacturing \*

### 6.1 Motivation

As described in the previous chapter, a new functionally “graded” PMB design is proposed, where the gradation in topology (i.e. porosity, pore diameter, cell diameter, etc.) enables a continuous variation of the local Stanton number and optical depth, allowing the flame to stabilize dynamically within the porous matrix and for a wider range of operating conditions. These results indicate that properties of PMBs, such as flame stability, can be optimized by tailoring the underlying porous structure. Furthermore, since the local porous microstructure directly affects global properties such as total heat transfer across a porous material or heat exchange between the working fluid and the solid structure, the ability to tailor the microstructure is desired for numerous other applications, as well.

---

\*This chapter contains work presented in [Sobhani et al. \(2019c\)](#), adapted here with modifications and extensions. In the work presented, Priyanka Muhunthan contributed to the experimentation; Shawn Allan and the Lithoz team printed the porous materials, Francesco Panerai assisted with the SEM imagining, Emeric Boigne performed the image processing of XCT scans, and Zhilong Cheng assisted with the formulation of the surface equations.

However, due to limitations in conventional ceramic foam manufacturing technologies, matrix properties such as pore diameter and porosity cannot be varied independently, hindering the ability to systematically study their effects on PMB performance. Traditional ceramic foam fabrication methods involving pressing or casting result in dense, low-porosity materials, therefore manufacturing highly porous structures requires the use of special techniques. Such techniques primarily rely on the replication of a high-porosity polymer or carbon structure either by coating with a ceramic slurry or by vapor deposition ([Binner 2006](#)). Alternatively, highly porous ceramic materials can be produced by foaming methods, which incorporate a gas into a suspension that subsequently sets to maintain the structure of the bubbles ([Studart et al. 2006](#)). However, replication and foaming techniques are not easily amenable to the tailoring of the local porous microstructure. Enabling microstructure-tailoring capabilities for optimizing performance necessitates the use of advanced manufacturing techniques such as Additive Manufacturing (AM). AM allows for the fabrication of highly complex and customized structures from Computer Aided Design (CAD) model data. The high-melting temperatures of ceramics has made them specially challenging for AM, with only a handful of technologies capable of converting a digital representation to a physical ceramic structure. An additional challenge to creating complex porous ceramic structures is resolving the sub-millimeter pore and strut features, which are relevant for practical applications.

The current AM methods applicable to ceramic parts are divided into direct and indirect techniques ([Schwentenwein and Homa 2015](#)). Direct techniques are powder-based and use thermal energy input by a laser to selectively melt or sinter the ceramic grains to form the final part (i.e. selective laser sintering/melting). In contrast, indirect techniques first print a “green part” consisting of the ceramic particles and an organic binder, which is then thermally treated to remove the organic components and sinter the ceramic grains. Lithography-based methods are a subset of indirect techniques that rely on selective space-resolved exposure to light to solidify the liquid suspension. In Digital Light Processing (DLP), a part is created from a suspension of ceramic particles in a photosensitive resin, which is shaped via photochemical reactions. A photopolymerization-based technology, such as DLP, enables higher feature

resolution and surface quality as compared to thermal energy-based methods such as selective laser sintering ([Mitteramskogler et al. 2014](#)).

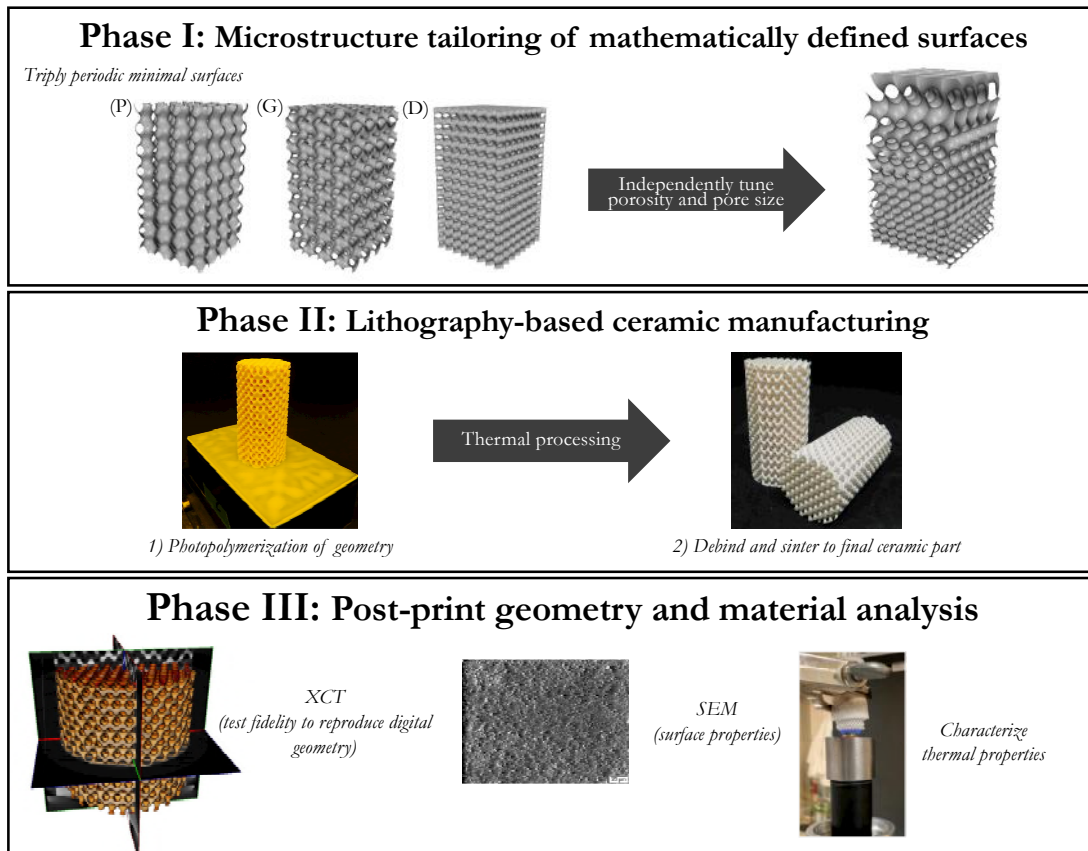


Figure 6.1: Schematic outlining the three phases of actualizing tailored porous structures, starting from design using mathematically defined surfaces, fabrication, and post-print analysis.

In this work, a framework is proposed for designing and manufacturing, using DLP to perform Lithography-based Ceramic Manufacturing (LCM), tailored ceramic porous structures for application to high-temperature environments. This framework, as summarized in Figure 6.1, is applied to PMBs to design, manufacture, and experimentally test the combustion performance of smoothly graded matrix structures. The matrix topology used as the input to the LCM is designed using periodic surface equations, as described in Section 6.2. The specifications of the materials used as well as the manufacturing methodology is presented in Section 6.3. XCT imaging was then

used to test the fidelity of the printing technology in reproducing the input STL geometry, and results are presented in Section 6.4. The printed samples were also tested to characterize the effects of feedstock particle diameter, layer thickness, and printing orientation on the macro-scale thermal and durability properties of LCM-alumina. Scanning Electron Microscope (SEM) and Energy dispersive X-ray (EDX) analysis techniques were employed to test for material degradation and chemical changes. The results of this analysis along with thermal conductivity measurements are presented in Section 6.5. Lastly, the manufactured samples are implemented in a PMB and tested over a range of operating conditions to test the feasibility and performance of AM materials in PMBs. The experimental setup and results are presented in Section 6.6.

## 6.2 Porous structures using triply periodic minimal surfaces

Previously, gradation of porous media topology was only achieved by stacking conventionally manufactured ceramic foams of different pore sizes or porosities and then sintering to create a final part. To leverage recent advances in additive manufacturing to fabricate smoothly graded porous structures, a design methodology is required to create a digital rendering of the desired structure in a format compatible with 3D printers. Thus, with the goal of manufacturing a smoothly “graded” PMB, the first step is to generate the topology of a functionally graded porous structure.

There are various approaches to creating digital representations of a porous structure, including strut-based lattice structures (i.e. body-centered-cubic) or mathematically defined structures. Approaches based on lattice structures are not easily amenable to tailoring or topology gradation, in part due to complexities in joining unit cells of different sizes. Mathematically defined structures, on the other hand, can be modified simply by changing functional parameters. Thus, the matrix unit type used in this study is based on a subset of periodic surface equations, known as Triply Periodic Minimal Surfaces (TPMS). TPMS offer several advantages over strut-based lattice structures, including high surface-to-volume ratio, enhanced pore

connectivity, and ease of functional grading (Maskery et al. 2018). TPMS are commonly used in biomedical applications for tissue and bone engineering (Maskery et al. 2018; Rajagopalan and Robb 2006; Melchels et al. 2010; Gabbrielli et al. 2008; Vijayaventaraman et al. 2018).

The topologically simplest forms of TPMS that have cubic lattice symmetry are the primitive (P), gyroid (G) and diamond (D) surfaces (Schwarz 1890; Schoen 1970), which are illustrated in Fig. 6.1. These surfaces are characterized by interconnectivity order, which quantifies the number of struts at each node of the lattice. P, D, and G surfaces have an interconnectivity order of 6, 4 and 3, respectively.

The following equations define P, D, and G surfaces, respectively:

$$F_P(x, y, z) = \cos(\omega_x x) + \cos(\omega_y y) + \cos(\omega_z z) + q, \quad (6.1a)$$

$$F_D(x, y, z) = \sin(\omega_x x) \sin(\omega_y y) \sin(\omega_z z) + \sin(\omega_x x) \cos(\omega_y y) \cos(\omega_z z) + q \quad (6.1b)$$

$$F_G(x, y, z) = \cos(\omega_x x) \sin(\omega_y y) + \cos(\omega_y y) \sin(\omega_z z) + \cos(\omega_z z) \sin(\omega_x x) + q, \quad (6.1c)$$

where  $\omega$  and  $q$  control the pore density (e.g. pore size) and porosity, respectively. The  $F = 0$  isosurface is treated as a boundary separating solid and void regions of a 3D structure. Regions where  $F \leq 0$  is defined to be solid and regions where  $F > 0$  is void space.

To facilitate lattice functional grading of porosity and pore size, the D-surface equation (Equation (6.1b)) is adjusted such that either  $\omega$  and/or  $q$  are replaced by spatially-dependent parameters. In the current study, the following functions were used to generate grading in the axial direction:

$$q(z) = q_1 + \frac{(q_2 - q_1)z}{L}, \quad (6.2a)$$

$$\omega(z) = \omega_1 + \frac{(\omega_2 - \omega_1)z}{L}, \quad (6.2b)$$

where  $L$  is the axial height of the sample, and subscripts 1 and 2 refer to the limits of

the parameter within the sample. These parameter limits are first determined from the desired limits of porosity and pore size.

Once the desired geometry is modeled, an isosurface is created and converted to a stereolithography (STL) file for input to the printer system, using the mathematical modeling software MathMod. The fabrication of the digital geometry is described below.

### 6.3 Fabrication methodology

In the present study, DLP is used to perform LCM for fabrication of tailored porous structures. Before input to the printer, the geometry is first modified in order to address over-polymerization within the layers (XY-plane) and across the layers (Z-plane), respectively. To ensure adhesion between exposed layers, the depth of cure is generally larger than the layer thickness. This has the undesired effect that light can cure regions where no curing was planned (i.e. Z-plane over-polymerization). For Z-plane corrections, light exposure to certain features is delayed to offset the effects related to the penetration of light through the slurry between layers. Over-polymerization can also simultaneously affect the XY-plane, due to light scattering in the slurry. To compensate for these effects, features are enlarged or shrunk (i.e. by adding or removing pixels around the feature). After the digital file is corrected for over-polymerization, it is then scaled up to the known shrinkage value for the materials used.

The printer used in this study is the CeraFab 7500, which uses blue LED light and a digital light projector to create an array of  $40\ \mu\text{m}$  pixels over a  $76 \times 43\ \text{mm}$  area. The printer functions with the same principles as stereolithography and DLP systems for printing polymers. Each layer is produced by illuminating the slice image, using a monochromatic (450 nm) projector, into the vat of slurry, with a slurry depth of approximately  $250\ \mu\text{m}$ . The light penetration depth, equal to  $200\ \mu\text{m}$  for the current study, must be at least two to three times higher than the layer height to ensure good adhesion between the layers. In this study, samples were printed using 25 or  $50\ \mu\text{m}$  layers. Two different grades of high-density and high-purity alumina, LithaLox

HP500 and LithaLox 350D, were used. The 350D material, referred to as material A, is 99.8% Al<sub>2</sub>O<sub>3</sub>, with powder particle sizes from  $\approx 0.5$  to  $1\ \mu\text{m}$  that sinters together to approximately 98% density. The HP500 material, referred to as material B, has a higher purity of 99.99% Al<sub>2</sub>O<sub>3</sub>, with particle sizes from 0.1 to  $0.5\ \mu\text{m}$  that sinter to form over 99.4% density. The other distinguishing feature between the two alumina materials is the surface roughness, which is reported by the manufacturer as  $0.9\ \mu\text{m}$  for 350D and  $0.4\ \mu\text{m}$  for HP500. The variation in surface roughness and microporosity are evident in the SEM images shown in Fig 6.2, which were taken using an XL30 Environmental Scanning Electron Microscope.

Contour Offset and Z-compensation, often used in lithography processes, are techniques used to modify the input to the printer to address over-polymerization caused by light scattering in the slurry within the layers (XY-plane) and across the layers (Z-plane), respectively. In regions where there are holes, at the boundary between illumined pixels and those areas that should not be illumined, light scattering results in the over-polymerization and a smaller hole diameter than what is prescribed. Contour offset adds or removes pixels from all of the edges within an exposed layer to compensate for this effect. Conversely, Z-compensation delays the light exposure to certain features to offset the effects related to the penetration of light through the slurry between layers. To ensure adhesion between exposed layers, the depth of cure is generally larger than the layer thickness. This has the undesired effect that light can cure regions where no curing was planned, specifically in the layers that were exposed directly before. As a result holes, ending channels or similar structures will be shortened in build direction. To compensate for that effect, the Z-compensation algorithm extends every opening or hole in build direction for a given layer count.

By curing the resin with UV or visible light, the polymer matrix builds up a three-dimensional composite of photopolymer and ceramic powder, called a green part. The green part is removed from the printer for post processing, where the excess slurry is cleaned from the parts with the use of a cleaning solution (LithaSol 20, Lithoz, GmbH), compressed air, and an ultrasonic bath. Cleaning is critical for removing the excess slurry that is retained by matrix structures due to capillary adhesion. The green parts are then thermally processed to remove the organic material and then

sintered to form the final ceramic part.

Forming ceramics out of a slurry, as done in LCM, promises high solids loading, which in turn enables equivalent strength properties as products of conventional forming methods such as injection molding or dry pressing, but with greater geometric flexibility.

Next, the following post-print analysis techniques are implemented to test the fidelity of the printer to reproduce the input geometry, the effects of the alumina material used and printer layer depth on thermal conductivity, and the material durability at high-temperature conditions.

## 6.4 XCT analysis of printed porous structures

Four porous samples were printed to construct three burners—two “graded” burners consisting each of one porous structure, and one “step” burner consisting of two different, yet uniform, porous structures. The burners tested consisted of AM alumina porous structures with different pore size, porosity, and gradation profiles, outlined in Table 6.1. Burner 1 is graded in porosity and constant in pore diameter profile, and conversely, burner 2 is graded in pore diameter and constant in porosity. Burner 3 is equivalent in pore diameter and porosity to Burner 2, but consists of a step topology design instead of a graded one.

Pore diameter is defined based on the porosity and pore density. Given the total volume of the void space, number of pores, and assuming that each pore is a sphere, the pore diameter based on void volume is defined as:

$$d_v = 2 \left( \frac{3V_p}{4\pi N} \right)^{1/3} \quad (6.3)$$

where  $V_p$  represents the total volume of void space and  $N$  represents the number of pores in that volume. Given an input pore diameter and porosity profile, the corresponding  $q$  and  $\omega$  parameters are computed for Eq. (6.1) and (6.2).

To test the accuracy of the LCM technique in actualizing the digital design, the final sintered porous structures are analyzed using Micro-XCT imaging using a ZEISS

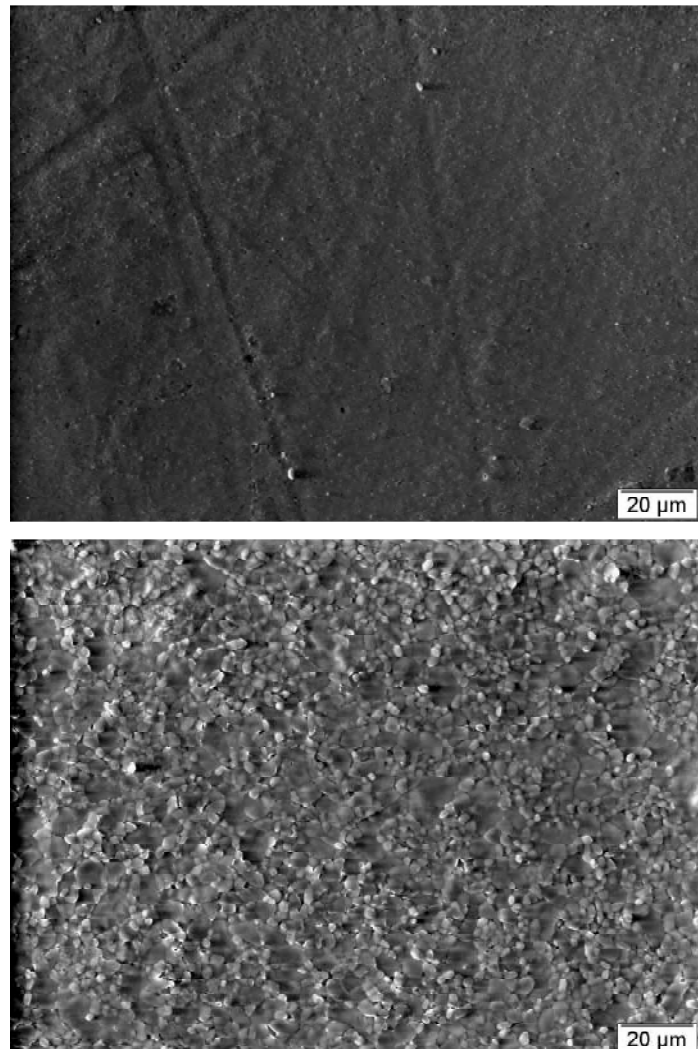


Figure 6.2: SEM images, at 650 times magnification, of wafers of the HP500 material A (top) and 350D material B (bottom) alumina, illustrating the variation in surface roughness and microporosity between the materials.

Burner 1	Burner 2	Burner 3
graded porosity $d_v = 2.5 \text{ mm}$ $\epsilon = 65\text{-}85\%$ $H = 75 \text{ mm}$ $D = 20 \text{ mm}$	graded pore diameter $d_v = 1.5\text{-}3.5 \text{ mm}$ $\epsilon = 75\%$ $H = 75 \text{ mm}$ $D = 20 \text{ mm}$	step pore diameter $d_v = 1.5, 3.5 \text{ mm}$ $\epsilon = 75\%$ $H = 75 \text{ mm}$ $D = 20 \text{ mm}$

Table 6.1: Geometric parameters for the burners tested, where  $d$ ,  $\epsilon$ ,  $H$ , and  $D$  refer to pore diameter, porosity, burner height, and burner diameter, respectively.

XRADIA 520 VERSA X-ray Microscope for XCT with a resolution of  $12 \mu\text{m}$ . XCT is used to compare the three-dimensional features of the printed parts to those of the input model data. Porosity, mean pore and cell diameters were estimated along the axial direction of the cylindrical ceramic pieces, using the methods discussed in Section 5.3.2. The strut throats, defined as the thinnest part of the struts, were extracted by applying the same algorithms on the solid domain instead. The cell diameters were then computed as the diameters of spheres of equivalent volumes, whereas the pore and throat diameters were obtained as the diameters of the circles of equivalent areas. Figures 6.3–6.5 illustrate the porosity, pore and cell diameters of burners 1–3, as measured from the XCT scan and aforementioned image processing algorithms. Since a different definition of the pore diameter is used in processing the 3D structures as in deriving the theoretical value (Eq.( 6.3)), the quantitative value does not correspond to the measurements for any of the burners.

For burner 1, designed with a gradation in porosity and constant pore size, Fig. 6.3b illustrates that the final print faithfully represents the constant pore diameter profile and Fig. 6.3c shows the intended linear porosity profile.

Figure 6.4 also compares the result of these algorithms applied to the input STL geometry of burner 2, for comparison. Furthermore, Fig. 6.4c illustrates the effects of the segmentation and image processing on the computation of the porosity profile, which varies by 10% between the STL-geometry and that of the theoretical value (Table 6.1). However, for burner 2, the constant porosity profile was not achieved, as illustrated in Fig. 6.4c. Instead, a linear decay in porosity of  $\sim 10\%$  is measured. This effect can be accounted for by analyzing the strut throat diameters between

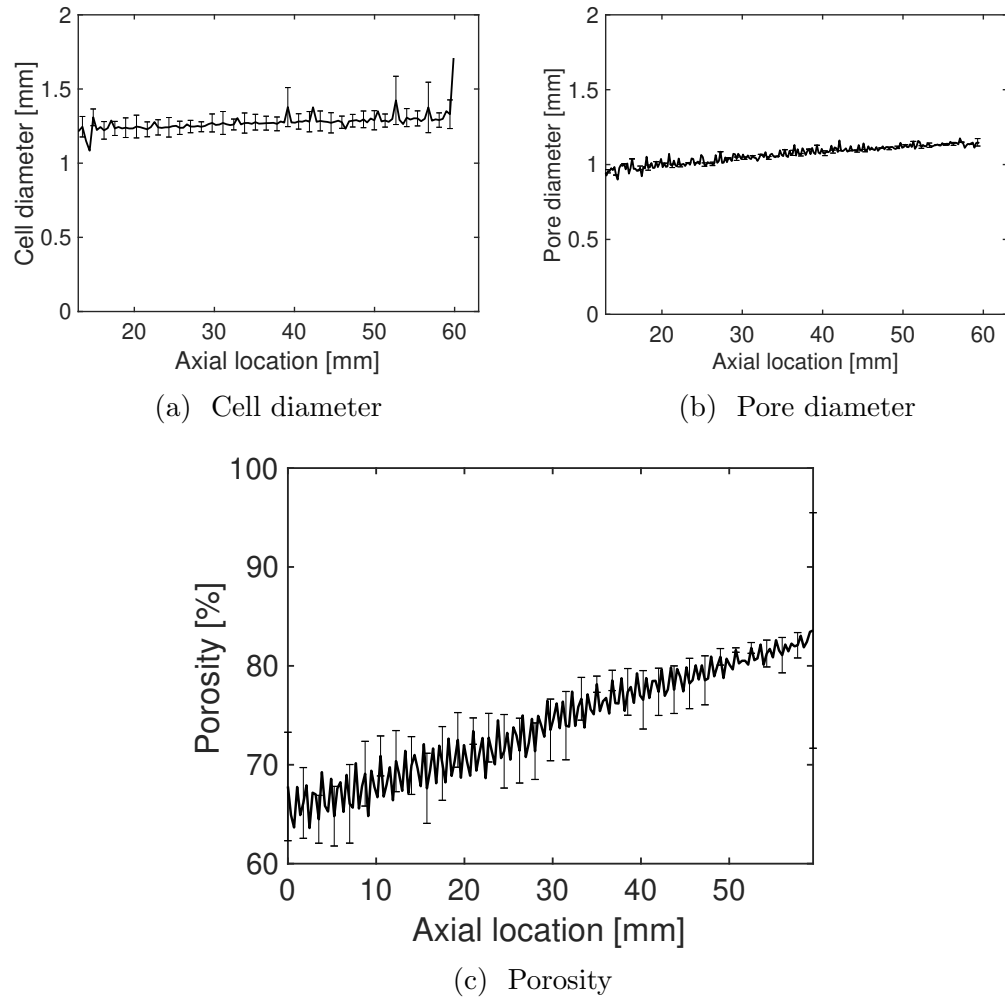


Figure 6.3: XCT measurements of cell diameter, pore diameter, and porosity of burner 1.

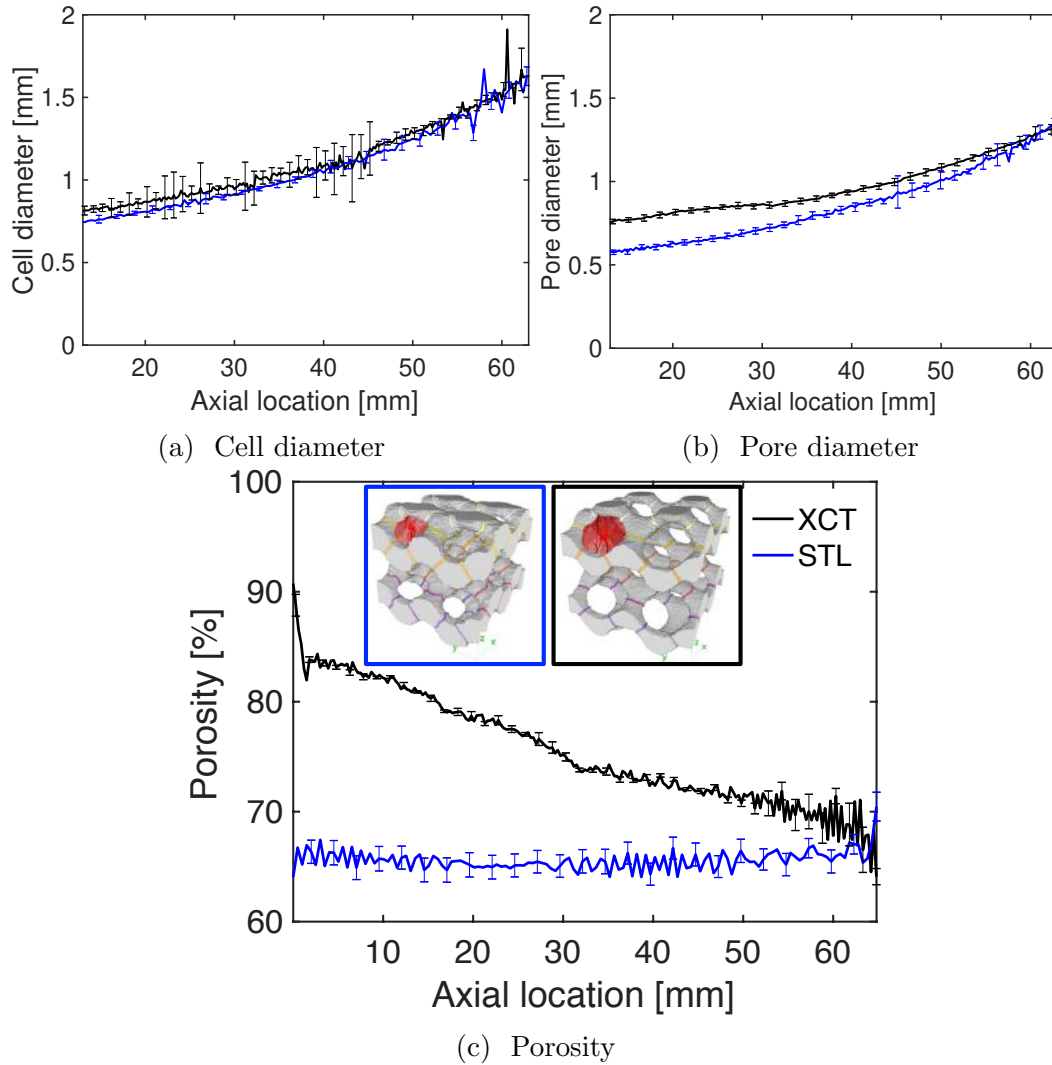


Figure 6.4: Variations between the designed and final printed structure for burner 2, in (a) cell diameter, (b) pore diameter, and (c) porosity, illustrating four cells with red surfaces to represent the locations and morphologies of two pores, and colored rings on the struts represent the throat locations. The mean diameters of the throats pictured were estimated as  $352 \mu\text{m}$  for the original geometry, versus  $229 \mu\text{m}$  for the 3D printed sample.

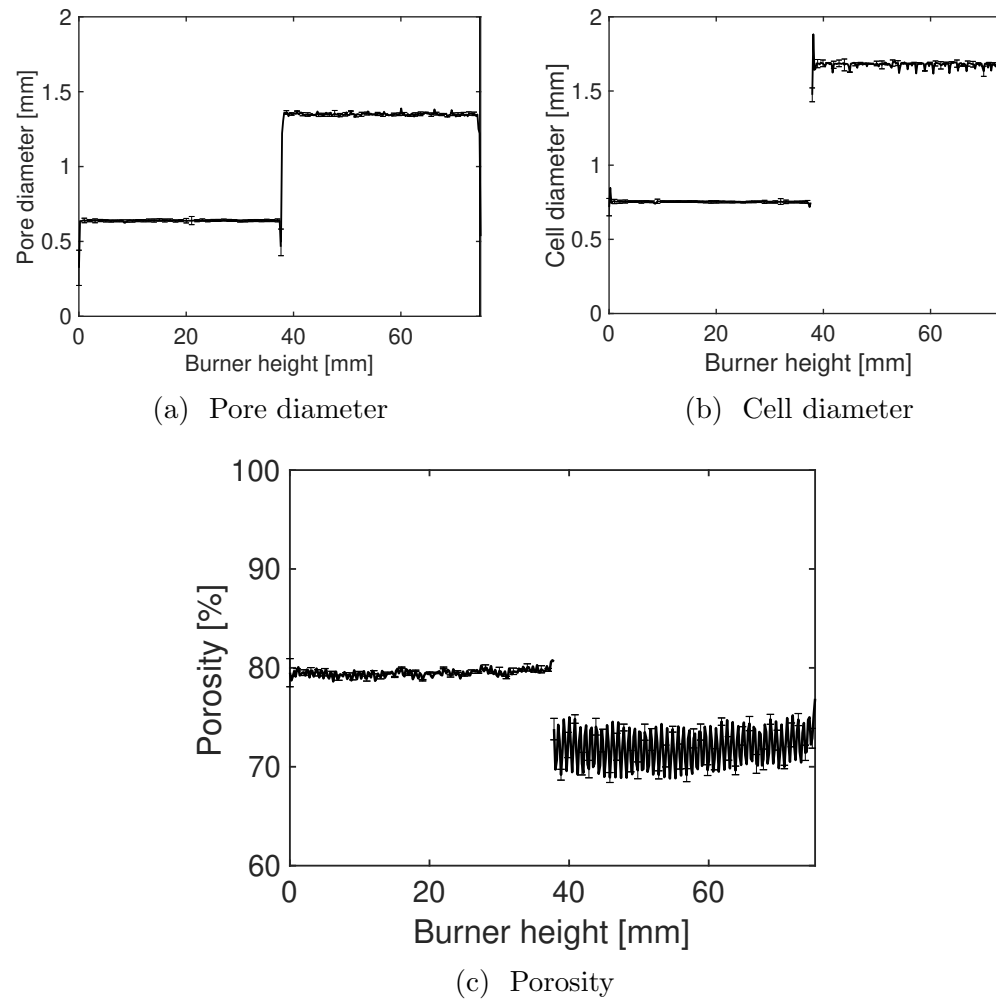


Figure 6.5: XCT measurements of cell diameter, pore diameter, and porosity of burner 3.

the input STL geometry and that of the final print. The mean diameters of the throats in Fig. 6.4c were estimated as  $352 \mu\text{m}$  for the original geometry and  $229 \mu\text{m}$  for the 3D printed sample. Although the same energy is used for all samples, the thinner struts have less absorption and thus become even thinner than what the input STL prescribes. The strut thinning effect results in larger pore diameters and higher porosity, as shown in Fig. 6.4. Although the pore space is larger than designed, the inputted gradation in pore size is achieved in the final print.

Burner 3, designed as a direct “step” profile comparison with burner 2, has the fidelity in capturing the input geometry profile, exhibiting a 10% decrease in porosity across the two samples and an increase in pore size, as shown in Fig. 6.5. The discrepancy is again assumed to occur from the difference in energy absorption of the thin strut regions. However, the goal of manufacturing comparable burners with graded and step porosity and pore size profiles was successfully achieved.

## 6.5 Thermal conductivity and durability of additive manufactured alumina

Disk samples of each material were printed to measure the effect of printing layer thickness, orientation, and material composition on effective thermal conductivity. The first orientation is the XY-orientation, where the printed layers are parallel to the face of the disk. The other orientation is the Z-direction, where the layers are perpendicular to the face of the disk. The 350D samples were printed with two different layer thicknesses ( $25$  and  $50 \mu\text{m}$ ) and in two orientations, while the HP500 sample was printed only in  $25 \mu\text{m}$  and XY-orientation. The thermal conductivity of the samples were characterized using the modified transient plane source (MTPS) method. Prior to testing the samples, a blotter test was performed to ensure valid testing thickness. A blotter test involves performing a measurement with and without an insulative layer as a backing material between the sample and the applied weight. For samples of valid thickness, no differences are observed between tests. Samples that are too thin will result variability between measurements due to the heat pulse completely

penetrating past the sample boundary. Tests were performed at 298K, 373K, and 473K, with distilled water as the contact agent for tests at 298K and Wakefield 120 Thermal Grease at elevated temperatures. Prior to testing, a reference material evaluation was performed to validate the instrument and ensure proper operation. Each reported test result is the average of five measurements, which is then repeated three times for a total of 15 tests per sample. The averaged value of the three measurements are shown in Figure 6.6. The maximum standard deviation was 4%. Additionally, the thermal conductivity of conventionally manufactured high-grade alumina is also shown.

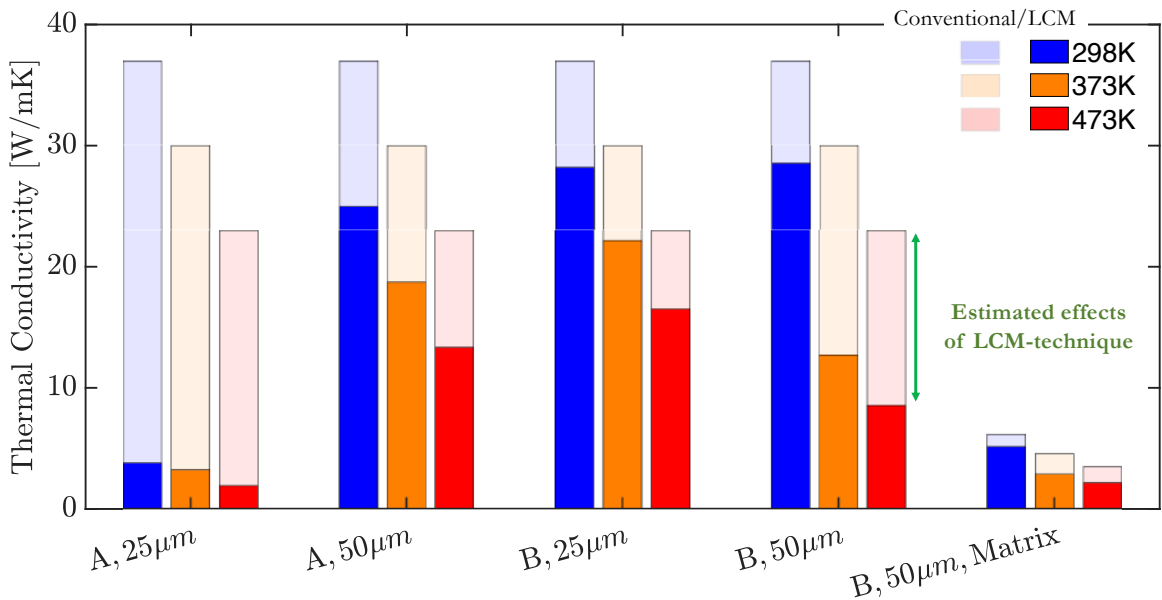


Figure 6.6: Thermal conductivity measurements at various temperatures of the solid disks and porous structure, with material A and B corresponding to Alumina 350D and HP500, respectively. All data presented correspond to samples printed with XY-plane layer orientations, with thermal conductivity measured in the Z-direction. The data corresponding to this figure can be found in Table A.10 in Appendix A

The temperature dependence is approximated using the following expression ([Auerkari 1996](#)):

$$\lambda_{s,conv} = 5.5 + 34.5 \exp(-0.0033(T - 273)) \quad (6.4)$$

All measured values deviate from the thermal properties of common high-grade (at least 99% purity) alumina ceramics prepared by conventional approaches. The effect of this discrepancy originates from the specific nature of the fabrication technique (lithography-based method) as well as the effectiveness of the layer-to-layer adhesion and particle-particle sintering (i.e. material density).

As an artifact of the layered forming process in LCM, the material micro-porosity is greater between layers than within each layer, thus resulting in anisotropic material properties. Samples with a Z-plane orientation of layers displayed significantly higher heat transfer than samples with an XY-orientation, since the temperature gradient was applied across the high-density layers. Although the tests indicated significant anisotropy in thermal conductivity, there was high variability between the iterations of the Z-plane sample tests, therefore accurate estimates of the thermal conductivity were not possible. Therefore, the data presented correspond to samples printed with XY-plane layer orientations, with thermal conductivity measured in the Z-direction.

Additionally, it is expected that the high-density material B (HP500) has higher thermal conductivity than the material A (350D), which is confirmed by comparing the measurements of 25  $\mu\text{m}$  layer material B to those of material A. At higher temperatures, the thicker layered material B sample had a significantly lower thermal conductivity. Beyond micro-porosity between and within the layers, layer-to-layer adhesion can significantly change the material thermal conductivity, due to decreased contact between each layer. It is hypothesized that the significant deviation in conductivity of alumina 350D (i.e. material A) 25  $\mu\text{m}$  layers, is a result of reduced layer-to-layer adhesion (i.e. delamination).

The thermal conductivity of a printed porous structure is also measured in order to quantify its dependence on the constituent material properties and geometry. The effective thermal conductivity of an HP500 (i.e. material B), layer thickness 50

$\mu\text{m}$ , matrix was measured and compared to simulations results, using the software PuMA ([Ferguson et al. 2018](#)). For the simulation, an XCT-reconstruction of a  $3 \text{ mm}^3$  matrix domain is first imported and segmented to identify the solid and void space. Next, the conductivity of the constituents – HP500,  $50 \mu\text{m}$  layer thickness alumina and air– are specified to correspond with the voxels identified as solid or void, respectively. Finally, the steady state heat conduction equation is then solved using a finite difference method with a prescribed temperature differential in the simulation direction and periodic boundary conditions in the side directions. This process is repeated for the three temperatures tested. The simulation results are within 5% of those measured at all temperatures, thereby confirming that the constituent material thermal conductivity and geometry (from XCT) are sufficient to predict the effective properties of a printed porous structure. For diamond (D) surfaces matrix structure tested, the relationship is described by the following equation:

$$\lambda_{s,eff} = \alpha(1 - \epsilon)\lambda_s(T) \quad (6.5)$$

where  $\lambda_{s,eff}$  is the effective thermal conductivity,  $\alpha$  is a correction factor corresponding to the geometry ( $\approx 0.4$  for the D-surface structure),  $\epsilon$  is the porosity, and  $\lambda_s(T)$  is the constituent material thermal conductivity as a function of temperature. For the temperature range tested,  $298K < T < 473K$ , the following dependence is observed:

$$\lambda_s(T) = aT^2 + bT + c \quad (6.6)$$

where a, b, and c for HP500 alumina is approximately  $1e-3$ ,  $-0.87$ , and  $200$ , respectively. Using this expression, the effective conductivity using the constituent values from conventionally manufactured high-grade alumina (Equation 6.5) is predicted and compared to that measured in the LCM-alumina matrix (final group of columns in Figure 6.6). This analysis illustrates that, assuming sufficient layer-to-layer adhesion, the LCM process reduces the effective conductivity by at least 20%, as compared to other manufacturing techniques.

In addition to thermal conductivity testing, a bunsen burner was setup to test

the material durability of the final sintered HP500, 50  $\mu\text{m}$  layer thickness, alumina porous matrix exposed to combustion environments. The matrix was mounted 3 mm above the lip of the burner, shown in Fig. 6.7, operated with methane at equivalence ratio  $\phi = 0.9$ . At this operating condition, the flame temperature is  $\approx 2100$  K. Before the start of the test and after time intervals of 1, 6, and 24 hours, the surface exposed to the flame was imaged using a SEM, and the results are shown in Fig. 6.8. EDX analysis was also performed to identify the elements for the material and create elemental surface maps, and the results are shown in Fig. 6.9.



Figure 6.7: Bunsen burner setup used to test the material durability of the additive manufactured alumina.

The SEM images after each time interval, as shown in Fig. 6.8, are not taken at the same location, therefore visual differences in the surface properties may be due to pre-existing heterogeneities. First, the pre-combustion SEM images manifest

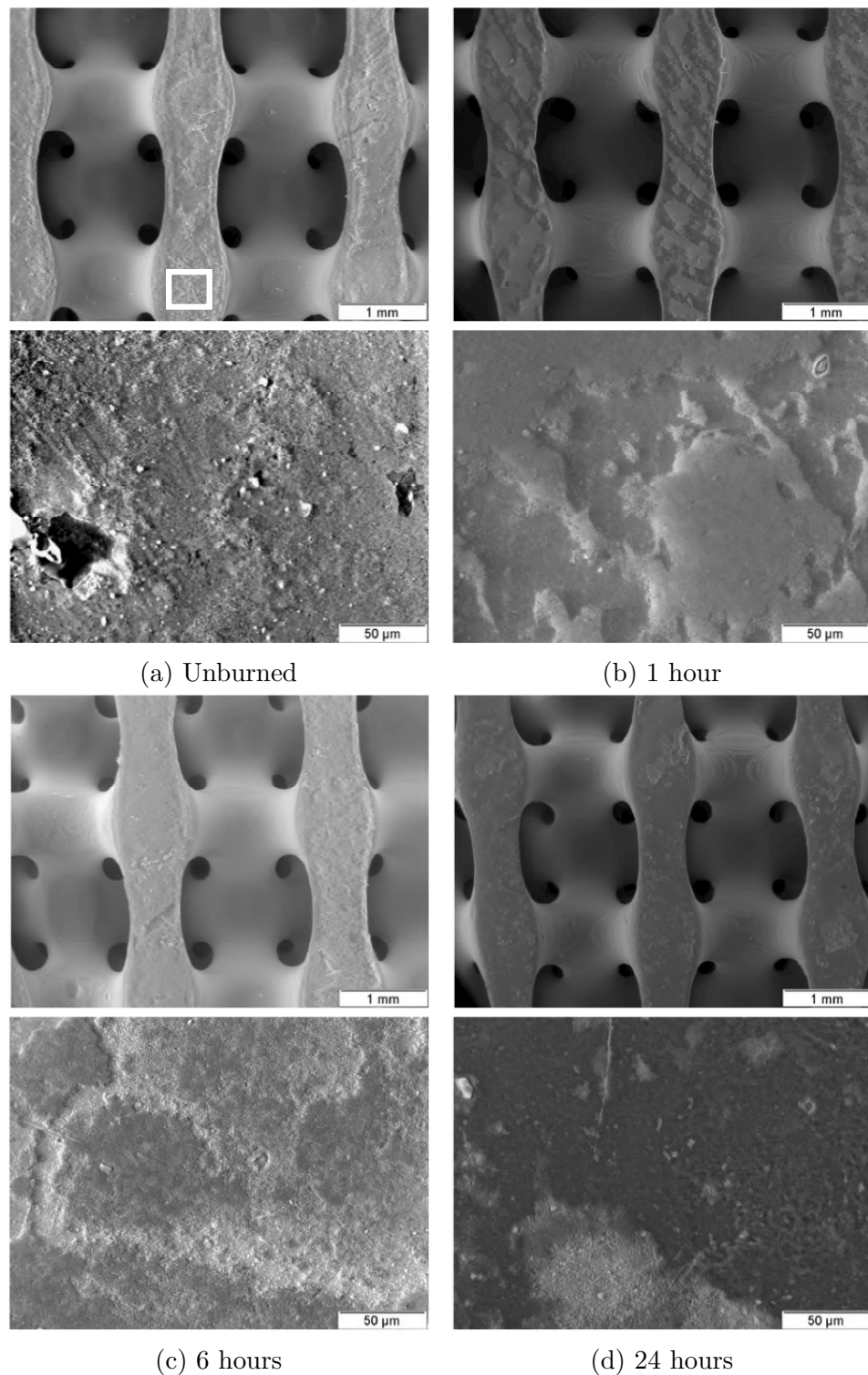


Figure 6.8: SEM images of the porous matrix before and durability testing, at 25 $\times$  and 500 $\times$  magnification near the location of the exposed strut shown in the white box of (a).



Figure 6.9: 25X magnified SEM (left) and EDX composition maps after 1 hour of combustion of Al (middle) and O (right).

the artifact of the layer-by-layer printing process as well as the sintered. The main conclusion from the SEM analysis is that the additive manufactured alumina remains very stable upon long flame exposures. The results illustrate that the material does not undergo any cracking or significant surface transformations even after 24 hours of exposure to the combustion environment. Figure 6.9 shows the elemental surface map of a 25X magnification SEM image after 1 hour of combustion. The EDX did not show any chemical changes or contamination of the material, measuring primarily Al and O elements before and after the combustion experiments. Therefore, the manufacturing technique and matrix geometry proposed in this work result in materials that are chemically stable for high-temperature combustion applications.

## 6.6 Tailored structures implemented in porous media burners

Lastly, informed by previous computational predictions of graded pore diameter profiles, ceramic porous structures are designed, manufactured and tested in a PMB experiment to illustrate the potential system performance enhancements using tailored porous structures.

### 6.6.1 Experimental setup

The burners tested consisted of AM alumina porous structures with different pore size, porosity, and gradation profiles, as outlined in Table 6.1. The burner geometries tested were printed in 350D alumina, 50  $\mu\text{m}$  layers. In addition, one HP500, 50  $\mu\text{m}$  layers, sample with the same geometry as the large pore section of burner 3 was printed and tested for comparison. The pore diameter and porosity profiles tested were based on the previous study described in Chapter 5. The porous samples were wrapped in insulation and housed in a quartz tube (see Fig. 6.10). All experiments were performed using a methane/air mixture at atmospheric pressure. Flow rates of reactants were measured and controlled using Alicat Scientific mass flow controllers. Compressed air and methane flows were mixed at a tee-junction approximately 200 tube diameters upstream of the burner to achieve a homogeneous mixture prior to entry into the burner.

Six K-type mineral-insulated thermocouples were placed along the axial profile of the burner at azimuthal locations varying by 60°. Temperature measurements were primarily used to determine flame location and stability. Stable operation was defined as continuous operation without changes in thermocouple measurements greater than 5 K over 5 minutes. After each stable operating condition was determined, the mass flux was changed to find the maximum stable flow rate for each equivalence ratio. The blow-off limit was determined first by the occurrence of the maximum temperature measurement at the thermocouple furthest downstream, and subsequently by the continual decrease in temperature measured by this thermocouple. Flashback was determined similarly, except that the maximum temperature was observed at the thermocouple furthest upstream, followed by a decrease in temperature of its adjacent thermocouple.

### 6.6.2 Results and discussion

Flame stability measurements are presented for the three burners outlined in Table 6.1, printed in 350D alumina, 50  $\mu\text{m}$  layers. At each equivalence ratio, the inlet conditions resulting in a stable flame are shown in Fig. 6.11. The graded porosity

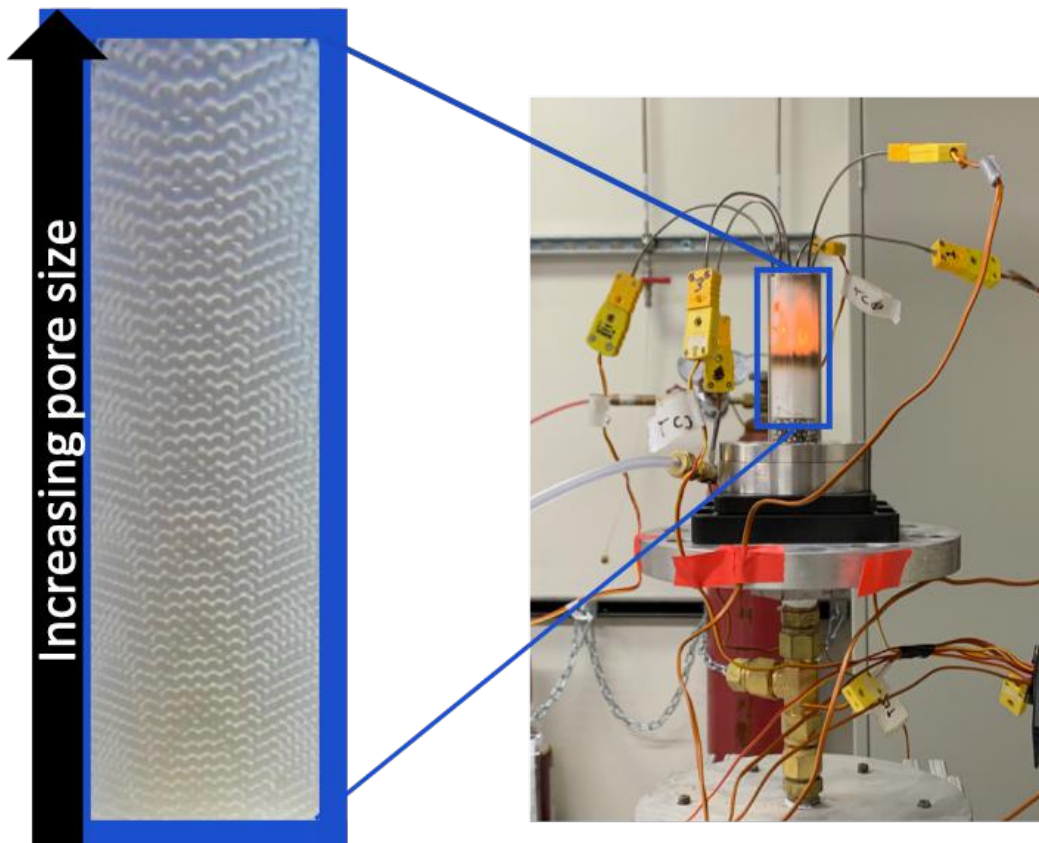


Figure 6.10: (Left) Porous structure with graded pore diameter ( $d = 1.5\text{-}3.5\text{ mm}$ ) and constant porosity (75%) profile after binder burnout and sintering of green part. (Right) Experimental setup illustrating the burner in operation with instrumented thermocouples. Methane/air flows from bottom to top, and the flame is visible through the insulation and quartz tube.

burner, burner 1, was only stable at  $\phi = 0.6$ , since at leaner conditions, the flame would either extinguish or blow off, and at richer conditions, the flame would flashback. However, burner 1 had a 80% higher blow-off limit at this equivalence ratio, as compared to burner 2.

Burner 2, with a graded pore diameter profile, has a significantly wider range of stable operating conditions. The maximum limit for stability, after which an increase in inlet mass flux would result in blow-off, increases with decreasing  $\phi$ . The minimum limit, however, is the relatively constant for the range of  $\phi$  tested. Burners 1 and 2 each isolate the effects of the matrix-pore diameter and porosity on the flame stability performance. Although both burners have the same average pore diameter and porosity, the flame behavior is significantly affected by the difference in local properties. The smaller pore diameter region in Burner B inhibits flashback, while facilitating sufficient preheating to delay blow-off at higher velocity conditions. Burner 3, the “step” equivalent to burner 2, has a smaller stable operating range, as predicted by previous analysis in Chapter 5.

The results from this experiment showed a significant extension of the stable operating conditions using a smoothly-graded pore diameter matrix as compared to a conventional two-zone design. At different operating conditions, the flame dynamically stabilizes in the matrix and thus, enables stable operation of a wider range of equivalence ratios.

During the PMB test, the flame was embedded in the burner for several hours, after which the matrix had significant damage even though the time of the PMB experiment was shorter than the durability study. This implies that although the material is properly sintered and not affected by manufacturing defects, as exhibited by the uniform heating in the durability study, it undergoes strut cracking and breakage when exposed to non-uniform thermal expansion. An XCT scan of a small broken fragment is shown in Fig. 6.12, using a ZEISS XRADIA 520 VERSA X-ray Microscope for XCT with a resolution of  $1.6 \mu\text{m}$ . In addition to the evidence breakage, the high-resolution scans illustrate additional micro-fissures within the structure.

Since crack development is impeded by grain boundaries, a finer-grained alumina such as the HP500 is expected to have higher wear resistance than 350D ([Ruys 2019](#)).

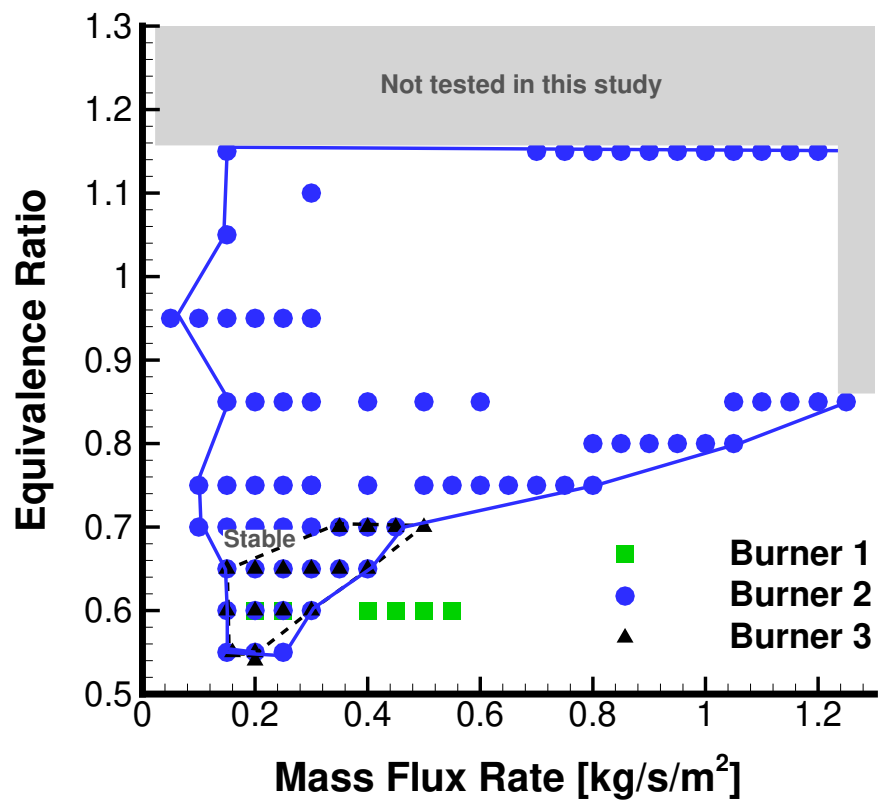


Figure 6.11: Experimental flame stability measurements, illustrating maximum and minimum stable mass flux at each equivalence ratio,  $\phi$ , tested in burner 1–3 (see Table 6.1). The data corresponding to this figure can be found in Table A.11 in Appendix A

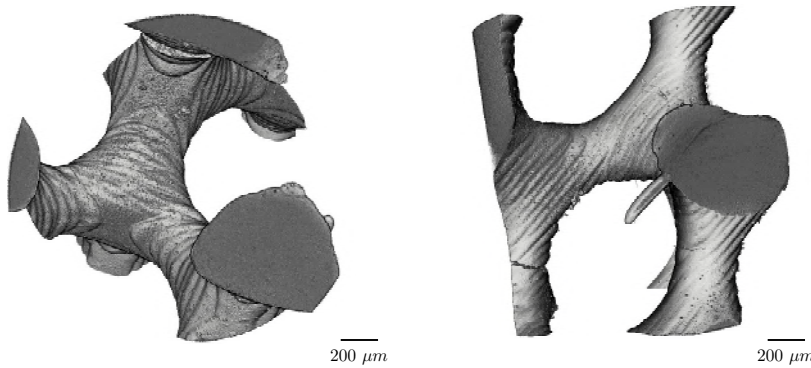


Figure 6.12: XCT scan of a small broken fragment of the 3D printed 350D alumina matrix, post-PMB experimentation.

Indeed, combustion experiments of both materials illustrated that the HP500 material was significantly more durable than the 350D. Although both eventually experienced breakage at the struts, the HP500 exhibited enhanced material integrity and few cracks. Alternative strut morphology and optimized matrix designs may further alleviate thermal shock concerns related to heterogeneous heating, as experienced in embedded flame PMB's.

## 6.7 Summary

In this study, the feasibility of application-tailored PMBs is demonstrated using Triply Periodic Minimal Surfaces to design the porous structure and lithography-based AM for fabrication. 3D structures with specified axial porosity and pore diameter profiles were translated from computer models into physical samples, which were then tested in PMB combustion experiments. Samples were printed via Lithography-based ceramic manufacturing using two different alumina feedstocks and at 25 or 50  $\mu\text{m}$  layer thickness. The effects of the material composition on the matrix properties were tested, showing that finer sintered alumina particles result in 3D printed structures with greater durability. SEM and EDX analysis showed negligible material degradation of the printed alumina after 24 hours of flame exposure. Additionally, the finer material (i.e. HP500 alumina) exhibited a higher thermal conductivity than the 350D

alumina material, at all three temperatures tested.

The matrix topology was designed by modifying Triply Periodic Minimal Surface equations to introduce gradation in the structure. XCT imaging and analysis of the final printed parts illustrated a deviation from the input geometry for geometries with thin struts—specifically a higher effective porosity than that prescribed. Lastly, the manufactured samples were implemented in a PMB test the feasibility and performance of AM materials in PMB.

Results from these experiments show a wide range of stable operating conditions in AM ceramic porous media, depending on the geometric profile implemented. The largest stability regime resulted from a smoothly-graded pore diameter matrix as compared to a conventional “step” PMB. At different operating conditions, the flame dynamically stabilized in the matrix and thus, enables stable operation of a wider range of equivalence ratios. Previous experimental studies of PMBs used conventionally manufactured porous foams, limiting the study of the isolated effects of topology gradation, porosity distribution, and pore diameter profiles on the burner performance. The current study is an example of how the matrix topology can be tailored to achieve drastically different burner performance. As illustrated in this work, recent advances in AM for ceramics enable the design and manufacture of fully tailored PMBs, both to improve the fundamental understanding of combustion in porous media and to create application-specific designs.

# Chapter 7

## Conclusions and future work

### 7.1 Main findings

This dissertation contributes both to the analysis of combustion in porous media, characterization of performance in conventional PMBs, and the development of a novel porous matrix design for enhanced system performance to demonstrate the potential of PMBs to overcome technological barriers associated with conventional free-flame combustion technologies.

First, at atmospheric pressure and methane-fuel operation, the flame stability, pressure drop, CO and  $\text{NO}_x$  emissions, and material durability of five conventional “step” PMBs were tested. This burner design utilizes a two-zone “step” topology concept in which the flame stabilizes at the interface between two porous matrices of different topologies. Results from the experiments are presented and compared to 1D volume-averaged simulation results. All  $\text{NO}_x$  emissions were low and measured below 14 ppm. CO emissions were highest at lower flow rates, where low temperatures hinder complete CO oxidation. The results illustrate that by using low heat conductivity material (i.e. YZA) upstream and high conductivity material (i.e. SiC) downstream, maximum flame stability can be achieved.

Material durability tests were conducted for the burner with maximum flame stability, composed of a 3 PPI SiC downstream section and a 40 PPI YZA upstream section. Long-term material durability tests at steady-state and cycled on-off conditions

were done to investigate the feasibility of these materials in industrial applications. XCT analysis was used to study the internal structure of the porous matrix. Although the 3 PPI SiC in the downstream combustion zone exhibited superior pressure drop and stability behavior, local cracks developed in the flame region during the cycle testing.

Next, the burner configuration identified was applied for high-pressure testing and durability analysis. This burner successfully operated with liquid heptane, fully vaporized and premixed with air at 2, 8, and 20 bar absolute pressure with preheat values of around 500 K. The burner was also tested with methane at 8 bar to compare with heptane performance as well as previous gaseous methane experiments at atmospheric conditions. The XCT analysis, similar to the durability tests at atmospheric conditions, revealed micro-cracks in the combustion zone porous media. In future work, reinforced material such as silicon infiltrated silicon carbide, with high thermal conductivity and high thermal shock and corrosion resistance, can be tested to alleviate the durability concerns.

For all high-pressure tests, the burning velocity in the PMB was measured 2–10 times higher than the laminar flame speed. Methane combustion at 8 bar was significantly more stable than heptane. The pressure drop was shown to decrease with increasing operating pressure, although independent of fuel.  $\text{NO}_x$  measurements were < 25 ppm for all stable operating conditions, for which complete oxidation of CO was observed. Next, theoretical, computational and experimental investigations were conducted to explore the potential performance benefits of topology grading in porous media combustion. Gradation was motivated by theoretically examining the governing equations and constitutive relations, revealing the significance of pore topology on interphase heat exchange and radiative heat transfer properties, and consequently on the flame stability. Specifically, the local Stanton number and optical depth were proposed as the quantities of interest for predicting trends in dynamic flame stabilization. Results from 1D simulations showed an extensive improvement in flame stability between “step” and “graded” burners, in particular for a graded pore diameter and constant porosity profile. This design was chosen for the experimental investigation of “graded” versus “step” PMBs, which qualitatively confirmed an enhancement of

flame stability by  $\sim 50\%$ .

The graded porous matrix topology was experimentally investigated by considering a step-wise sequence of conventionally manufactured porous disks. In fact, in all previous experimental studies of PMBs, conventionally manufactured porous foams were implemented, limiting the study of the isolated effects of topology gradation, porosity distribution, and pore diameter profiles on the burner performance. In the next and final chapter, smoothly graded porous matrices were introduced and tested using lithography-based ceramic manufacturing, thus demonstrating the potential for tailoring PMBs for enhanced performance. Designed using Triply Periodic Minimal Surfaces, 3D structures with specified axial porosity and pore diameter profiles were translated from computer models into physical samples using Lithography-based ceramic manufacturing. The printed samples were implemented in a PMB and tested over a range of operating conditions to test the feasibility and performance of additive manufactured materials in PMBs. The largest stability regime resulted from a smoothly-graded pore diameter matrix as compared to a conventional “step” PMB. At different operating conditions, the flame dynamically stabilized in the matrix and thus, enables stable operation of a wider range of equivalence ratios. These experiments also demonstrate the sensitivity of the flame to the geometric profile of the porous matrix, confirming that tailored PMBs can be developed to achieve drastically different burner performances.

Beyond serving as a comparison to previous theoretical, computational, and preliminary experimentation, the samples were also tested to characterize the effects of feedstock particle diameter, layer thickness, and printing orientation on the macro-scale thermal and durability properties of 3D printed ceramics. SEM and EDX analysis techniques were employed to test for material degradation and chemical changes, and showed that the samples remain chemically and structurally stable even after 24 hours of flame exposure. XCT imaging was used to test the fidelity of the printing technology in reproducing the input STL geometry and identify potential areas for improving the fabrication methodology.

The contributions summarized above further the fundamental understanding of

PMBs as well as advance the development of this technology for deployment in practical applications. Suggestions for potential next steps in further advancing these objectives are presented in the following section.

## 7.2 Directions for future work

### 7.2.1 Addressing challenges in deploying PMBs to real-world applications

Large-scale implementations of the PMB technology have not yet been achieved, which can be partially attributed to the insufficient durability of current ceramic porous structures, limited knowledge of the pore-scale processes, and the challenge of experimentation at scales and operating conditions of practical relevance. Development and testing of low thermal expansion ceramics can help to alleviate concerns related to durability, which are assumed to be caused by thermal shock. Pore-scale simulations and non-intrusive 3D diagnostics can inform some of the pore-scale physics and guide the development of enhanced closure models (see below for more discussion on closure model development). The work presented in Chapter 4 contributes to alleviating the challenge regarding experimentation at practical conditions. To continue this work, future studies are needed to test PMB performance with real transportation fuels as well as to identify the effects of liquid-fuel evaporation. Additionally, strategies for effective heating of the porous matrix are needed. Currently, the flame is ignited and operated for minutes before the porous matrix sufficiently heats up to facilitate an embedded flame. This delay would be infeasible for aviation applications.

### 7.2.2 Developing improved closure models for combustion in porous media

Although the 1D volume-averaged model (see Chapter 2) in conjunction with empirical model coefficients qualitatively captures trends in flame stability for different porous matrix designs, as presented in Chapter 5, the results do not quantitatively

match those of the corresponding experiment. This motivates further development of volume-averaged models and macro-scale transport properties. Such insight can be gained from pore-resolved simulations, as well as by non-intrusive 3D experimental diagnostics. Additionally, the simplifications and assumptions made in the model formulation regarding surface-catalytic chemistry can be further explored and quantified. For this, Energy Dispersive X-ray Analysis can be applied to study the surface properties and compositions of ceramic materials applied in the combustion zone of PMBs. Furthermore, it is worthwhile exploring the operating conditions under which the laminar flow assumption fails and appropriate turbulence models are need for an accurate description of the combustion process.

### **7.2.3 Applying tailored ceramic structures to applications beyond PMBs**

In Chapter 5 and 6, significant performance improvements for PMBs were demonstrated based on tailoring of the porous matrix. The design and manufacturing of fully tailored ceramic porous structures have potential applications to other energy and thermal management systems that rely on temperature and corrosion resistance while maintaining a low pressure-drop. Due to their advantageous properties, ceramic porous structures are also often utilized in various other fluid flow applications such as filtration, volumetric solar receivers, catalytic converters, heat exchangers and thermal protection materials ([Sommers et al. 2010](#)). In future studies, the framework introduced in this dissertation for designing and fabricating tailored ceramic structures can be applied to optimize these systems.

### **7.2.4 Improving and expanding the ceramic porous structure fabrication methodology**

As illustrated in Chapter 6, recent advances in AM for ceramics begin to enable similar design flexibility as that of plastics and metals. In this work, the LCM method was applied to fabricate tailored ceramic porous structures. By applied light to cure a

photosensitive resin, this method enables higher feature resolution and surface quality as compared to thermal energy-based methods such as selective laser sintering. However, this otherwise advantageous technique can hinder the faithful fabrication of the input geometry in some cases, since thinner features have less absorption and thus become even thinner than what the input STL prescribes. To alleviate this discrepancy, algorithms for modifying the input geometry can be developed to counteract the strut thinning effect in accordance with the energy of the printer used and the composition of the feedstock material.

The study presented in Chapter 3, which found that burners with low thermally conductive materials upstream and high thermally conductive materials downstream result in enhanced flame stability, motivates an extension of the porous matrix tailoring proposed in Chapter 5 and 6. Beyond topology grading, which is presented as a means to modulate the radiative and interphase heat transfer modes, in future work, the thermal properties of the solid matrix itself can be functionalized by a composition or microporosity gradient to enable further customization. This could be achieved by careful engineering of the input resin or by spatially varying the thermal processing of the green part (please refer to Chapter 6 for details).

Lastly, the durability of the printed ceramic structure requires improvement. The porous matrices used presented in Chapter 6 underwent significant cracking and spallation during the combustion experiment. Structural optimization can help inform enhanced designs that reduce thermal stresses and alleviate thermal shock damage.

# Appendix A

## Experimental Data

### A.1 Introduction

The experimental data presented graphically throughout this dissertation are provided here in tables. Each section corresponds to the data associated with a those of a different chapter.

### A.2 Performance study at atmospheric conditions

Data are presented here corresponding to the experimental results of Chapter 3.

#### A.2.1 Stability diagram

Table A.1: Data corresponding to the stable operating conditions presented in Fig. 3.6.

$\phi$	$\dot{m}''$ [kg/(m <sup>2</sup> s)]
<i>Burner 1</i>	
0.49	0.40
0.47	0.13
0.53	0.34
Continued on next page	

Table A.1 – continued from previous page

$\phi$	$\dot{m}''$ [kg/(m <sup>2</sup> s)]
0.59	0.50
0.53	0.47
0.49	0.40
<i>Burner 2</i>	
0.50	0.35
0.51	0.10
0.55	0.09
0.60	0.23
0.65	0.29
0.65	0.74
0.60	0.59
0.50	0.35
<i>Burner 3</i>	
0.50	0.38
0.50	0.11
0.56	0.22
0.60	0.31
0.65	0.38
0.65	0.81
0.60	0.61
0.55	0.50
0.50	0.38
<i>Burner 4</i>	
0.51	0.16
0.50	0.07
0.56	0.23
0.65	0.41
0.56	0.25
Continued on next page	

**Table A.1 – continued from previous page**

$\phi$	$\dot{m}''$ [kg/(m <sup>2</sup> s)]
0.51	0.16
<i>Burner 5</i>	
0.50	0.36
0.50	0.15
0.55	0.16
0.61	0.30
0.66	0.39
0.66	0.85
0.61	0.64
0.55	0.50
0.50	0.36

### A.2.2 Thermocouple measurements

Table A.2: Thermocouple measurements, [K], corresponding to burner 1 and 2, including data from Fig. 3.8. The equivalence ratio,  $\phi$ , and mass flux rate,  $\dot{m}''$ , for each Operating Condition (OC) are described in the table.

X [cm]	OC 1	OC 2	OC 3	OC 4
<i>Burner 1</i>				
	OC 1: $\phi = 0.49$ , $\dot{m}'' = 0.40$ kg/(m <sup>2</sup> s)			
	OC 2: $\phi = 0.47$ , $\dot{m}'' = 0.13$ kg/(m <sup>2</sup> s)			
	OC 3: $\phi = 0.53$ , $\dot{m}'' = 0.34$ kg/(m <sup>2</sup> s)			
	OC 4: $\phi = 0.53$ , $\dot{m}'' = 0.47$ kg/(m <sup>2</sup> s)			
7.663	1.11258E+03	8.44080E+02	1.09234E+03	1.18539E+03
5.498	1.11484E+03	1.00458E+03	1.15439E+03	1.04398E+03
4.942	6.48300E+02	8.19640E+02	7.27750E+02	5.96120E+02
Continued on next page				

Table A.2 – continued from previous page

X [cm]	OC 1	OC 2	OC 3	OC 4
3.593	3.95010E+02	4.75640E+02	3.92560E+02	3.88610E+02
6.530	1.33815E+03	1.06866E+03	1.29508E+03	1.39406E+03
5.577	1.46770E+03	1.24529E+03	1.43149E+03	1.50014E+03
4.387	5.04410E+02	6.89180E+02	6.90190E+02	4.99880E+02
2.958	4.19350E+02	4.54510E+02	4.15010E+02	4.15950E+02
7.980	1.16044E+03	8.89070E+02	1.12121E+03	1.21746E+03
6.450	1.40207E+03	1.17531E+03	1.38025E+03	1.44868E+03
5.260	1.35994E+03	1.17524E+03	1.35253E+03	1.39341E+03
3.593	4.55660E+02	5.03770E+02	4.67330E+02	4.51700E+02
7.403	1.13845E+03	8.92740E+02	1.10915E+03	1.19652E+03
5.657	1.40178E+03	1.18686E+03	1.42279E+03	1.27213E+03
4.307	4.58790E+02	6.35460E+02	4.88310E+02	4.40700E+02
2.879	4.11190E+02	4.53590E+02	4.02200E+02	4.03640E+02
<i>Burner 2</i>				
OC 1: $\phi = 0.50, \dot{m}'' = 0.40 \text{ kg}/(\text{m}^2\text{s})$				
OC 2: $\phi = 0.51, \dot{m}'' = 0.10 \text{ kg}/(\text{m}^2\text{s})$				
OC 3: $\phi = 0.56, \dot{m}'' = 0.48 \text{ kg}/(\text{m}^2\text{s})$				
OC 4: $\phi = 0.55, \dot{m}'' = 0.09 \text{ kg}/(\text{m}^2\text{s})$				
7.663	9.74610E+02	8.23020E+02	1.16163E+03	8.91600E+02
5.498	1.22457E+03	1.10687E+03	1.37724E+03	1.20897E+03
4.942	5.62310E+02	6.68490E+02	6.53720E+02	7.86930E+02
3.593	3.94420E+02	4.81760E+02	4.17140E+02	5.41770E+02
6.530	1.26953E+03	1.05852E+03	1.41124E+03	1.10716E+03
5.577	1.11810E+03	1.16369E+03	1.23510E+03	1.23982E+03
4.387	5.14620E+02	5.86750E+02	5.94390E+02	6.70470E+02
2.958	3.91270E+02	4.64330E+02	4.16610E+02	5.15860E+02
7.980	1.00897E+03	8.32770E+02	1.18993E+03	8.88130E+02
6.450	1.25914E+03	1.07444E+03	1.41469E+03	1.11385E+03
Continued on next page				

Table A.2 – continued from previous page

X [cm]	OC 1	OC 2	OC 3	OC 4
5.260	8.19940E+02	9.11970E+02	8.92340E+02	1.00414E+03
3.593	3.85000E+02	4.73410E+02	4.04900E+02	5.48840E+02
7.403	1.02356E+03	8.79990E+02	1.19600E+03	9.37050E+02
5.657	1.06066E+03	9.81160E+02	1.21018E+03	1.04714E+03
4.307	4.55180E+02	5.71890E+02	5.09000E+02	7.09330E+02
2.879	3.76750E+02	4.52970E+02	3.95310E+02	5.00290E+02
<i>Burner 2</i>				
	OC 1: $\phi = 0.60$ , $\dot{m}'' = 0.59 \text{ kg}/(\text{m}^2\text{s})$			
	OC 2: $\phi = 0.60$ , $\dot{m}'' = 0.23 \text{ kg}/(\text{m}^2\text{s})$			
	OC 3: $\phi = 0.65$ , $\dot{m}'' = 0.74 \text{ kg}/(\text{m}^2\text{s})$			
	OC 4: $\phi = 0.65$ , $\dot{m}'' = 0.29 \text{ kg}/(\text{m}^2\text{s})$			
7.663	1.22724E+03	1.10733E+03	1.32258E+03	1.16825E+03
5.498	1.40968E+03	1.40616E+03	1.51796E+03	1.57791E+03
4.942	6.58140E+02	9.15790E+02	6.97950E+02	8.63040E+02
3.593	4.03080E+02	5.12050E+02	4.00430E+02	4.69640E+02
6.530	1.47459E+03	1.34684E+03	1.57199E+03	1.42665E+03
5.577	1.28156E+03	1.45479E+03	1.64426E+03	1.64426E+03
4.387	5.90470E+02	7.23020E+02	6.00170E+02	6.85450E+02
2.958	4.06490E+02	4.98420E+02	4.07050E+02	4.69070E+02
7.980	1.25591E+03	1.11495E+03	1.34074E+03	1.17344E+03
6.450	1.48456E+03	1.35255E+03	1.58458E+03	1.43591E+03
5.260	8.55390E+02	1.18449E+03	9.72460E+02	1.22505E+03
3.593	3.98560E+02	5.09220E+02	3.99880E+02	4.80490E+02
7.403	1.26019E+03	1.15921E+03	1.35485E+03	1.22736E+03
5.657	1.23696E+03	1.27689E+03	1.34474E+03	1.35821E+03
4.307	5.03820E+02	6.69890E+02	5.03960E+02	6.11540E+02
2.879	3.82870E+02	4.70430E+02	3.80690E+02	4.40840E+02

### A.2.3 Emissions measurements

Table A.3: Emissions measurements, including data corresponding to Fig. 3.10.

$\phi$	$\dot{m}''$ [kg/(m <sup>2</sup> s)]	NO <sub>x</sub> [ppm]	CO [ppm]
<i>Burner 1</i>			
0.50	0.13	3.9	950
0.50	0.34	6.4	12
0.55	0.26	8.6	5
0.56	0.49	9.5	6
<i>Burner 2</i>			
0.50	0.13	4	58
0.50	0.35	5.6	5
0.55	0.15	5.1	15
0.56	0.48	8.8	0
0.60	0.6	11	0
0.60	0.24	8.8	2
0.65	0.74	13.5	0
0.65	0.3	13.3	0
<i>Burner 3</i>			
0.50	0.11	1.7	84
0.50	0.39	4.2	1
0.56	0.49	4.9	0
0.65	0.79	10.8	0
0.65	0.37	8.1	4
<i>Burner 5</i>			
0.50	0.15	2.8	305
0.50	0.34	4	2
0.55	0.16	4.3	23
0.55	0.49	6.4	0
0.60	0.63	7.9	0
Continued on next page			

**Table A.3 – continued from previous page**

$\phi$	$\dot{m}''$ [kg/(m <sup>2</sup> s)]	NO <sub>x</sub> [ppm]	CO [ppm]
0.60	0.30	7.9	0
0.64	0.84	11	0
0.65	0.41	12	0

### A.2.4 Pressure drop measurements

Table A.4: Pressure drop,  $\Delta P$ , measurements, including data corresponding to the cold flow cases of Fig. 3.11. Note that the units in the table are in WC, not pressure drop percentage as in the corresponding figure. B 1–B 5 refer to burners 1–5.

$\dot{m}''$ [kg/(m <sup>2</sup> s)]	B 1	B 2	B 3	B 4	B 5
0.090	0.10	0.05	0.04	0.04	0.02
0.136	0.12	0.10	0.06	0.06	0.04
0.181	0.16	0.15	0.08	0.08	0.06
0.227	0.20	0.18	0.10	0.10	0.08
0.272	0.24	0.23	0.12	0.13	0.10
0.300	0.30	0.30	0.20	0.20	0.12
0.363	0.34	0.34	0.18	0.19	0.15
0.410	0.38	0.41	0.21	0.22	0.18
0.454	0.44	0.47	0.24	0.25	0.21
0.499	0.48	0.55	0.27	0.28	0.24
0.544	0.54	0.64	0.32	0.33	0.28
0.590	0.60	0.74	0.36	0.37	0.32
0.600	0.70	0.80	0.40	0.40	0.36
0.681	0.72	0.93	0.45	0.47	0.41
0.730	0.78	1.04	0.50	0.53	0.45
0.771	0.86	1.14	0.56	0.59	0.51
Continued on next page					

**Table A.4 – continued from previous page**

$\dot{m}''$ [kg/(m <sup>2</sup> s)]	B 1	B 2	B 3	B 4	B 5
0.817	0.92	1.26	0.62	0.64	0.56
0.862	0.98	1.42	0.68	0.71	0.62
0.907	1.04	1.55	0.74	0.77	0.68

Table A.5: Pressure drop,  $\Delta P$ , measurements, including data corresponding to the reacting flow cases of Fig. 3.11. Note that the units in the table are in WC, not pressure drop percentage as in the corresponding figure.

$\phi$	$\Delta P$ [WC]	$\dot{m}''$ [kg/(m <sup>2</sup> s)]
<i>Burner 1</i>		
0.49	0.66	0.40
0.47	0.30	0.13
0.53	0.76	0.46
0.54	0.63	0.34
0.59	1.02	0.61
0.59	0.84	0.49
<i>Burner 2</i>		
0.50	0.46	0.35
0.51	0.16	0.10
0.56	0.79	0.48
0.55	0.18	0.09
0.60	1.06	0.59
0.60	0.40	0.23
0.65	1.59	0.74
0.65	0.51	0.29
<i>Burner 3</i>		
0.50	0.30	0.38
Continued on next page		

**Table A.5 – continued from previous page**

$\phi$	$\Delta P$ [WC]	$\dot{m}''$ [ $\text{kg}/(\text{m}^2\text{s})$ ]
0.50	0.09	0.11
0.56	0.48	0.50
0.55	0.19	0.22
0.60	0.69	0.61
0.60	0.29	0.31
0.65	1.06	0.81
0.65	0.37	0.38
<i>Burner 4</i>		
0.51	0.13	0.16
0.50	0.06	0.07
0.56	0.26	0.25
0.56	0.23	0.23
0.65	0.40	0.41
<i>Burner 5</i>		
0.50	0.21	0.36
0.50	0.08	0.15
0.55	0.40	0.50
0.55	0.10	0.16
0.61	0.61	0.64
0.61	0.24	0.30
0.66	0.94	0.85
0.66	0.34	0.39

### A.3 Performance study at elevated pressures

Data are presented here corresponding to the experimental results of Chapter 4.

### A.3.1 Thermocouple measurements

Table A.6: Thermocouple measurements, [K], including data from Fig. 4.7. The equivalence ratio,  $\phi$ , and mass flux rate,  $\dot{m}''$ , for each Operating Condition (OC) are described in the table. The thermocouples A–D correspond to the locations specified in Fig. 4.4 and Table 4.1.

X [cm]	OC 1	OC 2	OC 3
<b>C<sub>7</sub>H<sub>16</sub>, P = 2 bar</b>			
OC 1: $\phi = 0.48$ , $\dot{m}'' = 0.93 \text{ kg}/(\text{m}^2\text{s})$			
OC 2: $\phi = 0.56$ , $\dot{m}'' = 0.94 \text{ kg}/(\text{m}^2\text{s})$			
OC 3: $\phi = 0.55$ , $\dot{m}'' = 1.25 \text{ kg}/(\text{m}^2\text{s})$			
<i>Thermocouple A</i>			
0.000	7.623253784E+02	1.363262939E+03	1.366096069E+03
-2.540	5.185150757E+02	9.611578369E+02	8.220453491E+02
-3.810	5.202416992E+02	5.879607544E+02	5.567918701E+02
<i>Thermocouple B</i>			
-0.635	1.046046143E+03	1.439506836E+03	1.446230591E+03
-1.905	6.573975830E+02	1.138226685E+03	1.091549194E+03
-3.175	5.345131836E+02	6.799805908E+02	6.232887573E+02
-4.445	5.264062500E+02	5.606742554E+02	5.398196411E+02
<i>Thermocouple C</i>			
0.000	1.071028931E+03	1.338040894E+03	1.303938843E+03
-1.270	1.198503174E+03	1.474011841E+03	1.463832886E+03
-2.540	8.166044312E+02	1.197314087E+03	1.206987915E+03
-3.810	5.408385010E+02	6.203256836E+02	5.825817261E+02
<i>Thermocouple D</i>			
-0.635	9.758443604E+02	1.454181885E+03	1.444311523E+03
-1.905	6.573411255E+02	1.343134033E+03	1.426283813E+03
-3.175	5.239997559E+02	6.672416382E+02	6.637753296E+02
-4.445	4.922854614E+02	5.655061035E+02	5.332313843E+02
Continued on next page			

Table A.6 – continued from previous page

X [cm]	OC 1	OC 2	OC 3
<b>C<sub>7</sub>H<sub>16</sub>, P = 8 bar</b>			
OC 1: $\phi = 0.43, \dot{m}'' = 1.34 \text{ kg}/(\text{m}^2\text{s})$			
OC 2: $\phi = 0.45, \dot{m}'' = 1.37 \text{ kg}/(\text{m}^2\text{s})$			
OC 3: $\phi = 0.47, \dot{m}'' = 1.34 \text{ kg}/(\text{m}^2\text{s})$			
<i>Thermocouple A</i>			
0.000	1.124291138E+03	1.224386719E+03	1.208440063E+03
-2.540	5.673013916E+02	5.899315796E+02	7.016051636E+02
-3.810	5.344287109E+02	5.163800659E+02	5.473346558E+02
<i>Thermocouple B</i>			
-0.635	1.206957764E+03	1.260600342E+03	1.269578735E+03
-1.905	7.477445068E+02	7.353905029E+02	8.979294434E+02
-3.175	5.672174683E+02	5.543125610E+02	5.739199219E+02
-4.445	5.386884766E+02	5.186033936E+02	5.406185303E+02
<i>Thermocouple C</i>			
0.000	1.142541748E+03	1.175655518E+03	1.184848999E+03
-1.270	1.190306641E+03	1.211479004E+03	1.269468994E+03
-2.540	7.902610474E+02	8.737660522E+02	9.311281738E+02
-3.810	5.625871582E+02	5.703827515E+02	5.633975220E+02
<i>Thermocouple D</i>			
-0.635	1.176246216E+03	1.301678589E+03	1.261055176E+03
-1.905	7.992365723E+02	1.120156860E+03	9.906898804E+02
-3.175	5.695621948E+02	6.416304321E+02	5.737596436E+02
-4.445	5.174402466E+02	5.627601929E+02	5.253329468E+02
<b>C<sub>7</sub>H<sub>16</sub>, P = 20 bar</b>			
OC 1: $\phi = 0.42, \dot{m}'' = 2.68 \text{ kg}/(\text{m}^2\text{s})$			
OC 2: $\phi = 0.45, \dot{m}'' = 2.68 \text{ kg}/(\text{m}^2\text{s})$			
OC 3: $\phi = 0.47, \dot{m}'' = 2.68 \text{ kg}/(\text{m}^2\text{s})$			
Continued on next page			

Table A.6 – continued from previous page

X [cm]	OC 1	OC 2	OC 3
<i>Thermocouple A</i>			
0.000	8.817604370E+02	1.095660400E+03	1.128142090E+03
-2.540	5.062882385E+02	1.217053711E+03	1.289847046E+03
-3.810	5.134098511E+02	5.862951660E+02	5.893911743E+02
<i>Thermocouple B</i>			
-0.635	9.251233521E+02	1.178474121E+03	1.213199707E+03
-1.905	5.000321655E+02	7.057630005E+02	7.585959473E+02
-3.175	4.841200562E+02	5.305122070E+02	5.380095825E+02
-4.445	5.194582520E+02	5.354114990E+02	5.372238159E+02
<i>Thermocouple C</i>			
0.000	9.709367065E+02	1.064175659E+03	1.104646606E+03
-1.270	8.374114990E+02	1.151773193E+03	1.183930176E+03
-2.540	5.679837036E+02	1.102768921E+03	1.178371460E+03
-3.810	5.000469360E+02	5.996542358E+02	5.993294067E+02
<i>Thermocouple D</i>			
-0.635	9.411005859E+02	1.147118774E+03	1.186350220E+03
-1.905	5.784133301E+02	1.049581543E+03	1.090358398E+03
-3.175	4.749279480E+02	9.471055298E+02	9.258198853E+02
-4.445	4.609077148E+02	5.645560303E+02	5.632178955E+02
<b>CH<sub>4</sub>, P = 8 bar</b>			
OC 1: $\phi = 0.47$ , $\dot{m}'' = 1.55 \text{ kg}/(\text{m}^2\text{s})$			
OC 2: $\phi = 0.51$ , $\dot{m}'' = 1.41 \text{ kg}/(\text{m}^2\text{s})$			
OC 3: $\phi = 0.55$ , $\dot{m}'' = 1.56 \text{ kg}/(\text{m}^2\text{s})$			
<i>Thermocouple A</i>			
0.000	5.238940430E+02	1.334230103E+03	1.417808838E+03
-2.540	5.962717896E+02	9.361379395E+02	1.320207397E+03
-3.810	5.173845825E+02	5.324657593E+02	5.537218628E+02
Continued on next page			

**Table A.6 – continued from previous page**

X [cm]	OC 1	OC 2	OC 3
<i>Thermocouple B</i>			
-0.635	1.351470947E+03	1.364047241E+03	1.506046265E+03
-1.905	8.140333252E+02	1.070389160E+03	1.236580200E+03
-3.175	6.112147217E+02	6.288558960E+02	6.845559082E+02
-4.445	5.293483276E+02	5.337797852E+02	5.381506348E+02
<i>Thermocouple C</i>			
0.000	1.232952881E+03	1.262563232E+03	1.388148193E+03
-1.270	1.280846802E+03	1.334791870E+03	1.485341431E+03
-2.540	8.925872803E+02	1.067294189E+03	1.315293091E+03
-3.810	5.637731934E+02	5.658208008E+02	5.841667480E+02
<i>Thermocouple D</i>			
-0.635	1.379195557E+03	1.416020630E+03	1.521233276E+03
-1.905	1.224544067E+03	1.329981201E+03	1.463799683E+03
-3.175	6.226228027E+02	6.258140259E+02	6.503134155E+02
-4.445	5.635533447E+02	5.648952026E+02	5.564841919E+02

### A.3.2 Stability diagram, emissions, and pressure drop

Table A.7: Data corresponding to the stability regime and CO emissions presented in Fig. 4.5, NO<sub>x</sub> emissions of the stable operating conditions as presented in Fig. 4.10, and pressure drop measurements corresponding to Fig. 4.9a.

$\dot{m}''$ [kg/(m <sup>2</sup> s)]	$\phi$	NO <sub>x</sub> [ppm]	CO [ppm]	$\Delta P$ [Pa]
$C_7H_{16}$ , P = 2 bar				
1.519	0.5503	22.93	0.00	340.91
1.378	0.5526	21.15	0.00	286.166
1.250	0.5542	20.37	0.00	236.398
Continued on next page				

Table A.7 – continued from previous page

$\dot{m}''$ [kg/(m <sup>2</sup> s)]	$\phi$	NO <sub>x</sub> [ppm]	CO [ppm]	$\Delta P$ [Pa]
1.136	0.5549	19.82	0.00	194.095
1.037	0.5522	27.24	0.00	164.234
0.937	0.5559	18.70	0.00	146.816
0.852	0.5561	19.27	0.00	126.908
0.781	0.5490	19.77	0.00	107.001
0.775	0.4420	15.49	0.00	114.466
$C_7H_{16}$ , P = 8 bar				
3.258	0.5107	21.11	6.33	330.957
2.961	0.5107	18.40	11.35	258.794
2.744	0.4888	14.63	0.00	171.700
2.692	0.5110	18.65	8.98	206.537
2.451	0.5106	18.37	13.78	136.862
2.490	0.4898	12.73	0.00	169.211
2.263	0.4898	13.18	0.00	116.955
2.051	0.4915	13.76	0.00	102.024
1.837	0.4739	17.21	17.21	74.652
1.624	0.4608	10.14	0.00	52.256
1.511	0.4671	08.83	0.00	64.698
1.511	0.4671	11.00	0.00	57.233
1.368	0.4452	9.81	0.00	42.303
1.342	0.4688	8.48	0.00	49.768
1.341	0.4609	9.67	0.00	44.791
1.241	0.4461	9.32	3.22	37.326
1.144	0.4660	7.79	0.00	37.326
1.141	0.4269	5.73	0.00	34.838
$C_7H_{16}$ , P = 20 bar				
3.243	0.4366	5.78	6.43	64.698
2.958	0.4935	-	-	57.233
Continued on next page				

Table A.7 – continued from previous page

$\dot{m}''$ [kg/(m <sup>2</sup> s)]	$\phi$	NO <sub>x</sub> [ppm]	CO [ppm]	$\Delta P$ [Pa]
2.954	0.4703	-	-	57.233
2.949	0.4479	-	-	54.745
2.947	0.4371	5.39	0.00	52.256
2.684	0.4673	6.55	0.00	49.768
2.680	0.4451	5.55	0.00	47.280
2.679	0.4371	5.22	0.00	42.303
2.672	0.396	-	-	37.326
2.440	0.4443	5.39	0.00	42.303
2.440	0.4364	-	-	39.814
2.436	0.4155	-	-	32.349
2.432	0.3867	-	-	32.349
2.218	0.4674	6.96	0.00	27.372
2.215	0.4453	5.31	0.00	27.372
2.213	0.4280	-	-	29.861
2.212	0.4241	4.40	14.66	27.372
2.211	0.4155	-	-	27.372
2.209	0.4039	-	-	19.907
2.016	0.4361	-	-	27.372
2.014	0.4150	-	-	27.372
2.011	0.3949	-	-	22.396
1.833	0.4356	-	-	22.396
$\text{CH}_4$ , P = 8 bar				
3.378	0.539	0.00	16.07	343.399
3.346	0.522	-	-	-
3.035	0.519	-	-	-
2.755	0.533	6.20	18.62	223.956
2.501	0.534	-	-	179.165
2.275	0.534	-	-	139.350
Continued on next page				

Table A.7 – continued from previous page

$\dot{m}''$ [kg/(m <sup>2</sup> s)]	$\phi$	NO <sub>x</sub> [ppm]	CO [ppm]	$\Delta P$ [Pa]
2.114	0.487	-	-	-
2.065	0.552	-	-	111.978
1.916	0.488	-	-	-
1.881	0.550	-	-	94.559
1.801	0.464	5.64	8.47	82.117
1.761	0.488	2.67	14.73	72.164
1.747	0.486	-	-	69.675
1.703	0.471	-	-	-
1.697	0.554	-	-	77.140
1.650	0.508	8.03	9.64	74.652
1.646	0.463	2.90	8.12	69.675
1.592	0.485	-	-	54.745
1.555	0.547	-	-	64.698
1.548	0.472	-	-	54.745
1.492	0.465	2.94	8.83	59.722
1.492	0.465	8.14	9.5	57.233
1.414	0.550	-	-	57.233
1.411	0.509	0	14.55	49.768
1.409	0.486	-	-	49.768
1.408	0.473	0	13.74	47.280
1.351	0.467	2.90	6.38	49.768
1.283	0.504	0	14.65	42.303
1.281	0.472	0	13.75	42.303
1.228	0.516	2.67	8.57	47.280
1.224	0.468	2.90	6.09	42.303
1.223	0.446	3.11	7.79	44.791
1.197	0.485	-	-	32.349
1.115	0.516	2.71	8.68	39.814
Continued on next page				

**Table A.7 – continued from previous page**

$\dot{m}''$ [kg/(m <sup>2</sup> s)]	$\phi$	NO <sub>x</sub> [ppm]	CO [ppm]	$\Delta P$ [Pa]
1.112	0.470	2.98	6.27	37.326
1.112	0.476	2.71	8.68	39.814
1.014	0.475	2.94	7.65	32.349
1.013	0.468	9.08	5.14	32.349
1.012	0.446	13.70	4.45	32.349
1.011	0.425	6.74	5.39	32.349
0.986	0.491	-	-	44.791
0.915	0.478	0.00	6.96	29.861
0.914	0.450	17.41	5.57	29.861
0.831	0.481	0.00	6.66	27.372
0.830	0.457	0.00	6.66	24.884
0.829	0.434	0.00	7.51	24.884
0.828	0.413	0.00	5.82	24.884
0.828	0.413	3.48	5.57	24.884
0.817	0.489	-	-	27.372
0.675	0.466	-	-	22.396

## A.4 Modulation of heat transfer

Data are presented here corresponding to the experimental results of Chapter 5.

### A.4.1 Stability diagram and pressure drop

Table A.8: Data corresponding to the stable operating conditions presented in Fig. 5.7 and pressure drop,  $\Delta P$ , measurements, including data corresponding to Fig. 5.9.

$\phi$	$\dot{m}''$ [kg/(m <sup>2</sup> s)]	$\Delta P$ [Pa]
<i>Step burner</i>		
0.77	0.696	493.2136
0.75	1.494	1691.3676
0.75	1.345	1459.1003
0.75	1.245	1288.9452
0.75	1.395	1540.8999
0.75	1.295	1379.7020
0.70	0.796	393.1967
0.70	1.046	952.1399
0.70	0.896	480.8104
0.70	0.647	570.6614
0.70	0.996	892.3531
0.70	0.697	615.3761
0.70	0.896	838.0003
0.65	0.596	226.5941
0.65	0.646	253.8830
0.65	0.746	333.4971
0.65	0.547	197.6324
0.65	0.696	291.9568
0.63	0.397	109.6134
0.63	0.297	50.6319
0.63	0.547	393.9942
0.63	0.248	29.1515
0.63	0.347	82.2651
0.63	0.197	13.5421
0.60	0.547	189.2295
Continued on next page		

Table A.8 – continued from previous page

$\phi$	$\dot{m}''$ [kg/(m <sup>2</sup> s)]	$\Delta P$ [Pa]
0.60	0.497	161.6610
0.60	0.397	113.5134
0.60	0.447	137.3167
0.60	0.347	89.0744
0.55	0.397	133.9729
0.55	0.347	91.6047
0.55	0.297	69.7681
0.55	0.347	81.6545
0.55	0.247	45.0045
0.55	0.297	63.1530
0.55	0.198	17.7485
<i>Graded burner</i>		
0.77	0.777	1334.0146
0.77	2.063	4678.4691
0.77	1.674	3252.6440
0.77	1.563	2901.4920
0.77	2.342	5519.8820
0.77	1.340	2400.9060
0.77	1.675	3394.7219
0.77	1.899	4048.9977
0.77	2.120	4667.7894
0.77	1.952	4336.5377
0.77	2.288	5329.5126
0.77	2.234	5141.0684
0.77	2.067	4525.4278
0.77	2.066	4505.6694
0.77	1.843	3793.2128
0.77	2.122	4835.0973
Continued on next page		

**Table A.8 – continued from previous page**

$\phi$	$\dot{m}''$ [kg/(m <sup>2</sup> s)]	$\Delta P$ [Pa]
0.77	2.007	4486.7014
0.77	1.898	4168.9462
0.77	2.178	4897.3818
0.77	2.123	4719.3639
0.77	1.956	4203.0117
0.77	1.955	4223.7428
0.77	1.730	3393.5262
0.77	1.898	4088.8083
0.77	1.507	2760.2450
0.77	1.787	3636.5340
0.77	1.395	2481.2770
0.77	2.012	4379.4995
0.77	1.619	3045.7890
0.77	2.012	4377.8074
0.77	1.057	1626.4081
0.77	1.451	2632.0891
0.77	1.731	3457.0165
0.77	1.675	3317.5528
0.76	1.004	1524.1104
0.76	1.113	1727.3785
0.76	0.550	669.4674
0.76	0.164	143.5248
0.76	0.136	115.0191
0.76	0.117	97.0086
0.70	1.393	2617.2349
0.70	1.338	2471.1344
0.70	1.226	2146.3371
0.70	0.891	1044.1845
Continued on next page		

**Table A.8 – continued from previous page**

$\phi$	$\dot{m}''$ [kg/(m <sup>2</sup> s)]	$\Delta P$ [Pa]
0.70	1.280	2301.2833
0.70	1.114	1883.5406
0.70	1.058	1376.2468
0.70	1.339	2439.1461
0.70	1.282	2325.8444
0.70	1.001	1611.0878
0.70	0.947	1482.4962
0.70	1.171	2009.9030
0.70	1.002	1261.0910
0.70	0.892	1355.3435
0.70	0.946	1151.7309
0.70	1.114	1485.5157
0.69	0.163	124.1728
0.69	0.117	89.7016
0.69	0.136	106.7884
0.69	0.098	70.0711
0.69	0.108	77.8334
0.63	0.722	806.5997
0.63	0.666	639.3972
0.63	0.555	490.1344
0.63	0.499	417.2178
0.63	0.779	893.6602
0.63	0.611	565.7340
0.63	0.723	721.2415
0.62	0.163	107.8311
0.62	0.117	68.5113
0.62	0.135	83.0192
0.62	0.108	58.9783
Continued on next page		

**Table A.8 – continued from previous page**

$\phi$	$\dot{m}''$ [kg/(m <sup>2</sup> s)]	$\Delta P$ [Pa]
0.56	0.331	257.6229
0.55	0.220	156.6677
0.55	0.163	83.3193
0.55	0.135	63.2806
0.55	0.107	46.8075
0.55	0.117	52.9388
0.55	0.089	38.1288
0.55	0.080	31.1988

### A.4.2 Thermocouple measurements

Table A.9: Thermocouple measurements, [K], corresponding to the step and graded burners from Fig. 5.8. The equivalence ratio,  $\phi = 0.75$ , for all cases and mass flux rate,  $\dot{m}''$ , for each Operating Condition (OC) are described in the table.

X [cm]	OC 1	OC 2	OC 3
<i>Step burner</i>			
OC 1: $\dot{m}'' = 0.69$ kg/(m <sup>2</sup> s)			
OC 2: $\dot{m}'' = 1.25$ kg/(m <sup>2</sup> s)			
-1.1	303.53	302.58	-
0.6	305.15	303.02	-
1.8	348.44	321.84	-
2.9	1006.8	555.26	-
3.5	1309.8	842.95	-
4.5	1485.0	1473.8	-
6.4	1286.6	1336.2	-
<i>Graded burner</i>			
Continued on next page			

**Table A.9 – continued from previous page**

X [cm]	OC 1	OC 2	OC 3
OC 1: $\dot{m}'' = 0.55 \text{ kg}/(\text{m}^2\text{s})$			
OC 2: $\dot{m}'' = 1.06 \text{ kg}/(\text{m}^2\text{s})$			
OC 3: $\dot{m}'' = 2.29 \text{ kg}/(\text{m}^2\text{s})$			
-1.2	359.36	302.0	306.05
0.7	1049.4	515.87	302.42
1.9	1232.0	980.88	410.04
3.2	1189.3	1253.5	601.55
4.5	1183.6	1471.60	1275.5
5.8	1080.3	1204.2	1235.6
7.0	965.82	1138.6	1218.0

## A.5 Tailoring porous media burners

Data are presented here corresponding to the experimental results of Chapter 6.

### A.5.1 Thermal conductivity of additive manufactured alumina

Table A.10: Thermal conductivity data, [W/mK], as a function of temperature, corresponding to Fig. 6.6. Materials are described in Section 6.5. The relative standard deviation of each measurement is shown in parenthesis.

Material	298 K	373 K	473 K
A, 25 $\mu\text{m}$	3.7 (0.6%)	3.2 (0.7%)	1.9 (1.0%)
A, 50 $\mu\text{m}$	25.0 (2.0%)	18.7 (4.0%)	13.3 (1.0%)
B, 25 $\mu\text{m}$	28.2 (1.1%)	22.2 (1.3%)	16.5 (1.4%)
B, 50 $\mu\text{m}$	28.6 (1.6%)	12.7 (0.8%)	8.5 (1.1%)
Continued on next page			

**Table A.10 – continued from previous page**

Material	298 K	373 K	473 K
B, 50 $\mu\text{m}$ , Matrix	5.2 (0.9%)	2.9 (0.7%)	2.2 (0.8%)
Conventional ( <a href="#">Auerkari 1996</a> )	37	30	23

### A.5.2 Stability diagram

Table A.11: Data corresponding to the stable operating conditions presented in Fig. [6.11](#).

$\phi$	$\dot{m}'' [\text{kg}/(\text{m}^2\text{s})]$
<i>Burner 1</i>	
0.60	0.40
0.60	0.45
0.60	0.50
0.60	0.55
<i>Burner 2</i>	
0.55	0.15
0.55	0.20
0.55	0.25
0.60	0.15
0.60	0.20
0.60	0.25
0.60	0.30
0.65	0.15
0.65	0.20
0.65	0.25
0.65	0.30
0.65	0.35
Continued on next page	

**Table A.11 – continued from previous page**

$\phi$	$\dot{m}'' \text{ [kg/(m}^2\text{s)]}$
0.65	0.40
0.70	0.10
0.70	0.15
0.70	0.20
0.70	0.25
0.70	0.30
0.70	0.35
0.70	0.40
0.70	0.45
0.75	0.10
0.75	0.15
0.75	0.20
0.75	0.25
0.75	0.30
0.75	0.30
0.75	0.40
0.75	0.50
0.75	0.55
0.75	0.60
0.75	0.65
0.75	0.70
0.75	0.75
0.75	0.80
0.80	0.80
0.80	0.85
0.80	0.90
0.80	0.95
0.80	1.00
Continued on next page	

**Table A.11 – continued from previous page**

$\phi$	$\dot{m}'' \text{ [kg/(m}^2\text{s)]}$
0.80	1.05
0.85	0.15
0.85	0.20
0.85	0.25
0.85	0.30
0.85	0.40
0.85	0.50
0.85	0.60
0.85	1.05
0.85	1.10
0.85	1.15
0.85	1.20
0.85	1.25
0.95	0.05
0.95	0.10
0.95	0.15
0.95	0.20
0.95	0.25
0.95	0.30
1.05	0.15
1.10	0.30
1.15	0.15
1.15	0.70
1.15	0.75
1.15	0.80
1.15	0.85
1.15	0.90
1.15	0.95
Continued on next page	

**Table A.11 – continued from previous page**

$\phi$	$\dot{m}'' \text{ [kg/(m}^2\text{s)]}$
1.15	1.00
1.15	1.05
1.15	1.10
1.15	1.15
1.15	1.20
<i>Burner 3</i>	
0.54	0.20
0.55	0.16
0.55	0.20
0.60	0.15
0.60	0.20
0.60	0.25
0.60	0.30
0.65	0.15
0.65	0.20
0.65	0.25
0.65	0.30
0.65	0.35
0.65	0.40
0.70	0.35
0.70	0.40
0.70	0.45
0.70	0.50

# Bibliography

- M. Aronovici, G. Bianchi, L. Ferrari, M. Barbato, S. Gianella, and A. Ortona. Heat and mass transfer in ceramic lattices during high-temperature oxidation. *Journal of the American Ceramic Society*, 98(8):2625–2633, 2015.
- P. Auerkari. *Mechanical and physical properties of engineering alumina ceramics*. Technical Research Centre of Finland Espoo, 1996.
- V. S. Babkin, A. A. Korzhavin, and V. A. Bunev. Propagation of premixed gaseous explosion flames in porous media. *Combustion and Flame*, 87:182–190, 1991.
- A. Bakry, A. Al-Salaymeh, A. H. Al-Muhtaseb, A. Abu-Jrai, and D. Trimis. Adiabatic premixed combustion in a gaseous fuel porous inert media under high pressure and temperature: Novel flame stabilization technique. *Fuel*, 90(2):647–658, 2011.
- A. J. Barra and J. L. Ellzey. Heat recirculation and heat transfer in porous burners. *Combustion and Flame*, 137(1-2):230–241, 2004.
- A. J. Barra, G. Diepvans, J. L. Ellzey, and M. R. Henneke. Numerical study of the effects of material properties on flame stabilization in a porous burner. *Combustion and Flame*, 134(4):369–379, 2003.
- C. Bedoya, I. Dinkov, P. Habisreuther, N. Zarzalis, H. Bockhorn, and P. Parthasarathy. Experimental study, 1D volume-averaged calculations and 3D direct pore level simulations of the flame stabilization in porous inert media at elevated pressure. *Combustion and Flame*, 162(10):3740–3754, 2015.
- J. Binner. *Ceramics Foams*, chapter 2.1, pages 31–56. John Wiley & Sons, Ltd, 2006.

- J. Buckmaster and T. Takeno. Blow-off and flashback of an excess enthalpy flame. *Combustion Science and Technology*, 25(3-4):153–158, 1981.
- C. T. Bowman, R. K. Hanson, D. F. Davidson, W. C. Gardiner, Jr., V. Lissianski, G. P. Smith, D. M. Golden, M. Frenklach, and M. Goldenberg. GRI-Mech 2.11, 1995. available from <http://www.me.berkeley.edu/gri-mech/>.
- S. R. Choi and N. P. Bansal. Alumina-reinforced zirconia composites. In *Handbook of Ceramic Composites*, pages 437–457. Springer, 2005.
- K. V. Dobrego, S. A. Zhdanok, and A. I. Zaruba. Experimental and analytical investigation of the gas filtration combustion inclination instability. *International Journal of Heat and Mass Transfer*, 44(11):2127–2136, 2001.
- N. Dukhan and P. Patel. Equivalent particle diameter and length scale for pressure drop in porous metals. *Experimental Thermal and Fluid Science*, 32(5):1059–1067, 2008.
- J. Dunnmon, S. Sobhani, M. Wu, R. Fahrig, and M. Ihme. An investigation of internal flame structure in porous media combustion via x-ray computed tomography. *Proceedings of the Combustion Institute*, 36:4399–4408, 2016.
- M. K. El-Hossaini, M. Maerefat, and K. Mazaheri. Numerical investigation on the effects of pressure drop on thermal behavior of porous burners. *Journal of Heat Transfer*, 130(3):032601, 2008.
- J. L. Ellzey, E. L. Belmont, and C. H. Smith. Heat recirculating reactors: Fundamental research and applications. *Progress in Energy and Combustion Science*, 72: 32–58, 2019.
- S. Ergun and A. A. Orning. Fluid flow through randomly packed columns and fluidized beds. *Industrial & Engineering Chemistry*, 41(6):1179–1184, 1949.
- J. C. Ferguson, F. Panerai, A. Borner, and N. N. Mansour. Puma: the porous microstructure analysis software. *SoftwareX*, 7:81–87, 2018.

- X. Fu, R. Viskanta, and J. P. Gore. Measurement and correlation of volumetric heat transfer coefficients of cellular ceramics. *Experimental Thermal and Fluid Science*, 17(4):285–293, 1998.
- R. Gabbielli, I. Turner, and C. R. Bowen. Development of modelling methods for materials to be used as bone substitutes. In *Key Engineering Materials*, volume 361, pages 903–906. Trans Tech Publ, 2008.
- S. Gianella, D. Gaia, and A. Ortona. High temperature applications of Si-SiC cellular ceramics. *Advanced Engineering Materials*, 14(12):1074–1081, 2012.
- D. G. Goodwin. CANtera: An open-source, object-oriented software suite for combustion, 1998.
- D. R. Hardesty and F. J. Weinberg. Burners producing large excess enthalpies. *Combustion Science and Technology*, 8(5-6):201–214, 1973.
- J. Howell, M. Menguc, and R. Siegel. *Thermal Radiation Heat Transfer, 5th Edition*. Taylor & Francis, 2010.
- J. R. Howell, M. J. Hall, and J. L. Ellzey. Combustion of hydrocarbon fuels within porous inert media. *Progress in Energy and Combustion Science*, 22(2):121–145, 1996.
- P.-F. Hsu and J. R. Howell. Measurements of thermal conductivity and optical properties of porous partially stabilized zirconia. *Experimental Heat Transfer*, 5(4):293–313, 1992.
- P.-F. Hsu, W. D. Evans, and J. R. Howell. Experimental and numerical study of premixed combustion within nonhomogeneous porous ceramics. *Combustion Science and Technology*, 90(1-4):149–172, 1993.
- B. Hussey, R. Hussey, J. Wilson, and J. Wilson. *Advanced Technical Ceramics Directory and Databook*. Springer US, 1998.

- M. D. Innocentini, V. R. Salvini, A. Macedo, and V. C. Pandolfelli. Prediction of ceramic foams permeability using ergun's equation. *Materials Research*, 2(4):283–289, 1999.
- N. S. Jacobson. Corrosion of silicon-based ceramics in combustion environments. *Journal of the American Ceramic Society*, 76(1):3–28, 1993.
- S. Jugjai, N. Wongpanit, T. Laoketkan, and S. Nokkaew. The combustion of liquid fuels using a porous medium. *Experimental Thermal and Fluid Science*, 26(1):15–23, 2002.
- M. Kaplan and M. J. Hall. The combustion of liquid fuels within a porous media radiant burner. *Experimental Thermal and Fluid Science*, 11(1):13–20, 1995.
- M. Kaviany. *Principles of heat transfer in porous media*. Springer Science & Business Media, 1991.
- A. Kazakov and M. Frenklach. DRM19, 1994. available from <http://www.me.berkeley.edu/drm/>.
- J. J. Kojima and D. G. Fischer. Multiscalar analyses of high-pressure swirl-stabilized combustion via single-shot dual-SBG Raman spectroscopy. *Combustion Science and Technology*, 185(12):1735–1761, 2013.
- J. J. Kojima, D. G. Fischer, and J.-Y. Chen. Code-validation scalar measurements in high-pressure hydrogen-added methane combustion. *Journal of Propulsion and Power*, pages 285–304, 2016.
- Y. Kotani and T. Takeno. An experimental study on stability and combustion characteristics of an excess enthalpy flame. *Proceedings of the Combustion Institute*, 19(1):1503–1509, 1982.
- D. Legland, I. Arganda-Carreras, and P. Andrey. MorphoLibJ: integrated library and plugins for mathematical morphology with ImageJ. *Bioinformatics*, 32(22):3532–3534, 2016.

- T. Lu, C. K. Law, C. S. Yoo, and J. H. Chen. Dynamic stiffness removal for direct numerical simulations. *Combustion and Flame*, 156(8):1542–1551, 2009.
- J. F. Lynch. Engineering property data on selected ceramics. volume ii. carbides. Technical report, Metals and Ceramics Information Center, Battelle Columbus Laboratories, Columbus, OH, 1979.
- E. Maire, P. Colombo, J. Adrien, L. Babout, and L. Biassetto. Characterization of the morphology of cellular ceramics by 3D image processing of X-ray tomography. *J Eur. Ceram. Soc.*, 27(4):1973–1981, 2007.
- I. Malico and J. F. Pereira. Numerical study on the influence of radiative properties in porous media combustion. *Journal of Heat Transfer*, 123(5):951–957, 03 2001.
- T. L. Marbach and A. K. Agrawal. Experimental study of surface and interior combustion using composite porous inert media. In *ASME Turbo Expo 2003*, pages 549–556. American Society of Mechanical Engineers, 2003.
- I. Maskery, L. Sturm, A. O. Aremu, A. Panesar, C. B. Williams, C. J. Tuck, R. D. Wildman, I. A. Ashcroft, and R. J. M. Hague. Insights into the mechanical properties of several triply periodic minimal surface lattice structures made by polymer additive manufacturing. *Polymer*, 152:62–71, 2018.
- F. P. Melchels, K. Bertoldi, R. Gabbrielli, A. H. Velders, J. Feijen, and D. W. Grijpma. Mathematically defined tissue engineering scaffold architectures prepared by stereolithography. *Biomaterials*, 31(27):6909–6916, 2010.
- J. A. Miller and C. T. Bowman. Mechanism and modeling of nitrogen chemistry in combustion. *Progress in Energy and Combustion Science*, 15(4):287–338, 1989.
- S. S. Minaev, S. I. Potytnyakov, and V. S. Babkin. Combustion wave instability in the filtration combustion of gases. *Combustion, Explosion and Shock Waves*, 30(3):306–310, 1994.
- G. Mitteramskogler, R. Gmeiner, R. Felzmann, S. Gruber, C. Hofstetter, J. Stampfl, J. Ebert, W. Wachter, and J. Laubersheimer. Light curing strategies for

- lithography-based additive manufacturing of customized ceramics. *Additive Manufacturing*, 1-4:110 – 118, 2014.
- D. Mohaddes, M. Ihme, and C. T. Chang. Superadiabatic matrix-stabilized combustion for gas turbine engine performance improvement. *Energy*, 2019.
- M. A. Mujeebu, M. Z. Abdullah, M. A. Bakar, A. Mohamad, R. Muhad, and M. Abdullah. Combustion in porous media and its applications—a comprehensive survey. *J. Environ. Manage.*, 90(8):2287–2312, 2009.
- M. A. Mujeebu, M. Z. Abdullah, A. A. Mohamad, and M. Z. A. Bakar. Trends in modeling of porous media combustion. *Progress in Energy and Combustion Science*, 36(6):627–650, 2010.
- S. Mullens, J. Luyten, and J. Zeschky. *Characterization of Structure and Morphology, in: Cellular Ceramics*, pages 225–266. Wiley-VCH Verlag GmbH & Co. KGaA, 2006.
- E. Noordally, J. M. Przybylski, and J. J. Witton. Porous media combustors for clean gas turbine engines. Technical report, Bedford: Cranfield University, 2004.
- V. M. Patel and P. Talukdar. Evaluation of radiative properties of a representative foam structure using blocked-off region approach integrated with finite volume method. *Int. J. Therm. Sci.*, 108(Supplement C):89 – 99, 2016.
- A. P. Philipse and H. L. Schram. Non-Darcian airflow through ceramic foams. *Journal of the American Ceramic Society*, 74(4):728–732, 4 1991.
- S. Rajagopalan and R. A. Robb. Schwarz meets schwann: Design and fabrication of biomorphic and durataxic tissue engineering scaffolds. *Medical Image Analysis*, 10 (5):693–712, 2006.
- A. Ruys. Processing, structure, and properties of alumina ceramics. In A. Ruys, editor, *Alumina Ceramics*, pages 71 – 121. Woodhead Publishing, 2019.
- A. H. Schoen. Infinite periodic minimal surfaces without self-intersections. 1970.

- H. A. Schwarz. *Gesammelte mathematische Abhandlungen*, volume 1. Springer, 1890.
- M. Schwentenwein and J. Homa. Additive manufacturing of dense alumina ceramics. *International Journal of Applied Ceramic Technology*, 12(1):1–7, 2015.
- J. C. Slattery. Flow of viscoelastic fluids through porous media. *AICHE Journal*, 13(6):1066–1071, 1967.
- S. Sobhani, B. Haley, D. Bartz, J. Dunnmon, J. Sullivan, and M. Ihme. Investigation of lean combustion stability, pressure drop, and material durability in porous media burners. In *ASME Turbo Expo 2017: Turbomachinery Technical Conference and Exposition*, pages V05CT17A001–V05CT17A001. American Society of Mechanical Engineers, 2017.
- S. Sobhani, J. Legg, D. F. Bartz, J. Kojima, C. T. Chang, J. D. Sullivan, J. P. Moder, and M. Ihme. Experimental investigation of lean premixed pre-vaporized liquid-fuel combustion in porous media burners at elevated pressures up to 20 bar. *Under Review*, 2019a.
- S. Sobhani, D. Mohaddes, E. Boigne, P. Muhunthan, and M. Ihme. Modulation of heat transfer for extended flame stabilization in porous media burners via topology gradation. *Proceedings of the Combustion Institute*, 37(4):5697–5704, 2019b.
- S. Sobhani, P. Muhunthan, D. Mohaddes, E. Boigne, Z. Cheng, and M. Ihme. Enabling tailored porous media burners via additive manufacturing. *Proceedings of the 11th U.S. National Combustion Meeting*, 2019c.
- A. Sommers, Q. Wang, X. Han, C. T. Joen, Y. Park, and A. Jacobi. Ceramics and ceramic matrix composites for heat exchangers in advanced thermal systems—A review. *Applied Thermal Engineering*, 30(11-12):1277–1291, 2010.
- A. R. Studart, U. T. Gonzenbach, E. Tervoort, and L. J. Gauckler. Processing routes to macroporous ceramics: A review. *Journal of the American Ceramic Society*, 89(6):1771–1789, 2006.

- H. Takami, T. Suzuki, Y. Itaya, and M. Hasatani. Performance of flammability of kerosene and NO<sub>x</sub> emission in the porous burner. *Fuel*, 77(3):165–171, 1998.
- D. Trimis and F. Durst. Combustion in a porous medium—advances and applications. *Combustion Science and Technology*, 121(1-6):153–168, 1996.
- C.-J. Tseng and J. R. Howell. Combustion of liquid fuels in a porous radiant burner. *Combustion Science and Technology*, 112(1):141–161, 1996.
- S. Vijayaventaraman, L. Zhang, S. Zhang, J. Y. Hsi Fuh, and W. F. Lu. Triply periodic minimal surfaces sheet scaffolds for tissue engineering applications: An optimization approach toward biomimetic scaffold design. *ACS Applied Bio Materials*, 1(2):259–269, 2018.
- S. Vijaykant and A. K. Agrawal. Liquid fuel combustion within silicon-carbide coated carbon foam. *Experimental Thermal and Fluid Science*, 32(1):117–125, 2007.
- S. Voss, M. Mendes, J. Pereira, S. Ray, J. Pereira, and D. Trimis. Investigation on the thermal flame thickness for lean premixed combustion of low calorific H<sub>2</sub>/CO mixtures within porous inert media. *Proceedings of the Combustion Institute*, 34(2):3335 – 3342, 2013.
- K. Wawrzinek and D. Trimis. Flame stabilization of highly diffusive gas mixtures in porous inert media. In J. Vad, T. Lajos, and R. Schilling, editors, *Modelling Fluid Flow: The State of the Art*, pages 107–121. Springer, 2004.
- S. Whitaker. Diffusion and dispersion in porous media. *AICHE Journal*, 13(3):420–427, 1967.
- L. Williams and A. K. Agrawal. Acoustic effects of porous inert media on lean premixed combustion at elevated pressures. *AIAA Paper AIAA 2012-0207*, 2012.
- S. Wood and A. T. Harris. Porous burners for lean–burn applications. *Progress in Energy and Combustion Science*, 34(5):667–684, 2008.

- M. G. Zabetakis, S. Lambiris, and G. S. Scott. Flame temperatures of limit mixtures. *Proceedings of the Combustion Institute*, 7(1):484–487, 1958.
- J. Zhang, L. Cheng, C. Zheng, Z. Luo, and M. Ni. Numerical studies on the inclined flame front break of filtration combustion in porous media. *Energy and Fuels*, 27(8):4969–4976, 2013.
- C. Zheng, L. Cheng, A. Saveliev, Z. Luo, and K. Cen. Gas and solid phase temperature measurements of porous media combustion. *Proceedings of the Combustion Institute*, 33(2):3301–3308, 2011.